Experimental and Computational Study of Structure and Dynamics of Bulk Conjugated Polymer Systems

Kiran H. Kanekal

A thesis

Submitted in partial fulfillment of the

requirements for the degree of

Master of Science in Chemical Engineering

University of Washington

2016

Committee:

Lilo D. Pozzo

Jim Pfaendtner

Program Authorized to Offer Degree:

Department of Chemical Engineering

University of Washington

Abstract

Experimental and Computational Characterization of Bulk Conjugated Polymer Systems

Kiran H. Kanekal

Chair of the Supervisory Committee:
Associate Professor Lilo D. Pozzo
Department of Chemical Engineering

Conjugated polymers are a highly relevant class of materials due to their low processing cost and applicability in flexible electronic devices. A significant challenge in the field remains to relate the chemical structure of these materials with their morphology and dynamics, which in turn affect their charge transport characteristics. There are several experimental and computational methods that are commonly used when characterizing conjugated polymers. In this work, we attempt to synergistically apply these techniques so as to obtain a clear understanding of the properties that affect the structure and dynamics of conjugated polymers. A large experimental data set is used to validate molecular dynamics (MD) simulations of poly(3-hexylthiophene), a model conjugated polymer system. A sensitivity analysis of system and simulation parameters is performed, and the key factors affecting the conjugated polymer dynamics and configuration are found to be molecular weight, crystallinity, equilibration method, and force field parameters. Specifically, the atomistic partial charges are found to have the greatest influence on both properties. The identification of these key parameters will inform further studies of more complex conjugated polymer systems, elucidating the relationship between conjugated polymer chemistry and performance.

Table of Contents

List of Figures

Figure

Acknowledgements

I would like to thank my advisor, Professor Lilo Pozzo for being an inspirational mentor and believing in me even when I could not believe in myself. I am incredibly fortunate to have had someone with such incredible poise and confidence as a guide, and I will carry her example with me throughout the rest of my professional career. I would like to thank Professor Jim Pfaendtner for his staunch support, wonderful insights, and illuminating conversations (both scientific and personal) over the past three years. I would also like to thank my lab mates for all their help as fellow scientists, coworkers, and friends: Dr. Yeneneh Yimer for tirelessly working alongside me on this project while discussing the latest basketball scores, Dr. Jeffrey Richards for excellent science-related conversations and for introducing me to equally excellent restaurants in Seattle, Dr. Gregory Newbloom for finding even my lamest jokes to be hilarious (or at least faking it well enough to fool me), Dr. David Li for updating me on the latest click-bait articles and quizzes, Dr. Pablo de la Iglesia for providing an endless supply of corgi pictures, Michael Lombardo for showing me new ways to exercise my sarcasm, Yuyin Xi for TA-ing with me and teaching me Chinese tongue twisters, Yi-Ting Lee for always having tasty snacks on hand, Ryan Kastilani for constantly reminding me what good etiquette in the workplace meant, and Caitlyn Wolf for saving our team during trivia nights.

Dedication

To my friends and family

Chapter 1: The Importance of Conjugated Polymers

Conjugated polymers are polymers with monomer units that are conjugated (i.e. they will have a hybridized orbital structure similar to that of benzene, usually represented with alternating single and double bonds) such that the linking of these units into a polymer chain allows for charge delocalization across multiple monomer units.[1] This delocalization allows charge to travel along a single chain or for charges to hop between chains when sufficient overlap of the pi-orbitals between monomer units of different chains is achieved.[1] This phenomenon is commonly known as pi-stacking. The monomer units typically consist of a conjugated moiety and a non-conjugated moiety, usually an alkyl chain, which increases the configurational entropy and thus the solubility of the polymer.[1] The polymers can then be thought of as comb-like polymers, consisting of a conjugated rigid backbone from which side-chains extend. Conjugated polymers are a unique, highly relevant class of materials due to their applications in flexible and economical organic photovoltaics[2], transistors[3], and thermoelectric devices[4].

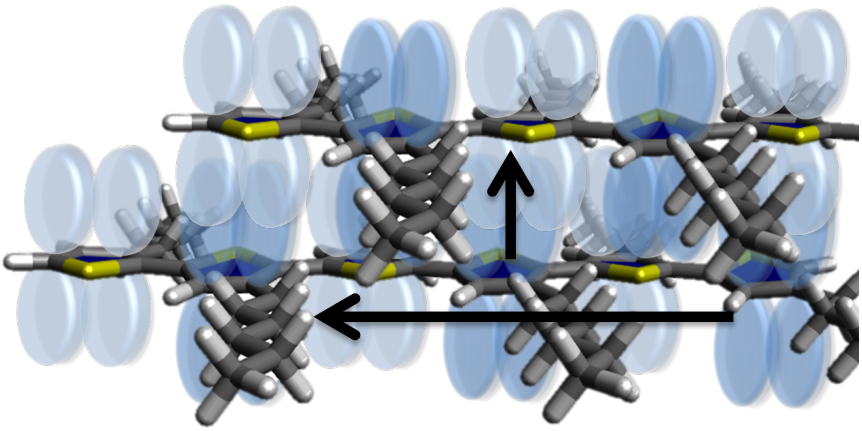

Figure 1.1 Schematic showing pi-orbital overlap in P3HT-RRe. The arrows denote the ability for charge to travel along a single chain or hop from chain to chain via pi-stacking.

1.1 A Brief History of the Development of Conjugated Polymers

The earliest synthesized conjugated polymers were polyacetylene, polyaniline, and polypyrrole[1]. While it was possible to achieve charge mobilities of up to 0.1 $cm^2\ V^{-1}\ s^{-1}$, it was notoriously difficult to process these materials using traditional methods (i.e. through melt processing or through a solvent dispersion method) and ensure homogeneity in the charge transport of devices made with these polymers[1]. The difficulty arose from the fact that the pi-orbital interactions between chains were very strong and it was far more energetically favorable for the chains to pi-stack with each other rather than disperse in an organic solvent. This changed around the mid 1980s, when synthetic chemists were able to add substitution moieties to the conjugated polymers that increased their configurational entropy, which lowered the change in solvation free energy for these materials to the point where certain organic solvents could disperse the polymers[1]. For example, Elsenbaumer et al. modified polythiophene with alkyl side-chains to make regiorandom poly(3-alkylthiophene)s (P3ATs), which were soluble in chloroform and other organic solvents, while unsubstituted polythiophenes were insoluble in the same solvents[5]. Regiorandom poly(3-hexylthiophene) (P3HT-RRa) could be solvent cast into thin films with field effect transistor (FET) mobilities of $10^{-5}\ cm^2\ V^{-1}\ s^{-1}$, although higher mobilities were possible by doping the system[5]. In 1992, McCullough and Lowe synthesized regioregular poly(3-hexylthiophene) (P3HT-RRe) and found that the FET mobility for this material increased to $10^{-2}\ cm^2\ V^{-1}\ s^{-1}$.[6] Regioregularity refers to the degree of ordering of the monomer units in a polymer chain such that each monomer has the same head-to-tail orientation. For example, in P3HT, the head group is the thiophene ring, while the tail is the alkyl side-chain. They noted that the regioregular polymer had a

morphology consisting of crystalline domains that were surrounded by amorphous polymer, and hypothesized that the increase in mobility was due to the presence of the crystalline domains, which facilitated greater inter-chain charge transport. This led to the synthesis of more conjugated polymers with chemistries that favored the formation of crystalline domains. In the early 2000s, polyquaterthiophene[7] (PQT) and poly[2,5-bis(3-thiophen-2-yl)thieno[3,2-*b*]thiophene][8] (PBTTT) were synthesized, which showed higher FET mobilities of 0.14 $cm^2 V^{-1} s^{-1}$ and 0.4 $cm^2 V^{-1} s^{-1}$, respectively, with correspondingly higher crystallinity. However, from the latest generation of organic electronic materials, conjugated polymers have been synthesized which appear to have an amorphous morphology when characterized using X-ray scattering techniques, yet these materials have FET mobilities higher than those of PQT and PBTTT[9]. This suggests that the paradigm of equating higher crystallinity to higher charge mobility is not enough to describe the relationship between morphology and charge transport. Furthermore, the role that conjugated polymer dynamics play in describing charge transport for these materials is unclear.

1.2 Applications for Conjugated Polymers

There are three major classes of devices for which conjugated polymers are used today: organic photovoltaic devices[2] (OPVs), organic field-effect transistors[3] (OFETs), and organic thermoelectric devices[4] (OTEs). Each of these devices consists of a conducting or semiconducting organic material (e.g. a conjugated polymer, although organic small molecules are also commonly used) and a set of electrodes. However, both the functions and the design parameters for each of these devices vary greatly.

OPVs, which are used to convert light energy from the sun into electricity, consist of a p-type and n-type material sandwiched between two electrodes, usually as a bulk heterojunction type cell[3]. Common bulk heterojunction solar cells are made up of three layers: a clear top electrode layer, which allows sunlight to pass through it, a bottom electrode layer, and the layer in between the electrodes, known as the active layer. This layer consists of an electron donating p-type material, usually a conjugated polymer such as P3HT-RRe, and an electron accepting n-type material, usually a fullerene derivative[3]. An OPV bulk heterojunction solar cell operates in the following manner. Photons are absorbed into the active layer of the device where they become excitons (electrostatically bound electron and hole pairs). These excitons migrate to the interface between the p and n-type materials, where they split into electrons and holes. The electrons travel to the cathode via the n-type material while the holes travel to the anode via the p-type material, causing current to be generated[2]. One of the main challenges in the OPV field is designing p-type and n-type materials that can be dispersed in order to achieve the proper interfacial area between the two materials while the pathways to their respective electrodes are maintained. The efficiency of these devices also decreases over time due to phase separation between the polymer and fullerene materials, which causes a decrease in the interfacial area between the p and n-type domains[2]. Understanding the nature of the "slow" dynamic motions facilitating this separation can allow for new materials to be developed that ensure they are kinetically trapped in a favorable morphology.

Unlike OPVs, which require both p and n type materials, an OFET only requires one type of organic semiconductor[3]. OFETs have structures similar to bottom-gate thin-film transistors, with the source and drain electrodes sandwiched between an organic

semiconducting channel material and an insulator[3]. The substrate supporting the device is commonly chosen so as to also act as the gate material. The quality of an OFET is described using two parameters: the charge carrier mobility and the current on/off ratio[3]. The charge carrier mobility describes the speed with which a charge carrier (i.e. electron or hole) travels within a material to which an electric field has been applied. The current on/off ratio is the ratio between the current with the maximum applied gate bias and the current without any gate bias applied (measured at the drain electrode). Both the on/off ratio and the carrier mobility must be maximized in order to create optimal OFETs, and continuing advances in molecular design and synthesis of conjugated polymers have led to dramatic increases in OFET performance[3]. While general guidelines for the design of conjugated polymers with high mobilities have been established, it is exceedingly difficult to predict the electronic performance of an OFET from the atomic structure of a monomer.

Thermoelectric devices generate current when subjected to a temperature gradient[4]. The metric of interest when characterizing a thermoelectric device is the dimensionless number ZT, which relates the thermal conductivity, electric conductivity, and the Seebeck coefficient (also known as the thermopower). The Seebeck coefficient is the ratio of the voltage created to the temperature gradient used to create that voltage. A high performance thermoelectric device will have a high electrical conductivity, a low thermal conductivity, and a high Seebeck coefficient[4]. However, many of these parameters have complex interdependencies, making design of high performing thermoelectric materials extremely challenging. Conjugated polymers are uniquely suited for use in thermoelectric devices because electron-phonon coupling effects are more prevalent in conjugated

polymers when compared to traditional inorganic materials such as Bismuth Telluride[4]. The semicrystalline nature of conjugated polymers results in materials with high electrical conductivity, due to the presence of crystalline domains, and low thermal conductivity resulting from the amorphous polymer regions. Furthermore, because conjugated polymers are easier to process in a variety of ways at relatively lower costs compared to inorganic materials, the feasibility of producing novel geometries for thermoelectric devices has also increased[4]. Still, engineering the conjugated polymer chains to adopt specific configurations relative to the thermal gradient is of utmost importance given the highly anisotropic nature of charge transport in these materials.

1.3 Objective

A commonality between all of the devices mentioned above is that processing methods used for fabrication also play a significant role in their performance. Different methods (i.e. solution-processing, vacuum-depositing) will affect the degree of charge percolation in conjugated polymers. This further complicates the problem of knowing how to predict conjugated polymer performance from monomer chemistry because processing effects must also be accurately predicted and mitigated for different chemistries. Computational methods, like molecular dynamics (MD) simulations, can provide the means to circumvent this issue. Recent increases in computational power and efficiency have made high throughput simulations of polymers in a multitude of environments possible. However, these methods can be of questionable accuracy and require experimental validation. The objective of this work is to establish the foundation of a framework designed to bridge the gap between the chemical composition of a conjugated polymer and its electronic characteristics. This is achieved by characterizing a

set of poly (3-alkylthiophene)s via a series of experimental and computational characterization techniques (with special emphasis on regio-random P3HT).

Chapter 2: Experimental Techniques for Characterization of Conjugated Polymers

A great number of experimental techniques have been used for the characterization of conjugated polymer systems. Here, we describe a small subset of these techniques. Wide-angle X-ray scattering (WAXS) is used to characterize the crystal structure and degree of crystallization of these materials. Quasi-elastic neutron scattering (QENS) techniques provide information about the dynamic motions of the polymer chains. Nuclear Magnetic Resonance (NMR) spectroscopy allows the regioregularity of the samples to be quantified. Gel permeation chromatography (GPC) is used to obtain the molecular weight distribution of a conjugated polymer sample. Differential scanning calorimetry (DSC) is used to determine the glass transition and melting temperatures of the polymers. Neutral buoyancy methods are used to determine the density of the polymers in the solid state.

2.1 Wide-Angle X-Ray Scattering

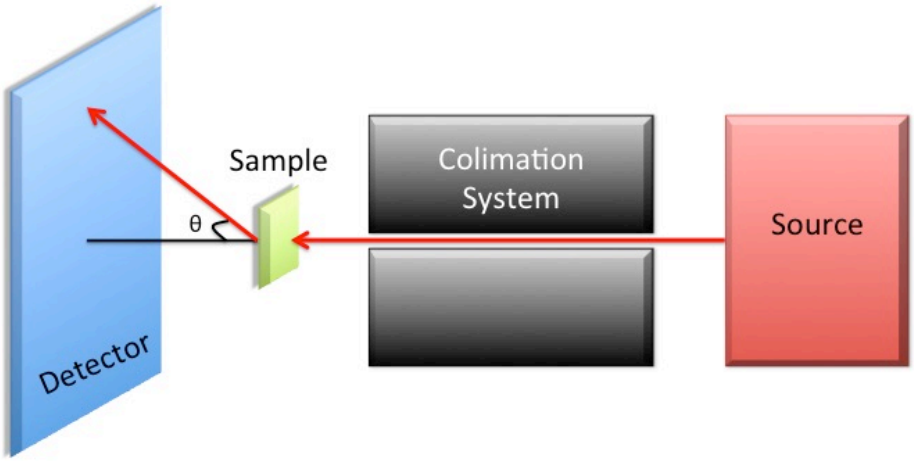

Figure 2.1.1 Diagram showing the WAXS instrument setup.

Wide-angle X-ray scattering (WAXS) is a powerful technique for probing the crystallinity of conjugated polymers. Both the crystal structure and the crystalline fraction of the polymer can be obtained from WAXS measurements[10]. Figure 2.1.1 shows the

basic setup of a WAXS instrument. The source refers to the X-Ray source, which was a Copper K-α source for the measurements conducted in this work. Synchrotron sources, which provide a much higher flux of X-rays, are also frequently used. The X-ray photons that interact with the sample are first collimated so as to have minimal divergence, a controlled illumination size and the same wavelength. The sample consists of a melt-processed conjugated polymer thick-film (~0.1 mm) sandwiched between two pieces of Kapton or Mylar tape. Metal spacers are used to keep the polymer and Kapton/Mylar in place. Furthermore, a small space is kept free for the insertion of a thermocouple that makes direct contact with the sample. The interactions of the X-rays with the sample are assumed to be elastic, meaning that there is no energy transfer between the X-rays and the sample. X-rays are either transmitted through the sample or scatter at an angle θ onto a detector that measures the intensity as a function of angle. The collected scattering pattern is 2-D, but it is reduced to a 1-D profile by integrating the intensity over the length of the detector[10]. The relationship between the scattering angle, θ, and the length scales of the molecular features which cause scattering is given by Bragg's Law[10]:

$$2d\sin\left(\frac{\theta}{2}\right) = n\lambda \qquad (2.1.1)$$

Here, the distance, *d*, corresponds to the length scale of the molecular features that cause scattering, and λ is the wavelength of the X-rays (1.54 Å for a Cu-Kα source).[10] The data is represented as a function of the scattering vector, *q*, which is related to *d* via the following formula:

$$d = \frac{2\pi}{q} \qquad (2.1.2)$$

Note that the incident X-rays interact with the electron clouds in the sample, meaning that the contributions to scattering will mainly come from electron-rich regions in the sample[10]. For conjugated polymers, this corresponds to the conjugated backbone.

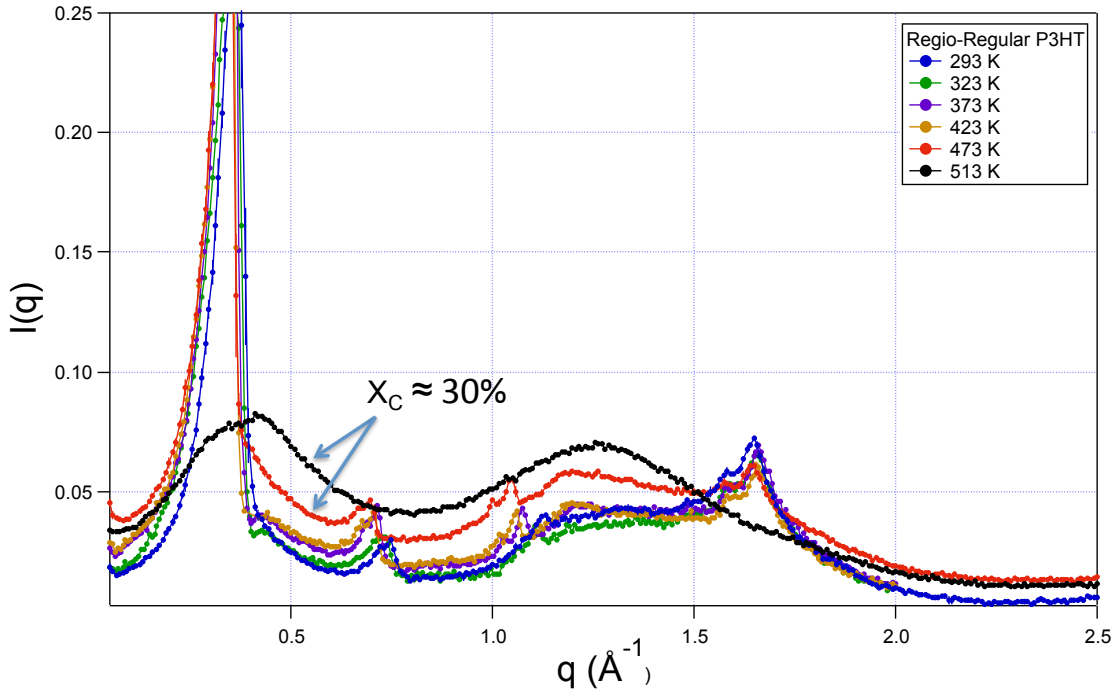

Figure 2.1.2 WAXS profiles of Regio-regular P3HT at different temperatures. X_C refers to the crystalline fraction of the material, calculated by taking the ratio of the scattering intensities at q = 0.55 Å^{-1}.

Regio-regular P3HT in the solid state is a semicrystalline material, meaning it consists of polymer chains arranged to form lamellar crystallites with regions of amorphous polymer surrounding these crystallites[11]. Figure 2.1.2 shows WAXS data collected from samples of regio-regular P3HT at various temperatures. At 293 K, several Bragg peaks are visible, corresponding to the lattice parameters of a P3HT crystalline unit cell[12]. The first peak at q = 0.3 Å^{-1} is the first order 'lamellar' peak (i.e. 100), which corresponds roughly to the distance separating P3HT chains along the side-chain axis. The peaks at 0.6 Å^{-1} and 1.2 Å^{-1} are higher order peaks (i.e. 200, 300) also due to the lamellar structure. The peak at

1.7 Å^{-1} is known as the 'pi-stacking' peak, which corresponds to the distance (3.81 Å) separating the thiophene ring units with overlapping pi orbitals[12]. As the temperature increases, the polymer transitions from semicrystalline to amorphous melt phases, which is reflected in the broadening of the Bragg peaks. For semi-crystalline samples, it is possible to get a rough estimate of the fraction of the material that is in crystalline domains by calculating ratios of the intensities between semi-crystalline and fully amorphous profiles for values of q where the signal is ideally flat and unaffected by the main diffraction peaks. The following formula is used[13]:

$$\frac{I_{scr}(q_0)}{I_{molten}(q_0)} \approx X_{am} = 1 - X_c \qquad (2.1.2)$$

Here, I_{scr} and I_{molten} refer to the intensity of the sample in the semicrystalline state and the molten state, respectively at the same q value (q_0). X_{am} is the fraction of the sample that is amorphous and X_C is the fraction that is crystalline[13]. Thus, WAXS provides a powerful means for determining the degree of crystallinity in a conjugated polymer sample.

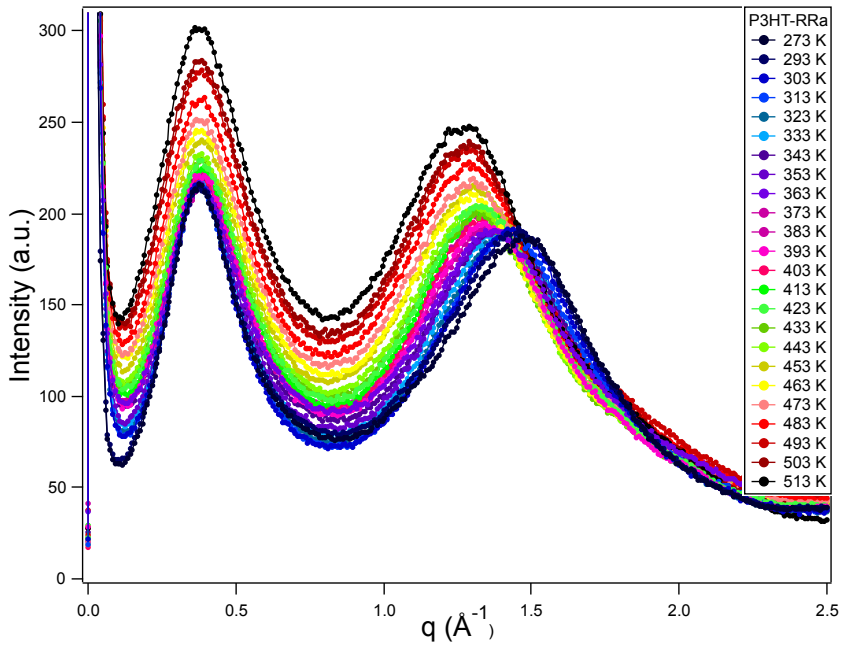

Figure 2.1.3 WAXS profiles of Regio-random P3HT at different temperatures.

Figure 2.1.3 shows WAXS data collected from regio-random P3HT over a large temperature range. The first broad peak corresponds to inter-chain separation distances, and the broadness of the peak highlights the large distribution of chain-chain separation distances that are expected for an amorphous polymer. The second broad peak corresponds to thiophene ring separation distances. Both intra and inter-chain ring-ring separation distances are included in this peak. Interestingly, as temperature increases, the second peak shifts to lower q, indicating increased ring-ring distances at higher temperatures.

2.2 Quasi-Elastic Neutron Scattering

The work presented in this section has since been published in Chapter 5 of "Semiconducting Polymers: Controlled Synthesis and Microstructure" edited by Professor Christine Luscombe.

While elastic scattering provides a method of discerning the structural properties of polymers, quasi-elastic neutron scattering (QENS) allows their dynamics on the molecular scale to be probed. This is because the energy range of neutrons used in this technique is similar to the activation energies of polymers (meV).[10,14–16] The dynamic disorder of polymer semiconductors is much higher than that of traditional semiconducting materials.[17,18] Molecular fluctuations also affect the degree to which π-orbital overlap is achieved, affecting both intra-chain and inter-chain charge transport.[19] In this section, the theory and techniques for QENS are briefly discussed before describing how QENS is being used to study polymer semiconductors.

2.2.1 Theory

$$\frac{\partial^2\sigma}{\partial\hbar\omega\partial\Omega} = \frac{1}{4\pi\hbar}\frac{K_f}{K_i}\left(\sigma_{inc}S_{inc}(Q,\omega)+\sigma_{coh}S_{coh}(Q,\omega)\right) \qquad (2.2.1)$$

In QENS experiments, the quantity measured is the double differential scattering cross-section, which describes the probability of neutrons being scattered into a solid angle $\partial\Omega$ with a change in energy $\partial\hbar\omega$ (Equation 2.2.1).[10] If there is no change in energy, the scattering is elastic, but if there is an energy transfer, the scattering is inelastic. When the energy transfers are close to zero, the scattering is said to be quasi-elastic. K_f and K_i correspond to the scattering vectors of the scattered and incident neutrons, whose ratio approaches 1 for QENS. $S_{inc}(Q,\omega)$ and $S_{coh}(Q,\omega)$ are the incoherent and coherent dynamic scattering functions that link microscopic molecular motions to the observed scattering. $S_{inc}(Q,\omega)$ is related by double Fourier transform to the self-correlation function $G_{self}(R,t)$, which is the probability density of finding an atom at distance R away from itself after an elapsed time t. $S_{coh}(Q,\omega)$ is similarly related to $G_{self}(R,t)$, which is the probability density of finding an atom R away from another atom at an elapsed time t. Thus, $S_{inc}(Q,\omega)$ describes the individual motion of atoms, while $S_{coh}(Q,\omega)$ describes the collective motion of atoms. QENS data is commonly represented using these scattering functions or their Fourier transforms in the time domain, known as the intermediate scattering functions $I_{inc}(Q,t)$ and $I_{coh}(Q,t)$. σ_{inc} and σ_{coh} are scattering cross-sections that are dependent on the scattering lengths characteristic to the nuclei of each atom. The incoherent scattering cross-section of hydrogen is almost two orders of magnitude higher than any of the cross-sections of other atoms that are found in polymers.[10] This means that the incoherent contribution to the double differential scattering cross-section will dominate for hydrogenated polymers, and the data will largely probe the self-motions of hydrogen. For example, QENS measurements of fully hydrogenated P3HT highlight the molecular motions of the hexyl side chains, as they contain the majority of hydrogen

atoms in each monomer. Deuterium, on the other hand, has a significantly lower σ_{inc}, almost equal to that of carbon. By substituting specific hydrogen atoms in a polymer with deuterium, the molecular motions of different parts of a polymer are 'highlighted'. With QENS, the Q dependence of the observed dynamics can also be investigated. This makes it possible to ascertain the type of dynamic motion based on the value of Q (i.e. length scale) where it is observed.

2.2.2 Instrumentation and Methods for Analysis

QENS experiments are usually conducted using three types of instruments: time-of-flight (TOF) spectrometers, backscattering spectrometers, and neutron spin echo (NSE) spectrometers. TOF and backscattering spectrometers detect the changes in energy and momentum of scattered neutrons by measuring the neutron velocity, which is related to energy.[10] However, each instrument has a different method for measuring changes in energy, which results in different energy resolutions and time scales that can be probed.

Data from these instruments is measured as a function of energy transfer ($\hbar\omega$), where broadening of the elastic peak occurs due to molecular dynamics. QENS data in the energy domain can be fit to linear combinations of Lorentzian functions, with the full width at half maximum of the Lorentzian peaks corresponding to the time scale of the observed relaxation.[10,16] For polymer systems, TOF spectrometers are sensitive to fast motions (e.g. methyl rotations), whereas backscattering spectrometers are sensitive to slower segmental motions (e.g. segmental vibration). QENS experiments are usually slow (6-8 hr is typical) but scans of the intensity of the elastic peak as a function of temperature are fast and can be used to identify the activation temperatures for different motions.[16] The intensity of the elastic peak decreases when molecular motions emerge

because more intensity is scattered inelastically. This can be modelled by the Debye-Waller equation to obtain an estimate of the temperature-dependent mean square displacement $\langle r^2 \rangle(T)$.

$$S(Q,T,\omega \approx 0) = \exp\left(-\frac{1}{3}\left\langle r^2 \right\rangle (T)Q^2 \right) \qquad (2.2.2)$$

Unlike backscattering and TOF spectrometers, NSE spectrometers are sensitive to energy transfers in the neV range, corresponding to time scales that can approach 1,000 ns. Additionally, the data is recorded directly in the time domain (i.e. intermediate scattering function) and it is not convoluted by instrument resolution. This technique is mainly used to monitor segmental and chain dynamics of polymers over longer times (i.e. Rouse dynamics and reptation for polymers with very low friction coefficients). In the time domain, information is often extracted from QENS data by fitting to a Kolrausch-William-Watts stretched exponential function.[15,16,20]

$$I(Q,t) = \exp\left[-\left(\frac{t}{\tau} \right)^{\beta} \right] \qquad (2.2.3)$$

Here, τ is the characteristic relaxation time of the dynamic process, and β is a "stretching" parameter ($0 < \beta < 1$). While τ varies greatly with both temperature and Q, a single β value is optimized for all Q (in many cases β is also fixed for multiple temperatures as well).[20] β values have been recorded within the range of 0.2 to 0.8, with polymers usually having a β value of ~0.5. Fourier transforms are often used to convert data from TOF and backscattering spectrometers into the time domain in order to combine with NSE and to extract characteristic relaxation times using KWW fits. The dynamic range of a single instrument is usually insufficient to completely capture all relevant dynamics. A list of QENS spectrometers around the world has been compiled by Colmenero and Arbe.[21] To

date, only TOF and backscattering spectrometers have been used to characterize the dynamics of polymer semiconductors.[22–27]

2.2.3 QENS of Polymer Semiconductors

QENS studies conducted on polymer semiconductors have largely focused on P3HT and polyaniline (PANI). Obrzut et al. measured the elastic intensity of P3HT as a function of temperature and compared these results with dielectric spectroscopy data.[22] They observed that the motions of the side chains are "liberated" at ~ 175 K, and there is also a corresponding decrease in the conductivity of bulk P3HT at this temperature. Using a modified version of equation (2.2), they also calculated the activation energy for the side-chain motions to be ~ 9 kJ/mol. They concluded that local relaxations of the alkyl side chains contributed to increased disorder of the polymer structure, causing an increase in the energy barriers to charge transport. Paterno et al. characterized the dynamics of P3HT-PCBM blends cast from three different solvents (chloroform, chlorobenzene, and ortho-dichlorobenzene).[23] Interestingly, the choice of solvent used had a negligible effect on the observed dynamics. They also noted that addition of PCBM caused a decrease in the quasi-elastic broadening observed at temperatures above 285 K. They hypothesized that this was due to an increase in domains that were not "dynamically active", causing greater confinement of the P3HT side-chains.

Most recently, Etampawala et al. also investigated the dynamics of P3HT/PCBM blends.[24] They assigned a fast relaxation process to P3HT and a slower process to PCBM, and fitted their data as a sum of two KWW functions corresponding to each relaxation. They confirmed that PCBM loading causes a frustration of P3HT side chain dynamics, and attributed this to steric hindrance caused by PCBM on the P3HT side-chains in the

amorphous phase. The Q dependence of the P3HT side-chain dynamics was also examined. For $Q < 0.9$ Å^{-1}, a near linear relationship between the characteristic relaxation time and Q^2 was observed, indicating simple diffusion dominated the observed dynamics at these length scales. For $Q > 1.1$ Å^{-1}, the relationship between the characteristic relaxation time was highly nonlinear with respect to Q. These relaxation times were attributed to local motions within a side-chain, such as methyl rotations and crankshaft motions.

Over the last decade, molecular dynamics (MD) simulations have also proved to be a highly useful complimentary method for analysing QENS data.[15,21] This is because the coherent and incoherent intermediate scattering functions can be directly calculated with Equation 2.4 (with $i = j$ for incoherent scattering).[21]

$$I(Q,t) = \frac{1}{N}\sum_{i,j=1}^{N}\left\langle \exp\left(-iQ\boldsymbol{r}_{ij}(t)\right)\right\rangle \qquad (2.2.4)$$

QENS data has been used to validate MD simulations by calculating intermediate scattering functions and comparing these to experimental *I(Q,t)*. The length scales and time scales accessible with MD simulations are the same as those accessible by QENS experiments. Validated MD simulations provide access to more detailed information than what can be obtained from analytical models like the KWW. For example, QENS can be used to validate force fields used in MD simulations. X-ray and neutron diffraction data can also be compared to MD simulations and used as further validation. Sniechowski et al. has used this approach to study the dynamics of polyaniline (PANI) doped with the plasticizing dopant di-(2-butoxyethoxyethyl) ester of 4-sulfophthalic acid (DB3EPSA).[25-27] The protons in the aliphatic tails of the dopant were the primary contributors to the observed scattering. Sniechowski et al. modelled the experimental data by assuming the

space explored by the aliphatic tail as a limited sphere in which protons could diffuse. They also performed MD simulations of PANI-DB3EPSA and validated their simulations with QENS. The simulations confirmed the analytical model that they proposed, but also revealed a dynamic heterogeneity between the counter-ions that was outside the scope of the model. Specifically, they observed a dramatic difference in the time evolution of the mean square displacement of protons in the dopant, which confirmed the relative immobility of the conjugated polymer compared to the dopant.

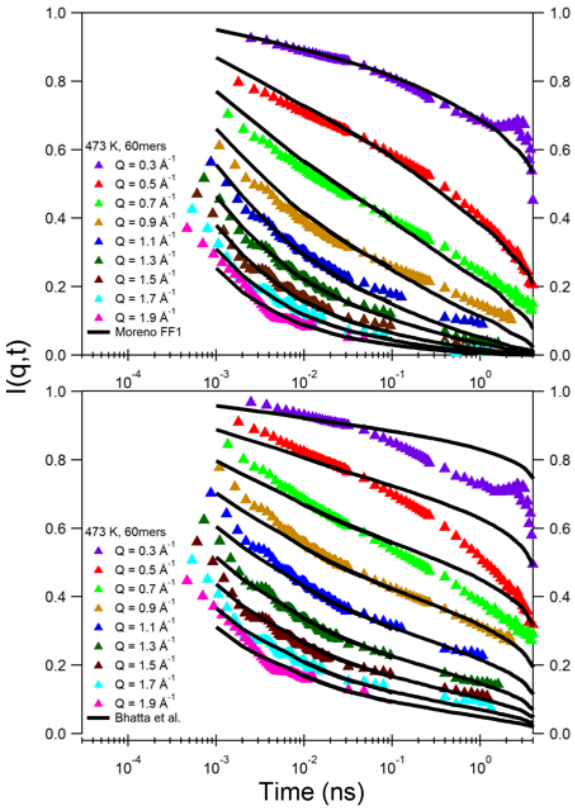

Figure 2.2.1: Comparison of MD simulations of melt phase regio-random P3HT with data obtained from DCS and HFBS at NIST as well as BASIS at ORNL. The upper plot shows a comparison with the OPLS-AA force field modified with a backbone torsion potential developed by Moreno et al.[28] The lower plot shows a comparison with the force field developed by Bhatta et al.[29]

New efforts in our group are focused on using this approach to refine MD force fields used to model the dynamics of poly(3-alkylthiophene)s (P3AT)s. Figure 2.2.1

shows that two published torsion potentials for P3HT, both derived from *ab-initio* DFT calculations, result in large discrepancies between simulations and experimental QENS data. The two torsion potentials overestimate or underestimate the time scales of the decay. This demonstrates that QENS of P3HT is very sensitive to torsional motions of both backbone and side-chains. These parameters are also linked to π-orbital overlap and inter-chain charge transport. QENS coupled with MD simulations will likely continue to provide insight to design superior polymer semiconductors.

2.2.4 QENS Analysis of Regio-Regular P3ATs

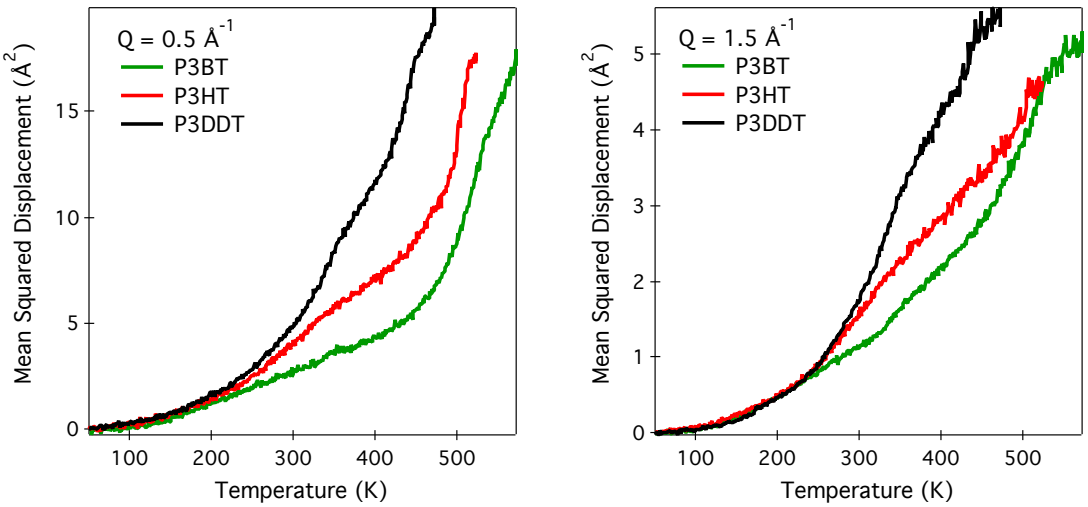

Figure 2.2.2: Mean square displacements calculated from fixed window scans of P3BT, P3HT, and P3DDT thick films at Q = 0.5 Å^{-1} (left) and Q = 1.5 Å^{-1} (right).

Fixed window scans were conducted on thick films of regio-regular P3HT (M_w = 39 kDa, PDI = 2.3), poly(3-butylthiophene) (P3BT) (M_w = 41 kDa, PDI = 2.3), and poly(3-dodecylthiophene) (P3DDT) (M_w = 57 kDa, PDI = 2.1). Equation 2.2.2 was used to calculate the mean squared displacement (MSD) for each sample at Q = 0.5 Å^{-1} and 1.5 Å^{-1}, corresponding to length scales above and below the crossover length scales specified by Etampawala and coworkers[24]. The resulting MSDs are shown in Figure 2.2.2. Note

that these MSDs correspond to the fluctuations of Hydrogen atoms in the samples, and the temperature ranges from 50 K to a temperature past the isotropic melting temperature as measured by DSC for each sample. A change in the slope of the MSD as a function is observed for all samples and Q values at ~175 K, confirming that the activation of the side-chains noted by Obrzut and coworkers[22] occurs regardless of side-chain length. As the temperature increases, the P3DDT sample shows the greatest increase in MSD compared to the other two samples. The curves exhibit another change in slope at ~350 K, which may correspond to the twist glass transition noted by Yazawa and coworkers[37], who reported this transition for P3BT at ~340 K. This transition refers to twisting motions of the thiophene rings in the crystalline phase. This transition is most visible for the P3BT sample because P3BT has a much higher crystalline fraction compared to P3HT and P3DDT, due to the smaller side-chain length that allows for increased packing. At higher temperatures—423 K, 473 K, and 500 K for P3BT, P3HT, and P3DDT respectively—we see the slope increase dramatically as these temperatures coincide with the start of the isotropic melting transition as measured by DSC.

In addition, we fitted stretched exponential functions similar to equation 2.2.3 to QENS data of these polymers as well as poly(3-octylthiophene) (P3OT) and poly(3-decylthiophene) (P3DT). Data was collected from the backscattering spectrometer (BASIS) at Oak Ridge National Labs as well as from the High Flux Backscattering Spectrometer (HFBS) at NIST. We used a modified version of equation 2.2.3 to fit the QENS data:

$$I(Q,t) = (1 - I_0)\exp\left[-\left(\frac{t}{\tau}\right)^{\beta}\right] + I_0 \qquad (2.2.5)$$

Here, I_0 corresponds to the set of relaxations that are not "visible" to the instrument used to collect the QENS data. The I_0 term can be considered as a second stretched exponential function that corresponds to relaxations that are either faster or slower than the relaxations detected by the instrument, and larger values of I_0 correspond to more relaxations outside the energy resolution of the instrument. Figure 2.2.3 shows the parameters extracted from the fits of the modified KWW function. A β value of 0.5 was used for all of the fits. The quality of the KWW fits is shown in figures A20-A24. Figure 2.2.3 shows that the characteristic time scales for relaxations observed decreases as a function of increasing Q, temperature, and side-chain length. It is also clear when examining the fits, that while equation 2.2.5 captures the general behavior of the experimental data, it insufficiently captures the changes in curvature, especially at short times ($t < 100$ ps). These subtleties in the experimental QENS data highlight differences in conjugated polymer dynamics compared to "traditional" polymer systems. For example, the comb-like nature of poly(3-alkylthiophene)s result in constraints due to increased excluded volume effects from neighboring side-chains, as well as the relative immobility of the backbone compared to the side-chain due to pi-orbital interactions. Therefore, it is by no means clear which relaxations are being captured within the characteristic time scales extracted from these fits. For P3BT and P3DDT, even when varying the β value, fits of the QENS data using equation 2.2.5 were insufficient to capture the relaxations observed (Figures A25 and A26). This strongly motivates the use of MD simulations to validate QENS data, as validated simulations can be used to identify specific motions contributing to the data.

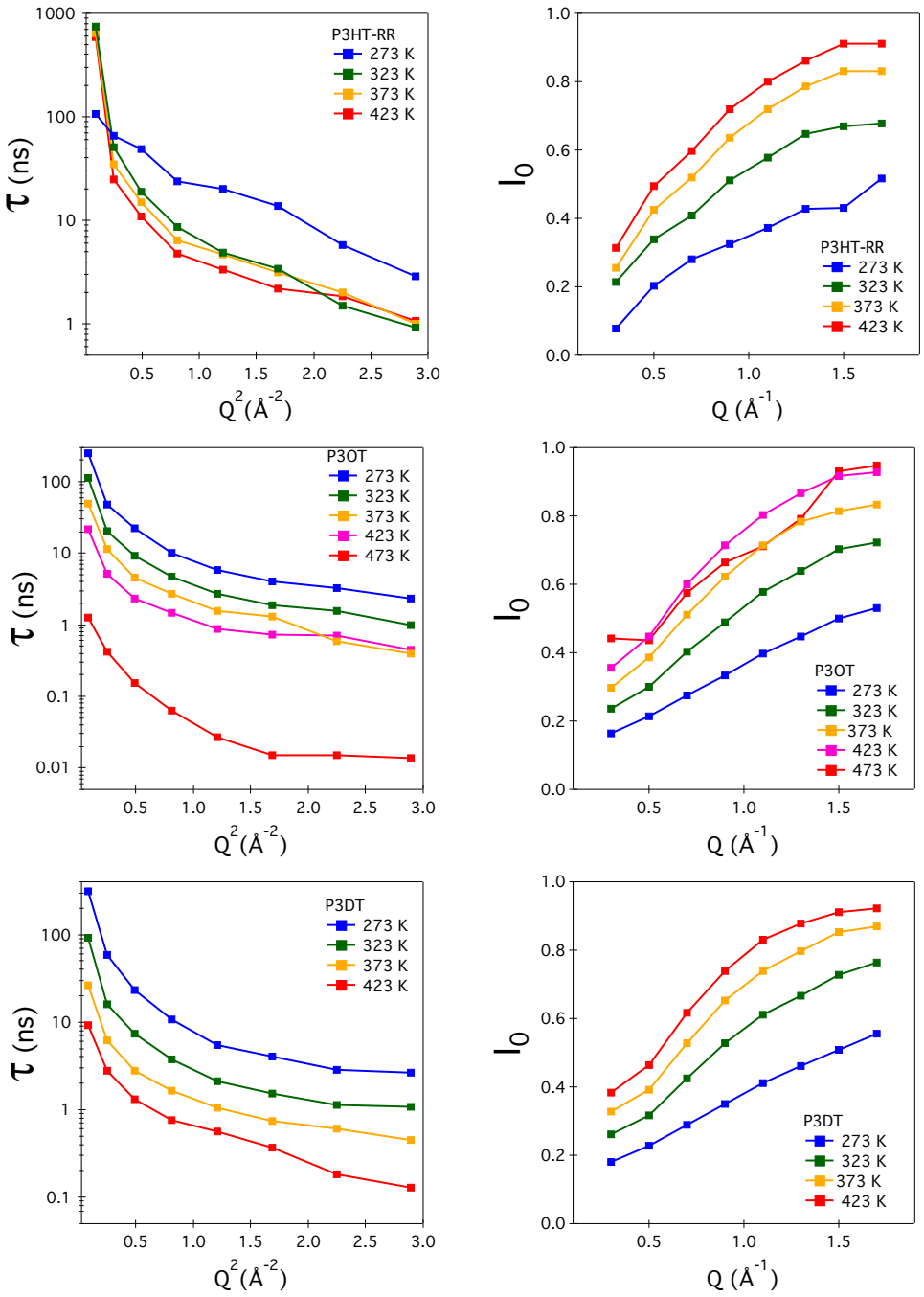

Figure 2.2.3: Characteristic relaxation times (τ) and constants (I_0) from fits of equation 2.2.5 to QENS data of P3HT-RR, P3OT, and P3DT.

2.3 Nuclear Magnetic Resonance Spectroscopy

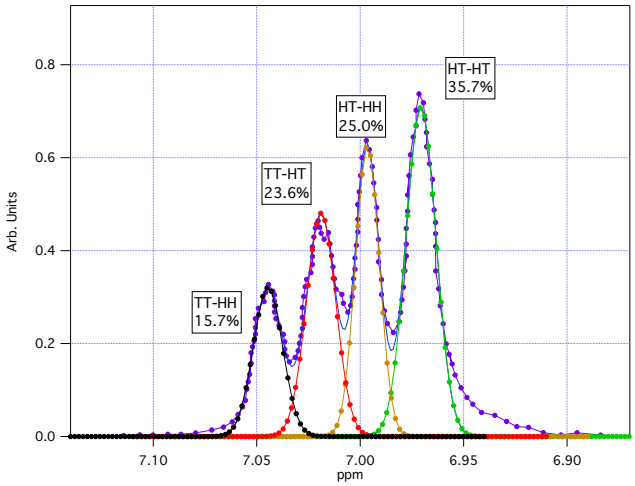

Figure 2.3.1: NMR spectrum of P3HT-RRa as well as Gaussian fits to peaks corresponding to different head-to-tail configurations.

Nuclear magnetic resonance (NMR) spectroscopy is an experimental technique that takes advantage of the magnetic properties of atomic nuclei to obtain information about the molecules that make up the sample[30]. While any material containing nuclei with magnetic spin can be used, organic molecules are commonly used due to the well-defined magnetic moments of ^{1}H and ^{13}C isotopes. Samples are placed in an environment with a uniform magnetic field, and a radio pulse is applied. The 'response' of the sample comes from the magnetic resonance of nuclei within the sample and it is recorded via radio receivers[30]. Although organic molecules contain an abundance of carbon and hydrogen, it is possible to obtain their detailed chemical structures. This is because variations in local environment of different carbon and hydrogen atoms will cause slight deviations in their resonance frequencies (relative to an arbitrary standard)[30]. These 'chemical shifts' allow specific chemical moieties to be identified. In the case of P3HT, some of these shifts correspond to carbon atoms that are arranged in specific configurations based on the regioregularity of the polymer[31]. An NMR spectrum of the regio-random P3HT was

acquired from Rieke metals. The peaks ranging from 6.90 to 7.10 ppm were fitted to Gaussian functions and their areas were calculated to determine the percentage of various head-to-tail configurations that were present in the sample, shown in Figure 2.3.1. This allows for regio-random chains to be constructed *in-silico* so as to have the same relative ratios of head-to-tail configurations. Other NMR techniques, such as dynamic NMR, can provide information about the dynamics of the system on time scales ranging from milliseconds to minutes[32].

2.4 Gel Permeation Chromatography

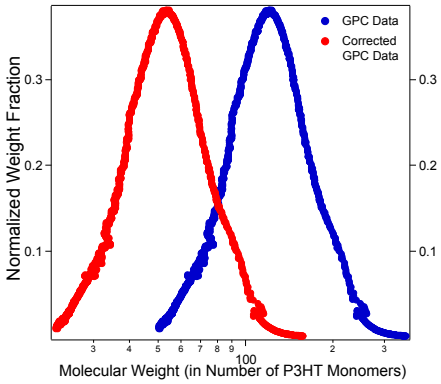

Figure 2.4.1: Normalized weight fraction calculated from GPC data versus molecular weight (in number of monomers)

Gel permeation chromatography (GPC) is used to characterize the molecular weight distribution of polymers[33]. The polymer is dispersed in a solvent (the mobile phase), and it is eluted through a column consisting of a porous gel (the stationary phase). The smaller chains will elute more quickly because they can more easily pass through the pores[33]. The rate at which the polymer exits the column is determined through the use of a detector sensitive to the polymer concentration. The data is usually obtained as a plot of signal intensity (whose source can vary depending on the concentration-measuring instrument used) as a function of elution time, from which the molecular weight distribution of the polymer sample is obtained. GPC was run using a universal method

with polystyrene MW standards[34]. Liu and coworkers have shown that P3HT run in GPC with a polystyrene standard overestimates the MW by a factor ranging from 1.5 to 2.[35] Figure 2.4.1 shows the normalized molecular weight distribution as a function of the number of P3HT monomers after correcting for the overestimation of MW.

2.5 Differential Scanning Calorimetry

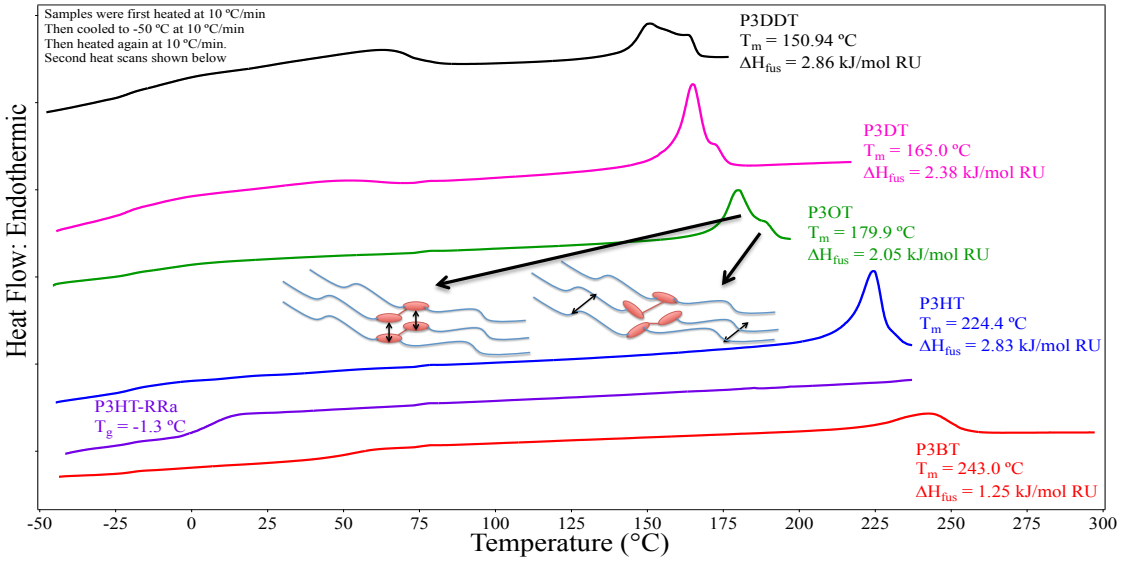

Figure 2.5.1: DSC thermograms of P3ATs with melting temperatures and latent heats of fusion labeled. The arrows point to cartoon representations of the polymer melting process for polymers with longer side-chains. The slight feature observed at ~75 °C for all data is an artifact of the instrument.

Differential scanning calorimetry (DSC) is used to identify phase transitions—such as the glass and melting transitions—occurring in polymer systems[36]. The instrument measures the heat needed to increase the temperature of a sample at a specific rate relative to a reference sample. Glass transitions represent a change in a polymer from glassy to rubbery phases, and it is represented by a sigmoid-like change on the DSC thermogram[36]. The melting transition indicates a change in the polymer phase from crystalline to liquid-amorphous, and is represented by a peak on the DSC thermogram. The area under this peak corresponds to the latent heat required for the phase transition to

occur[36]. Figure 2.5.1 shows the DSC thermograms of five different P3ATs with side-chains of varying length. As the length of the side-chain increases from four carbon atoms (P3BT) to twelve carbon atoms (P3DDT), the melting peak shifts to lower temperatures. The longer side-chains provide increased configurational entropy, which corresponds to less heat required for entropic effects to match the crystalline lattice dissociation enthalpy[37]. Additionally, a shoulder appears in the melting peak and becomes more prevalent. This corresponds to the formation of a semi-ordered, or liquid crystalline, phase in which the pi-stacking of the thiophene rings has been broken, but the side-chains are still loosely aligned so as to minimize steric interactions and maintain a general anisotropy. Adding additional heat causes the loosely ordered polymer to transition to a fully isotropic melt phase. The features observed for P3DT and P3DDT between 50 °C and 75 °C correspond to melting of the side-chains[37]. These transitions have been previously reported for comb-like polymers with alkyl side-chains that consist of at least ten carbon atoms[37].

2.6 Density Measurement

Density is an important thermodynamic property used to validate simulations of conjugated polymers. The density of P3HT-RRa was measured by heating the polymer powder to the melt state in a vacuum oven (1.0 mbar) for over 8 hours. At the beginning of this period, bubbles were initially observed coming off the melt state polymer, but none were observed by the end, indicating that there were no air pockets remaining in the material. Still under vacuum, the polymer was cooled into a pellet. The pellet was placed in a test tube containing glycerol where it floated due to its lower density. The test tube was then placed in a water heat bath to maintain a constant temperature. Water was

slowly added to the test tube until the pellet maintained neutral buoyancy in the mixture. The density of the liquid mixture was then measured using a portable density meter (Anton Paar DMA 35) to determine the density of the pellet. Similar techniques (i.e. density columns) have also been used to obtain the density of regio-random P3HT[38].

Chapter 3: Computational Methods for Conjugated Polymer Characterization

Computational methods provide a powerful means for analysis of conjugated polymer systems because they utilize a bottom-up approach to characterization. For example, *ab initio* methods, which approximate the electronic degrees of freedom in a molecule, can be used to model charge transport phenomena on the molecular scale[39]. Molecular dynamics (MD) simulations provide a clear picture of the molecular configurations and dynamics occurring in the bulk system[40]. Here, we will explain the MD simulation process and the information that can be obtained from these simulations. We will also focus on how *ab initio* methods are used to parameterize MD force fields.

3.1 Molecular Dynamics Simulations

An atomistic molecular dynamics (MD) simulation is a computer simulation in which trajectories of the molecules making up the system are determined as a function of time[40]. The system consists of a set number of particles that represent the atoms of each molecule. One of the main assumptions that goes into an MD simulation is that the interactions occurring between molecules—which are actually governed by the movement and interaction of the electrons in the molecule—are determined through classical mechanics (i.e. Newton's Laws of motion)[40]. Essentially, an MD simulation trajectory is created by evaluating the force applied on each atom in the simulation and then integrating the equations of motion in order to update the positions of the atoms after a set amount of time[40]. The trajectory is then a set of lists of atomic coordinates corresponding to each time step. The forces are calculated based on a potential energy function that describes the ground state interactions of each atom. The simulation is initialized by placing the molecules into a 'simulation box' followed by assigning initial

velocities to each atom. Excess energy can be accidentally propagated during this step if atoms are placed near to each other so as to create strong repulsive forces, resulting in the simulation 'blowing up'[40]. To mitigate this, an energy minimization step is performed, during which the atomic positions are slightly shifted so as to avoid these types of interactions. The simulation then runs until the specified time has passed. MD simulations can be run under different constraints corresponding to different ensembles. For example, with the aforementioned steps, the simulation would generate a trajectory in the microcanonical ensemble (also known as an NVE ensemble), which refers to a fully isolated system in which the number of particles, volume, and energy is specified. Given that we wish to calculate parameters from the simulation that will eventually be compared to experimental data, a trajectory can also be generated in an isobaric-isothermal, or NPT, ensemble, in which the number of particles, the temperature, and the pressure of the system are all held constant. This is achieved by applying a thermostat and barostat to the simulation. Finally, in order to simulate a bulk system, it is advantageous to apply periodic boundary conditions. When an atom passes through the edge of the simulation box with periodic boundary conditions applied, it wraps back around to the opposite side of the box with the same velocity. Essentially, the simulation box is surrounded by mirror images in all faces[40].

3.2 Molecular Dynamics Force Fields

A key parameter that is utilized in an MD simulation is the potential energy function—also known as the force field—that is used to calculate the forces acting on each atom. These force fields usually take the following form[41]:

$$U = \sum_{bonds} \frac{1}{2} k_b (r - r_0)^2 + \sum_{angles} \frac{1}{2} k_a (\theta - \theta_0)^2 + \sum_{torsions} \frac{V_n}{2} [1 + \cos(n\phi - \delta)] + \sum_{imp} V_n + \sum_{LJ} 4\epsilon_{ij} \left(\frac{\sigma_{ij}^{12}}{r_{ij}^{12}} - \frac{\sigma_{ij}^{6}}{r_{ij}^{6}} \right) + \sum_{elec} \frac{q_i q_j}{r_{ij}} \quad (3.2.1)$$

Here, the first two terms are harmonic potentials used to approximate the intra-molecular contributions of bond stretching and bending. These are relatively steep potentials that assume equilibrium bond and angle values (r_0 and θ_0) from which only minor deviations will occur. The next two terms account for energy contributions due to torsional motions within a molecule. The final two terms account for intermolecular interactions. The first term is a Lennard-Jones potential that accounts for Born repulsion (the r^{-12} term) and Van der Waals attraction (the r^{-6} term). The second term accounts for electrostatic (Coulombic) interactions between atoms for which charges have been assigned.[41]

In this work, the force fields used to simulate P3HT are all based on the OPLS-AA force field, but they are further modified in order to account for the effects of electron delocalization and pi-orbital interactions. Major modifications were made to the torsion potentials and the partial charges assigned to the backbone, which were parameterized using *ab initio* methods. The manner in which the new potentials and partial charges are determined can vary greatly depending on the specific method used by a research group. For example, Bhatta and coworkers parameterized P3HT torsion potentials by running a series of single point calculations[29]. A single P3HT decamer was simulated in vacuum. First, a geometry optimization was run in order to get the lowest energy conformation of the molecule. Next, a single torsion angle was varied while the rest of the molecule was constrained, and the energy was calculated as a function of torsional angle. This process was repeated for all of the carbon-carbon bonds in the P3HT side-chain for which torsional motions were possible, as well as the bond linking the

thiophene rings. The restrained electrostatic potential (RESP) fitting method was used to calculate the atomic partial charge values used in the force field[29]. For this calculation, a net charge neutrality condition was applied to the entire chain, and the electron density of the middle monomers were used for the RESP fitting. Therefore, these partial charge values correspond to electron densities of thiophene monomers with the charges delocalized over several neighboring conjugated units. The torsional calculations were conducted at the B3LYP/6-31+G(d,p) level, and the electron density used to determine the partial charges was evaluated at the MP2/6-31+G(d,p) level. The force field was validated by running simulations of crystalline P3HT and calculating melting and glass transition temperatures, surface tension, and mass density for comparison with experimental data[29].

Moreno and coworkers applied a similar strategy when parameterizing their MD force field[28]. Unlike Bhatta, they performed torsion potential calculations for only the inter-ring bond and the bond connecting the side-chain to the thiophene ring. Furthermore, they calculated 'intrinsic' torsion potentials by removing the effects of all other interactions. After calculating torsional energies using *ab initio* methods, they recalculated the energies of the same configurations with a molecular mechanics force field where the torsion potential for the bond of interest was set to 0. This meant that the energy changes calculated would result from all interactions except for the torsional interaction. By taking the difference between the *ab initio* torsional energy and the energy calculated from the molecular mechanics force field, they obtained an intrinsic torsion potential[28]. The calculations were carried out on a series of different thiophene tetramers at the B3LYP/6-311G** level. Three separate force fields were developed, with the only

variation in the force fields coming from the atomic partial charges used. Moreno FF1 uses partial charge values obtained from OPLS-AA. The partial charges in Moreno FF2 were determined by using an electrostatic potential (ESP) fitting method based on electron densities also evaluated at the B3LYP/6-311G** level. The electron density calculations were carried out with charge neutrality enforced over a single monomer, unlike the calculation made by Bhatta and coworkers, for which this same condition was enforced over the entire chain. It is therefore more likely that the charge distribution obtained by Moreno and coworkers is closer to the distribution seen in monomers with broken conjugation, where the charges are fully localized. Moreno FF3 uses the arithmetic mean values of the partial charges used in FF1 and FF2. FF3 also showed the best overall agreement in the benchmarking experiments that Moreno and coworkers conducted, which involved molecular mechanics and molecular dynamics simulations of crystalline poly(3-butylthiophene) (P3BT) and poly(3-(S)-2-methylbutylthiophene) (P3MBT)[28]. The simulations confirmed that the lowest energy conformations of these polymers matched the experimentally reported crystal structures.

Huang and coworkers implemented a similar approach to Moreno, but used a oligomer consisting of 14 P3HT monomers in their calculation of the backbone torsion potential[42]. However, rather than subtracting out the other contributions to the total torsional energy calculated from *ab initio* methods, they iteratively adjusted the intrinsic potential. They ran high temperature NVT simulations, and calculated the distribution of backbone torsion angles, adjusting the intrinsic torsion potential until the population reflected the expected population from the full *ab initio* derived torsion potential (which included all contributions to the torsional energy). They used a set of atomic partial

charges calculated by Marcon and Raos for tetrathiophene[43]. Interestingly, they did not calculate a torsion potential for the bond linking the side-chain to the thiophene ring so that this was left as a freely rotating joint. They ran MD simulations of P3HT and calculated the mass density for comparison with experimental results[42]. Further investigations of the force fields discussed here are presented in Chapter 4.

3.3 Calculating Parameters from MD Trajectories for Experimental Validation

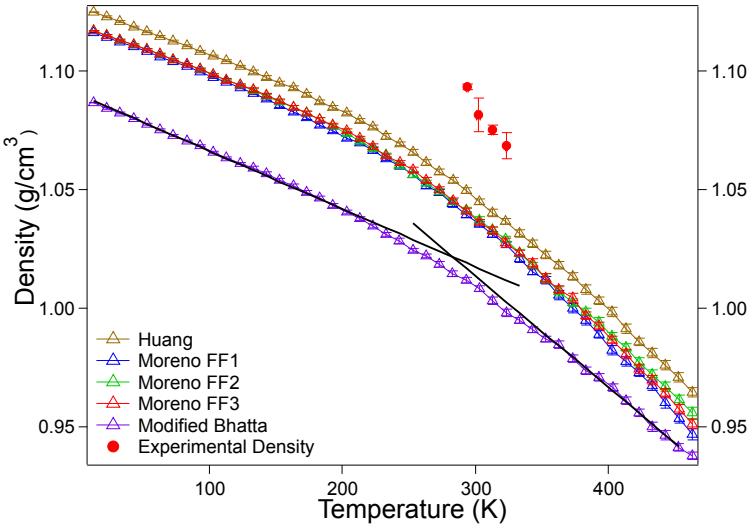

Figure 3.3.1: Densities of different MD simulations of P3HT-RRa as a function of temperature. The red points denote the experimental density of P3HT-RRa measured using a neutral buoyancy technique. The solid lines correspond to linear fits of the densities above and below the glass transition for each simulation. The point at which the lines intersect corresponds to the glass transition temperature for the simulated system.

Figure 3.3.1 shows densities of the simulated systems that were calculated as they were being cooled, providing another benchmark for validation of MD simulations. The location of the change in slope observed (between 200K and 300K) is used to denote the glass transition of the simulated system. All three Moreno force fields have close to the same glass transition. DSC results show a glass transition for the experimental system at 277 K (See Figure A8), which is in a good agreement with simulation result using Mod.

Bhatta FF (Table 3.1). The density calculated from the simulation run using the Huang FF also shows the closest agreement with the experimental density, which was determined to be 1.090 g/cm at room temperature, which is in good agreement with previously reported values for P3HT-RRa[38,44].

Table 3.1 Glass Transition Temperatures of P3HT-RRa determined through DSC measurements and calculated from MD simulations run with different force fields.

System	Glass Transition Temperature (K)
Experimental	277 ± 5
Mod. Bhatta	283 ± 15
Moreno FF1	247 ± 15
Moreno FF2	254 ± 15
Moreno FF3	252 ± 15
Huang	319 ± 15

In addition to calculating thermodynamic properties (e.g. density) for comparison with experimental data, the static and dynamic structure factors can be directly calculated from MD simulations and compared to X-ray and neutron scattering data. This was done using the software nMoldyn[45]. Given a molecular dynamics trajectory, the software evaluates equation 2.2.4 after taking in certain additional inputs. Essentially, the algorithm computes the intensity given in equation 2.2.4 for a specific set of Q values specified by the user. The algorithm iterates over each atom in the trajectory (or a specific subset if desired), and includes other atoms in the pairwise calculation if they lie on the surface of the sphere corresponding to each Q value. In addition to specifying the Q values, the user also sets a tolerance, called the 'Q-shell width'. The purpose of this is to include more atoms in the evaluation of equation 2.2.4, as the number of atoms that lie exactly on the surface of the sphere may be insufficient to generate a scattering curve that accurately represents the bulk system[45]. Equation 2.2.4 can be evaluated as a function of

time by specifying the time-steps corresponding to the frames of interest in the MD trajectory, yielding a dynamic structure factor. The static structure factor is calculated by averaging equation 2.2.4 over the entire trajectory. Additionally, nMoldyn can apply weights to the atomic contributions to the static and dynamic structure factors to approximate different experimental results. For example, X-ray static structure factors presented in this work are created by weighting the contributions of each atom in the trajectory by its atomic number, which approximates the differences in electron density that will affect WAXS measurements[10,45]. Similarly, the dynamic structure factors are calculated by weighing the contributions of each atom by its incoherent scattering cross section[10,45].

Chapter 4: Critical Assessment of Molecular Dynamics Simulations for Amorphous Poly(3-hexylthiophene) using Neutron and X-ray Scattering Experiments

The work presented in this chapter has been submitted to RSC Nanoscale (2016).

4.1 Introduction

Conjugated polymers have emerged as a highly relevant class of materials driven by the demand for conducting and semi-conducting devices that are inexpensive, lightweight, and flexible.[2–4] The majority of these organic materials consist of monomer units comprised of a conjugated backbone modified with alkyl side chains to increase solubility. Charges can travel along the length of a single chain or by hopping from chain to chain via pi-orbital overlaps between conjugated backbones when they are in close proximity (e.g. pi-stacking). Since the first conjugated polymers were synthesized, it has been shown that polymer nanostructure plays a significant role in determining which of these processes limits charge transport.[11,46] For example, bulk regio-regular poly(3-hexylthiophene) (P3HT-RR) consists of both crystalline and amorphous domains, and it is well known that transport along amorphous regions is the rate limiting step for these systems.[47]

Recently, investigations have aimed to also decipher the role of polymer dynamics in charge transport. Since the characteristic length and time scales for charge transport are of the same order of magnitude as dynamic fluctuations of the polymer chains, it is anticipated that these would play an important role.[21,48] For example, conjugated polymers are a material of interest for thermoelectric applications due to high electron-phonon coupling and electron-phonon scattering.[4] Additionally, the time scales for exciton thermalization and recombination in organic bulk heterojunction solar cells is

in the ps to ns range, which correspond well to the time scales of polymer fluctuations.[48] Moreover, polymer fluctuations become increasingly relevant at anticipated device operating temperatures, which are usually well above the glass transition temperature for these materials so that significant molecular mobility is anticipated.[37]

The combination of quantum mechanics calculations with either molecular dynamics (MD) or Monte Carlo (MC) simulations is one strategy that has been used extensively to study the effect of dynamic disorder on charge transport for these materials.[49] These works usually involve the use of MD or MC simulations to equilibrate a conjugated polymer system. The charge transport properties of the system are then calculated using quantum mechanical methods on specific frames obtained from the MD or MC simulation. McMahon and coworkers studied the effects of dynamic disorder on the crystalline P3HT, equilibrating the system via an MD simulation at 300K and 1 atm.[19] They noted that charge traps formed in regions of high backbone planarity with lifetimes on the order of ten picoseconds in crystalline P3HT. They also determined that the addition of defects in regioregularity to the crystalline system had no influence on the location or depth of the charge traps. Vukmirovic and cowokers also studied crystalline P3HT, using MC simulations to separately examine the effects of side-chain and backbone disorder on the electronic density of states (DOS).[50,51] They concluded that both side-chain and backbone disorder contributed to broadening of the DOS near the valence band edge and that backbone disorder played a larger role in increasing charge localization. For the case of amorphous P3HT, they found that the primary contributions to charge localization come from the electrostatic potentials of the backbone units, which influence their relative position and orientation, which in turn affects inter-chain pi-

orbital overlap[50]. Poelking and coworkers also investigated the effect of regio-regularity on charge transport in P3HT using this approach.[52] They calculated time autocorrelation functions for two parameters that affect charge transport according to the Marcus theory of charge transport, which is related to charge transfer integrals and hopping site energies. They determined that the time scales for the decorrelation of these parameters was in the ps to ns range for fully regio-regular P3HT. Counterintuitively, their results indicated that decorrelation time scales for the 90% regio-regular system were longer than those of the fully regio-regular system.[52] Because these methods use snapshots of trajectories obtained from MD and MC simulations, their ability to describe charge transport that is representative of the bulk material hinges on the accuracy of the parameters used when running the simulations. However, high uncertainty still remains as to how *in silico* system parameters, such as crystallinity, molecular weight, and equilibration methods affect the segmental dynamics of P3HT in the solid-state. Furthermore, there is limited agreement between the methods used when calculating MD force field parameters for conjugated polymers. This work aims to address these questions by using wide-angle X-ray scattering (WAXS) and quasi-elastic neutron scattering (QENS) techniques to critically evaluate the results of MD simulations for P3HT.

QENS experiments provide quantitative information about the dynamics of materials at molecular length scales. In comparison to other polymer systems, relatively few QENS experiments of conjugated polymers have been performed. Obrzut and Page related the dynamics of regio-regular P3HT to its conductivity by comparing QENS data with dielectric spectroscopy data.[22] They observed a "liberation" of the side-chains at

~175 K, with an activation energy for these motions of ~9 kJ/mol, and with a corresponding change in the conductivity of bulk P3HT at this temperature. Paterno and coworkers observed that the dynamics of P3HT-PCBM films were unaffected by the solvent used to make the film.[23] They additionally determined that increasing the PCBM concentration in the film increased the time-scales for the observed dynamics. They hypothesized that the longer time scales resulted from increased P3HT side-chain confinement caused by steric interactions with PCBM. Etampawala and coworkers also performed QENS measurements of P3HT/PCBM solvent-cast films[24]. They verified the results of Paterno and coworkers, and further examined the Q dependence of the P3HT side-chain dynamics. For length scales greater than 7 Å, they observed dynamics dominated by simple diffusion, and attributed these dynamics to collective motions of the side-chain. The dynamics corresponding to length scales smaller than 6 Å were attributed to motions within the side-chain (i.e. methyl rotations).[24]

QENS measurements and MD simulations are complimentary techniques. QENS provides information about the dynamics of specific fragments of the experimental system (e.g. self-correlation of motions for hydrogen atoms). On the other hand, MD simulations provide detailed information about all aspects of the system, but this information is only meaningful if the simulations are experimentally validated and determined to be accurate. QENS also provides a powerful method for validating MD simulations since the measured scattering from an experiment can be directly compared to simulated scattering data, which is calculated from the MD trajectories. Traditional methods of MD simulation validation usually involve the use structural and thermodynamic properties such as heat capacity, surface tension, glass transition

temperature, melting temperature or mass density to validate force field parameters. However, these benchmarks may not provide correct information about localized molecular fluctuations since the benchmark parameters are calculated by time averaging. In contrast, simulations validated with QENS experiments provide ample quantitative information about the dynamics of the system at various length scales and time scales that correspond to specific molecular motions. Richter, Colmenero, and Arbe *et al*. proposed the use of quasi-elastic neutron scattering to directly validate MD simulations of polymers to obtain a clear understanding of polymer dynamics.[15,21] For example, they were able to validate MD simulations of poly(alkyl oxides) (PAOs) that were run using the COMPASS force field.[53,54] After validating the simulation, they were able to identify the contributions from different methyl groups to the overall dynamics and determine characteristic relaxation times for backbone and side-chain motions separately. They have conducted similar analyses on poly(n-alkyl methacrylates), which showed reduced localized motions due to increased side-chain confinement relative to PAOs.[55] Only two combined QENS-MD studies have been conducted on conjugated polymers. Sniechowski and coworkers adopted this method when investigating the dynamics of polyaniline (PANI) doped with the plasticizing dopant di-(2-butoxyethoxyethyl) ester of 4-sulfophthalic acid (DB3EPSA).[25–27] They investigated the change in the mean-squared displacement of protons in the dopant as a function of time and found that the time scales for relaxations of different dopant protons spanned several orders of magnitude. They observed that the protons closest to the PANI chains had the longest relaxation times, confirming that the polymer chains were effectively stationary with respect to the dopant. Guilbert and coworkers adopted the method used by Colmenero for P3HT-RR and regio-

regular poly(3-octylthiophene).[56] They were able to demonstrate that QENS could be used to validate MD simulations of these materials and determined activation energies for different motions in these complex systems.

In this work, we further explore this new approach by performing multiple MD simulations of regio-random P3HT (P3HT-RRa) in order to quantitatively compare the impact of different simulation parameters on the dynamics of P3HT-RRa in the bulk solid-state. Regio-regular P3HT consists of both crystalline and amorphous regions, which require increased computational resources to simulate very large systems that include adequate samples of the two domains.[57] Additionally, simulating a multi-phase system significantly increases the parameter space for the problem, as both the relative amounts of crystalline and amorphous domains, the interfacial area between the domains, and the fact that polymer chains can coexist in both phases need to be taken into account. For these reasons, we chose to focus on regio-random P3HT because it is fully amorphous at all temperatures. This ensures that differences in the structure and dynamics of different simulations arise mainly from the parameters that are used in each simulation (i.e. force-fields, equilibration). QENS and WAXS data are used to assess the accuracy of individual MD runs in order to develop guidelines for future simulations conjugated polymer systems. Figure 4.1.1 shows the overall approach used in this work. The work rigorously evaluates force-field independent system parameters such as system structure (i.e. crystalline vs amorphous), alternative equilibration methods, and molecular weight. Moreover, five different MD force-fields that have been parameterized specifically for poly(3-alkylthiophene)s using *ab initio* methods are compared for accuracy and the parameters that cause the most significant differences are identified.

Finally, we investigate the effects of dynamic fluctuations on charge transport parameters (e.g. the charge transfer integral and conjugation length), and assess the applicability of validated force fields for use in other poly(3-alkylthiophene) systems.

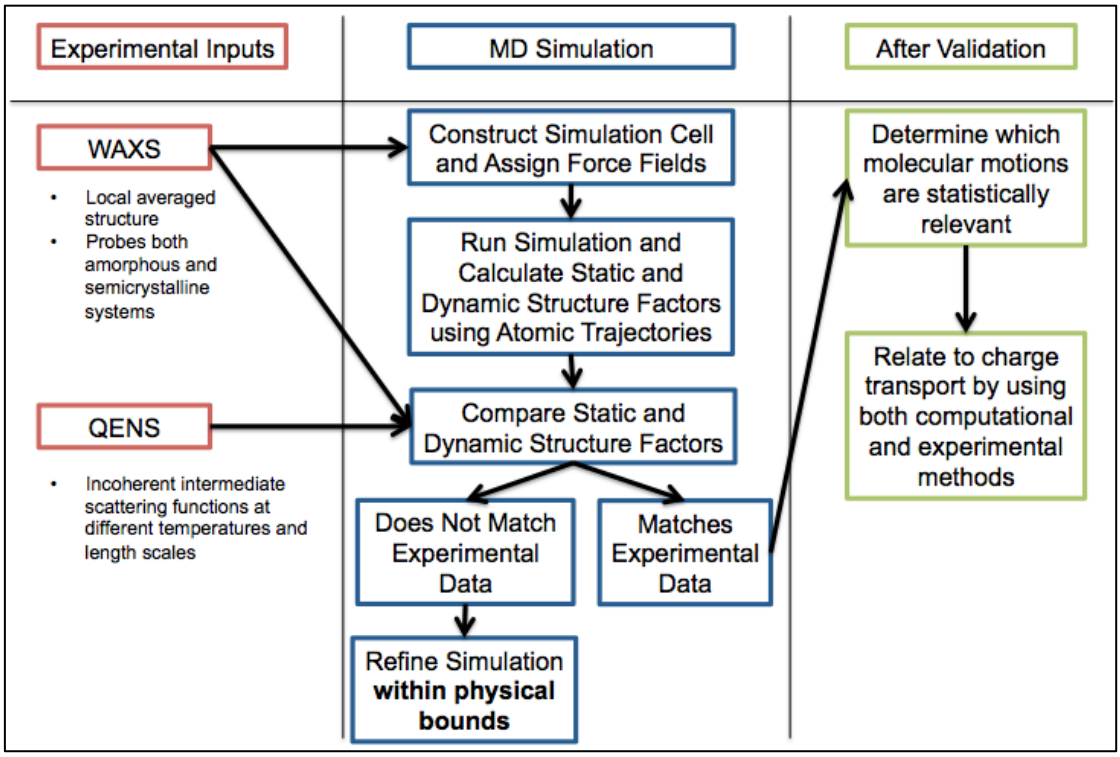

Figure 4.1.1: Flowchart depicting the method used to validate MD simulations using QENS and WAXS. Validated simulations provide information about the material that can be related to charge transport properties.

4.2 Materials and Methods

4.2.1 Materials

Regio-random P3HT (P3HT-RRa) (Reg 93%, M_w = 31 kDa, PDI = 1.5), regio-regular P3HT (P3HT-RR) (M_w = 39 kDa, PDI = 2.3) and regio-regular Poly(3-dodecylthiophene-2,5-diyl) (P3DDT) (M_w = 57 kDa, PDI = 2.1) were purchased from Rieke Metals. NMR (Figure 2.3.1), DSC (Figure A8), Density (Figure 3.3.1), and GPC (Figure 2.4.1) measurements were performed on P3HT-RRa and experimental details and data for these measurements are included in the supporting information.

4.2.2 Wide-Angle X-Ray Scattering (WAXS)

WAXS samples were prepared by placing polymer powder between two 10 μm thick layers of Mylar and melting the powder into a thick film (~1 mm) that was then placed in the path of the X-ray beam. A thermocouple was put in contact with the polymer that was not exposed to the X-Ray beam to accurately record temperature. An X-Ray scattering instrument (Anton-Paar, Graz, Austria) with a Cu-Kα source (1.54 Å wavelength) was used in line collimation mode. Fujifilm (Greenwood, SC) image plates and a PerkinElmer Cyclone (Covina, CA) image plate reader were used to acquire the data. The 2-D scattering images were reduced into 1-D plots of intensity (I) versus scattering vector (q) using the SAXSQuant software.

4.2.3 Quasi-elastic Neutron Scattering (QENS)

Polymers were melt processed over aluminum foil to produce films ~0.1 mm thick that maximize scattering intensity without multiple scattering. The polymer powder was placed in aluminum pouches and melted at 538 K in an argon glove box. While in the melt state, the polymer was spread evenly across the surface area of the pouch to ensure full coverage. The pouch was then folded and a large heated aluminum block (~ 2.3 kg) was place on top of the pouch to reduce heterogeneity in the film thickness. The samples were then cooled to room temperature at a rate of ~10 K/min. QENS measurements were carried out using three different instruments: the Backscattering Spectrometer (BASIS) at the Spallation Neutron Source (SNS) at Oak Ridge National Laboratory[58], the Disk Chopper Spectrometer (DCS)[59] at the NIST center for Neutron Research (NCNR), and the High Flux Backscattering Spectrometer (HFBS)[60] also located at NIST. DCS is sensitive to energy transfers corresponding to time scales ranging from

0.1-10 ps, while BASIS and HFBS probe time scales ranging from 10-1000 and 100-4000 ps, respectively. DCS and BASIS data were collected over Q values ranging from 0.3 to 1.9 $Å^{-1}$, while HFBS data ranged from 0.3 to 1.7 $Å^{-1}$. QENS scans were run for each instrument at 273 K, 373 K, 423 K, and 473 K. Data reduction and Fourier transformation of the data, from the frequency domain to the time domain, was performed using the Data Acquisition and Visualization Environment (DAVE) software[61] and the Mantid software[62] developed by the NCNR and SNS, respectively.

In a QENS experiment, the quantity measured is the double differential scattering cross section, which denotes the probability of measuring a neutron scattering event with a change in energy $d\hbar\omega$ into solid angle $d\Omega$.[10,15,21] It is closely related to $S(Q, \omega)$, the observed intensity as a function of the scattering vector Q and frequency ω. The double differential scattering cross section has both coherent and incoherent contributions, which are related to the coherent and incoherent scattering functions weighted by the scattering cross section of each isotope that makes up the sample, $\sum_{\alpha,\beta} \overline{\boldsymbol{b_\alpha b_\beta}}\, \boldsymbol{S^{\alpha,\beta}_{coh}(Q,\omega)}$ and $\sum_{\alpha} \overline{\boldsymbol{\Delta b^2_\alpha}}\, \boldsymbol{S^{\alpha}_{inc}(Q,\omega)}$. These are related to the intermediate scattering functions $\boldsymbol{I^{\alpha,\beta}_{coh}(Q,t)}$ and $\boldsymbol{I^{\alpha}_{inc}(Q,t)}$ and to the van Hove correlation functions $\boldsymbol{G_{\alpha,\beta}(r,t)}$ and $\boldsymbol{G_{\alpha}(r,t)}$ via Fourier transforms. b_α and b_β refer to the neutron scattering lengths for isotopes α and β, and Δb_α^2 is the neutron scattering cross section for isotope α. Thus, the coherent and incoherent scattering functions provide information about the pair and self motions of the atoms in the sample, and the atomic composition of the sample determines the extent to which these contributions will dominate the scattering.[10,15,21] Since hydrogen has an incoherent neutron scattering cross section (Δb_α^2) that is almost two orders of magnitude higher than that of all other atoms, the QENS signal for this system is greatly dominated

by dynamic fluctuations of hydrogen atoms.[10] For P3HT, the incoherent contributions from hydrogen atoms amount to 93% of the total QENS signal (calculated by taking the ratio of the incoherent scattering cross section from all hydrogen atoms in a monomer of P3HT to the total scattering cross section of a P3HT monomer). This means that the QENS signal for P3HT is dominated by self-motions of the alkyl side-chain, since ~93% of the hydrogen atoms in a monomer of P3HT are located in the side-chain. Thus, the contribution of side-chain incoherent scattering to the QENS signal amounts to ~87%. However, it was observed *in silico* that the parameters affecting backbone motions also caused significant variations in time autocorrelation functions calculated for the side-chains (Figure A19). Although the QENS signal is mainly comprised of side-chain fluctuations, these motions are in turn heavily influenced by the backbone and cannot be easily decoupled from the backbone motions.

QENS data was taken in the energy domain and is Fourier transformed to the time domain so as to remove the effects of instrument resolution via the following formula:[56]

$$\boldsymbol{I(Q,t) = \frac{\int S(Q,\omega) e^{i\omega t} dt}{\int R(Q,\omega) e^{i\omega t} dt}} \qquad (1)$$

where $S(Q, \omega)$ is the measured intensity as a function of the scattering vector Q and frequency ω, and $R(Q, \omega)$ is the instrumental resolution function. Transforming the data into the time-domain allowed us to match data from multiple instruments to probe a broad range of time scales. This also simplified comparison to MD simulation results. Since QENS instruments have limited energy resolution, the experimental data had to be shifted vertically using overlapping time regions to match with each other and with the simulation data. Modelled QENS profiles are calculated directly from the trajectories of

the MD simulation. which is equivalent to measuring the QENS spectra on an instrument for which the energy transfer windows of the entire system can be fully resolved.[63]

4.2.4 Polarized Neutron Diffraction:

Spin-polarized neutron diffraction (ND) experiments were also carried out on the fully hydrogenated P3DDT sample using the D7 instrument at the Institute Laue-Langevin in Grenoble, France. Samples were prepared identically to those of QENS experiments and measurements were performed using standard configurations as described elsewhere[64]. ND experiments, like WAXS experiments, provide information about the structure of the sample, but do so through interactions with atomic nuclei in the sample rather than electron clouds. Therefore, partial deuteration can be used to highlight specific regions of the polymer sample.[64]

4.2.5 Molecular Dynamics Simulations

Molecular dynamics simulations were carried out using the LAMMPS Molecular Dynamics Simulator.[65] Figure 4.2.2 shows torsional force field parameters that showed significant variation across five different force fields published by Bhatta and coworkers[29], Huang and coworkers[42], and Moreno and coworkers.[28] All of these force fields were specifically parameterized for P3HT using different methods and validated against different criteria (e.g. crystal structure, density, surface tension, glass transition temperature and/or melting temperature). All force fields were based on the OPLS-AA force field with special modifications to account for the effect of conjugation.[66] These modifications consist of torsion potentials applied to the backbone and side-chain atoms as well as changes to partial atomic charges. All parameters are derived from calculations using post-Hartree-Fock methods or hybrid-density-functional-theory methods.[39] The

backbone torsion potential accounted for the increased rigidity of the polymer due to pi-conjugation between the neighboring monomers. The atomic partial charges are also modified to more accurately represent the distribution of charges that result from charge delocalization, as determined from first principles methods.

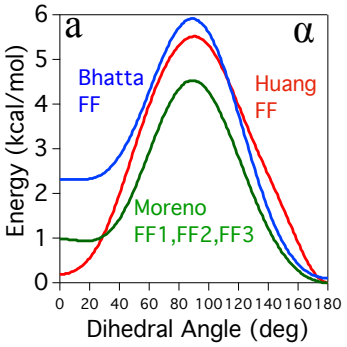

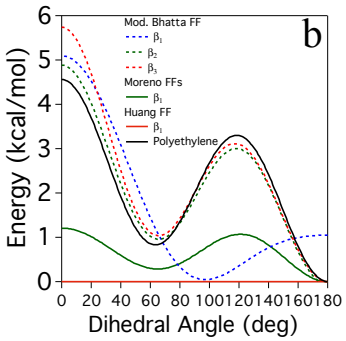

c	Bhatta	Huang	Moreno FF1	Moreno FF2	Moreno FF3
S1	-0.2171	-0.1496	+0.0180	-0.1200	-0.051
C1	-0.0441	+0.0748	-0.0090	0.0000	-0.0045
C2	+0.0318	-0.1817	0.0000	-0.0300	-0.0150
C9	-0.3128	-0.1817	-0.1150	-0.1800	-0.1475
C10	+0.1762	+0.0748	-0.0090	0.0000	-0.0045
C3	+0.1278	+0.0617	-0.1200	+0.0300	-0.0450
H7	+0.2356	+0.030	+0.1150	+0.1800	+0.1475
H1	+0.0039	+0.0600	+0.0600	+0.0600	+0.0600
Sum	+0.2356	0.0	0.0	0.0	0.0

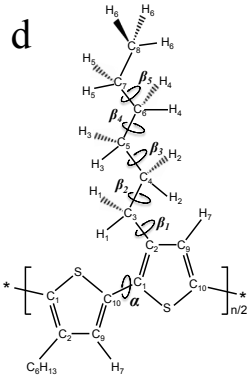

Figure 4.2.2: a) Backbone torsion potentials for force fields developed by Bhatta and coworkers[29], Huang and coworkers[42], and Moreno and coworkers.[28] B) Torsion potentials for the first three bonds in the side-chain for the same force fields. Dashed lines correspond to our re-calculation (this work) of the torsion potentials from Bhatta et.al. For all side-chain torsion potentials other than the first ($\beta_{2\text{-}5}$), the Huang FF and the Moreno FFs used the polyethylene torsion potential from OPLS-AA, represented by the black line. c) Atomistic partial charges used for the thiophene rings and the first side-chain methyl group for the five force fields (atom labels in Figure 4.2.2d) as well as the sum of the partial charges for an entire monomer unit. d) Atomic structure and class labels for a P3HT dimer. α represents the torsion angle between thiophene rings, and $\beta_{1\text{-}5}$ represent the torsion angles in the hexyl side chain.

A large discrepancy was noticed between the side-chain torsion potentials derived by Bhatta and coworkers and the potentials used by Moreno and Huang, with the most significant differences occurring for the first and second side-chain torsion potentials (β_1 and β_2). Bhatta and coworkers calculated the torsion barrier using a single point energy

calculation from an optimized P3HT dodecamer. It was noted that the side chain of a rotating monomer could intersect with neighboring side chains at low dihedral angles, accounting for steric repulsion between the side chains that resulted in very high torsion barriers at low torsion angles. Since steric interactions are also accounted for in the non-bonded Lennard-Jones repulsive component, applying this side-chain potential leads to an unrealistically rigid side-chain. To correct this, we repeated the *ab initio* calculation of Bhatta et.al. (B3LYP/6-31+G(d,p) level) while removing the side chains of neighboring monomers to avoid steric effects. The corrected side-chain torsion potentials (Figure 4.2.2b, Figure A1) closely resembled the polyethylene torsion potential for $\beta_{2\text{-}5}$. To avoid confusion with the original force field, in this work we refer to this as the "modified Bhatta" force field. All other parameters are identical to those previously obtained by Bhatta and coworkers. Additionally, we will refer to these force fields using the following notation: Mod. Bhatta FF for the modified Bhatta force field, Huang FF for the force field developed by Huang and coworkers, and Moreno FF1, Moreno FF2, and Moreno FF3 for the three force fields proposed by Moreno and coworkers.

Another significant difference between these force fields comes from the atomic partial charges, especially for atoms on the thiophene ring. There is very little agreement across force fields in terms of both the magnitude and the sign of the partial charges (Figure 4.2.2d). These parameters were derived using either post-Hartree-Fock or hybrid density functional theory calculations, and each set of partial charges was derived using a different basis set. Additionally, different charge neutrality constraints were applied for the calculations. For the Moreno and Huang force fields, the charge neutrality constraint was applied for a single monomer.[28,42] For the Mod. Bhatta FF, the MP2/6-31G(d,p) post-

hartree-fock method was used with a charge neutrality constraint applied to a P3HT decamer, with the partial charges from the monomers in the middle of the chain used for the MD force field.[29] The three force fields published by Moreno and coworkers only differ in the set of atomic partial charges used. FF1 uses partial charges that are taken directly from OPLS-AA, FF2 uses partial charges derived from B3LYP/6-311G** hybrid density functional theory calculations for four different thiophene oligomers, and FF3 uses partial charges that are the average of FF1 and FF2.[28]

Another difference between the three force fields lies in the backbone torsion potentials applied to the bonds connecting adjacent monomers (α). The Bhatta potential was derived from a single point calculation on a P3HT decamer using the B3LYP/6-31+G(d,p) functional/basis set[29], whereas the same calculation was done on quaterthiophene for the Moreno potential using the B3LYP/6-311G** functional/basis set[28]. The Huang backbone torsion potential was derived through a combined MD-DFT method from which the intrinsic torsion potential was extracted.[42]

The simulation system in this work consisted of 64 chains of P3HT-RRa, with 60 monomers per chain. Simulations were also run with 16 chains to determine the effect of system size, but it was determined that this had a negligible impact on the structure and dynamics of the simulation at the time and length scales of interest (Figure A9). The simulation system was initialized in the following way. Chains were generated such that the regio-regularity of the system reflected the experimental values determined from NMR (Figure 2.3.1). A Metropolis algorithm was used to set the initial distribution of *cis* and *trans* backbone configurations to a population that would reflect the corresponding backbone torsion potentials for each force field (see Figure A4 for more details). The

chains were then placed in a large simulation box (corresponding to an initial density of 0.0671 g/cm^3), spaced sufficiently far apart to allow for a quick relaxation. The system was equilibrated by running in the NVT ensemble for 2 ns at 600 K followed by an NPT run for 4 ns at 473 K. Subsequently the simulation was cooled at a rate of 50 K/ns until target temperatures were reached. At each temperature the system was equilibrated again with an NPT run for 4 ns. After equilibration, production was in the NPT ensemble for 5 ns at the specified temperature and at a pressure of 0.001 atm, which approximated the sample conditions during QENS and WAXS experiments. These conditions were maintained using a Nose-Hoover thermostat and barostat, with characteristic time constants $\tau_{pressure}$ = 1 ps and $\tau_{temperature}$ = 0.1 ps. The velocity-Verlet algorithm was used, with a time step of 1 fs for integration of the equations of motion. For the non-bonded interactions, a cutoff distance of 10 Å was used. The long-range Coulomb interactions was calculated using particle−particle/particle−mesh (pppm) Ewald algorithm[67].

The trajectories obtained from the production runs were then used to calculate the static and dynamic structure factors using the following formulae[15]:

$$S(Q) = \sum_{i,j} Z_i Z_j \langle e^{-i\vec{Q}\vec{r}_{ij}} \rangle \quad (2)$$

$$I(Q,t) = \sum_{\alpha} \overline{\Delta b_\alpha^2} \langle e^{-i\vec{Q}\vec{r}_\alpha(0)} e^{-i\vec{Q}\vec{r}_\alpha(t)} \rangle \quad (3)$$

Equation 1 was used to calculate the static structure factor, weighted by the atomic number of each atom (Z), to allow for comparison to the results from WAXS experiments. Equation 2 was used to calculate the dynamic incoherent structure factor, and was also weighted by the incoherent neutron scattering cross sections for each atom (Δb_α^2) so as to be comparable to experimental data from QENS. Since 93% of the total QENS signal comes from incoherent contributions, we will refer to the dynamic

incoherent structure factor as I(Q, t) for the remainder of this article. The software nMoldyn was used to efficiently run these calculations.[45] For the static structure factor, 100 Q vectors were generated from 0 to 2.5 $Å^{-1}$ with a step size of 0.02 and a Q-Shell Width of 0.02 $Å^{-1}$. For the calculation of I(Q, t), 100 Q Vectors were generated from 0.3 to 1.9 $Å^{-1}$ with a step size of 0.2 $Å^{-1}$ and Q-Shell Width of 0.1 $Å^{-1}$.

Additionally, dihedral autocorrelation functions (DACFs) were calculated for the backbone (α) and the bond between the second and third carbon atoms in the side-chain (β_1) using the following formula:[68]

$$\boldsymbol{DACF(t)} = \frac{\langle \cos \boldsymbol{\phi}(t+t_0) \cos \boldsymbol{\phi}(t_0) \rangle - \langle \cos \boldsymbol{\phi}(t_0) \rangle^2}{\langle \cos \boldsymbol{\phi}(t_0) \cos \boldsymbol{\phi}(t_0) \rangle - \langle \cos \boldsymbol{\phi}(t_0) \rangle^2} \quad (4)$$

where $\phi(t)$ is the torsion angle at time t. The backbone torsion populations and inter-chain radial distribution functions for the thiophene rings were also calculated. Finally, each simulation was cooled to 13 K (at a rate of 50 K/ns), and the density of the system was sampled 200 times each at 10 K intervals. Linear fits of the density as a function of temperature both above and below the glass transition were then performed. The glass transition temperatures of the simulated systems could then be obtained by determining the point of intersection between the linear fits.

4.3 Results

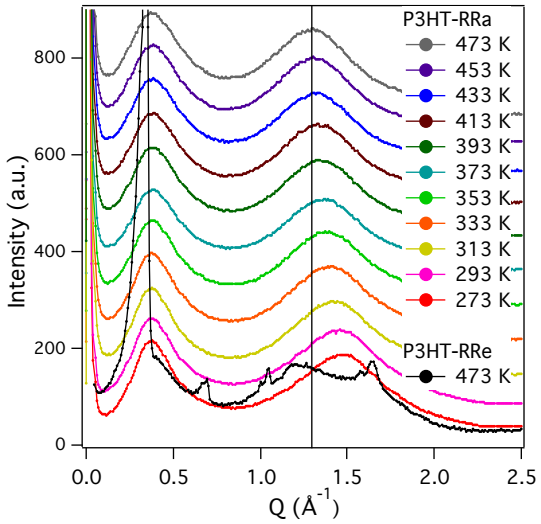

Figure 4.3.1: WAXS data for regio-random P3HT (P3HT-RRa) at temperatures ranging from 273 K to 513 K (colored symbols) and for regio-regular P3HT (P3HT-RRe) at 473 K (black). Peaks in regio-regular sample are indicative of a semi-crystalline structure with 30% crystallinity. The data from the regio-random sample is shifted for clarity. A vertical line was placed at 1.3 Å^{-1} to highlight the gradual shift that occurs in the second peak for the regio-random sample.

A regio-random P3HT polymer was chosen for this work because it maintains a single amorphous phase across all temperatures of interest. Figure 4.3.1 shows WAXS data demonstrating that there is no indication of crystallinity for the regio-random polymer over a wide temperature range, ensuring that the sample is a single-phase system. In contrast, a regio-regular P3HT sample shows a diffraction profile that is characteristic of a semi-crystalline polymer structure.[11] In order to simulate such a system, a much larger simulation would be necessary to properly capture interfaces between coexisting crystalline and amorphous domains that can range from 10 to 30 nm in size.[69,70] It would also be necessary to determine the crystalline fraction (X_c) of the system. The crystalline fraction is a measure of the relative amounts of crystalline and amorphous phases in the system. Several experimental methods for determining X_c have

been used for P3HT-RR, including DSC[57], WAXS[13], and solid-state NMR.[38] Using the method proposed by Balko and coworkers[13], X_c was determined to be ~0.3 at 473 K for our P3HT-RR sample. Furthermore, the presence of crystalline domains leads to a decreased decay in the QENS relaxations at high temperatures for $Q < 1.1$ Å^{-1} (see Figure A3). By focusing on regio-random P3HT, the experimental data can be confidently compared to numerous simulations with great accuracy and computational efficiency to identify the effect of simulation parameters.

The two broad peaks that arise in the WAXS profiles of P3HT-RRa are the result of inter-chain correlations with characteristic distances that have significant variation and fluctuate with time. The first broad low-Q diffraction peak of the P3HT-RRa sample corresponds to inter-chain correlation distances that are mediated by the lengths of the alkyl side-chains. For a crystalline P3HT sample with extended side-chains, this would correspond to the well-known lamellar spacing distance. This peak was also found to shift significantly when polythiophenes with longer side-chains were analyzed. The second high-Q peak corresponds to contributions from short ranged correlations between thiophene rings in neighboring chains. In a crystalline P3HT sample, this region would show a sharp peak corresponding to the pi-pi stacking distance between neighboring chains. Here, the peak is broad due to significant disorder and temporal fluctuations. Interestingly, a shift occurs towards lower Q values when the temperature increases. The intra-chain ring separation distance, which corresponds to a Q value of 1.6 Å^{-1}, has been previously determined from WAXS studies of crystalline P3HT, and is a fixed value independent of the temperature of the sample.[12] We therefore hypothesize that the shift

represents a gradual increase in the correlation distance between thiophene rings in neighboring chains due to significant increases in thermal fluctuations.

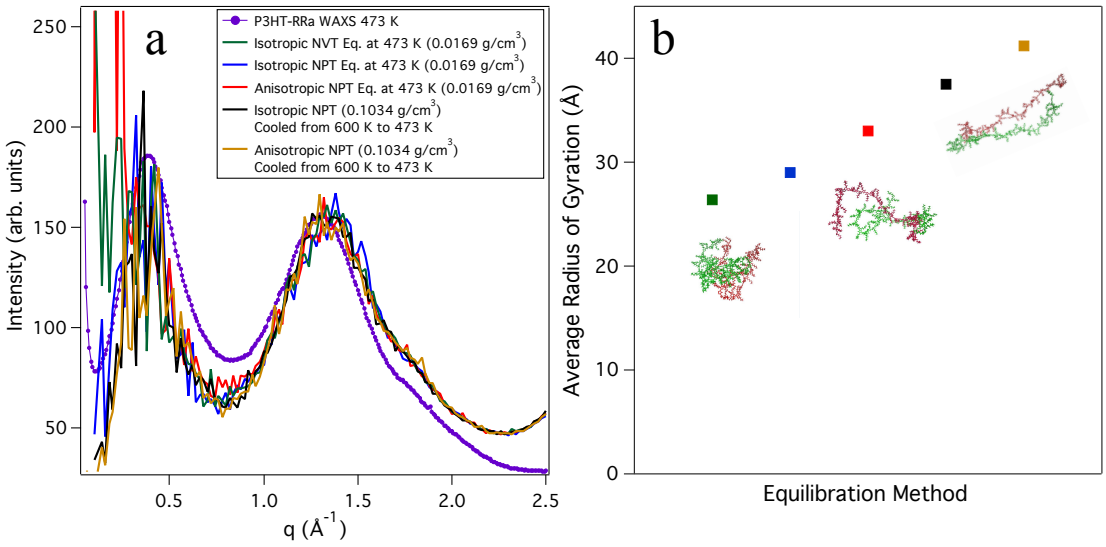

Figure 4.3.2: a) Static structure factors calculated from MD simulations of P3HT-RRa equilibrated using different ensembles. The initial packing density is shown in parentheses. In some cases, isotropy of the simulation cell is enforced, and in others, no such constraint is added, causing the equilibrated cell to become anisotropic, with the longest dimension corresponding to the direction along the chain backbones. b) The average radii of gyration for chains are plotted for each method with colors matching those in Figure 4.3.2a for identification. Images of representative chains are included for the isotropic NVT, isotropic NPT, and anisotropic NPT equilibration methods.

To properly determine the effect that different force field parameters will have on the structure and dynamics of simulations of P3HT-RRa, it was first necessary to perform a sensitivity analysis on the force field independent parameters. We first investigated the impact that different equilibration methods have on the structural characteristics of the MD simulations. The timescales for chain diffusive motions (i.e. reptation) for conjugated polymers are much longer than is accessible with these simulations due to a comb-like structure that causes large molecular friction. Therefore, it is difficult for chains in MD simulations to reconfigure and achieve an equilibrium structure within a reasonable time-frame if initial configuration is far from the real structure. As a result, it

was essential to evaluate the effects of altering the equilibration process on the structure of the system. Common equilibration strategies for polymer systems (i.e. those without pi-conjugated orbitals), often involved placing chains within a simulation cell followed by heating to temperatures well above the glass transitions to facilitate relaxation and equilibration.[71] Because the energetic barriers for configurational changes of these polymers are relatively low, the polymers have enough energy to fully explore configurational space. The cell is then slowly cooled, with sufficient time between temperature steps for the chains to fully relax, until the desired temperature is reached. Previous simulations of P3HT have adopted this method.[72] A similar method involves placing individual chains in a very large simulation cell, corresponding to densities less than 0.1 g/cm^3 and then stepping down the volume of the cell while waiting for the chains to fully relax between steps.[73] We tested combinations of both of these methods to equilibrate the P3HT-RRa simulations and investigated the impact that using different ensembles will have on the final polymer structure.

Figure 4.3.2 shows the calculated static structure factors for five systems equilibrated under different conditions with the Mod. Bhatta FF. For each case, the system was first run in a low-density NVT ensemble for 2 ns, after which the different equilibration conditions in Figure 4.3.2 were used for 4 ns, followed by an NPT production run of 5 ns. In addition to ensemble type, we investigated the effects of forcing simulation cell isotropy. We also examined the effect of starting the equilibration process at an elevated temperature (600 K) and slowly cooling the system in the NPT ensemble until the target temperature was reached. For the NVT case in which simulation cell isotropy was enforced during the production run (green curve), a low initial density

coupled with the "kinks" in the polymer chains caused the chains to fold onto themselves to form oblong clumps that were packed next to each other as the box volume is reduced. The sharp diffraction peak at low Q for this system correspond to the packing of these clumps (Figure 4.3.2a). This was also reflected in the average radius of gyration for this system, which was the lowest out of all methods used. In the NPT case where isotropy was not forced, the simulation cell became anisotropic along the direction of the polymer backbones. This caused the shortest cell dimension to approach the distances corresponding to low Q in Figure 4.3.2, which could lead to an overestimation in the pair correlations at low Q. This also explains the increase at low Q for the red curve in Figure 4.3.2a that disagrees with the experimental WAXS data. Given these observations, for all subsequent calculations, we opted to use an isotropic NPT ensemble with a moderately increased initial density (0.0671 g/cm^3) and an initial temperature of 600 K that was gradually reduced while equilibrating the system (similar to the black line in Figure 4.3.2a). Figure 4.3.2b indicates that the radius of gyration of the polymer chains is strongly dependent on the equilibration methods that are used. This is especially important for conjugated polymers because it affects the extent of conjugation of a chain and the intra-chain charge localization length.

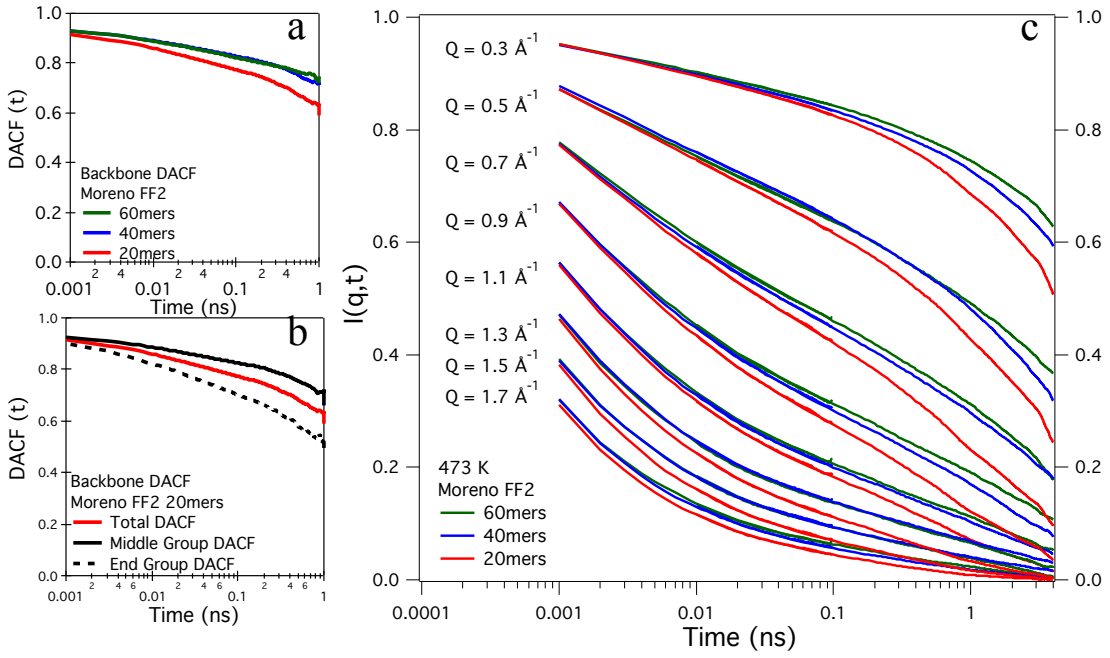

Figure 4.3.3: a) Backbone DACFs calculated for 3 MD simulations of P3HT-RRa using the Moreno FF2 force field with different molecular weights. b) For the 20-mers simulation, the overall backbone DACF, the backbone DACF for the last four monomer-monomer bonds on either ends of each chain, and the backbone DACF for the remaining monomer-monomer bonds of each chain. c) Comparisons of I(Q, t)s calculated from the same MD simulations as those shown in (a). All simulations were run at 473 K.

Having chosen an equilibration method, we then investigated the effect of molecular weight on the structure and dynamics of the MD simulations. While calculations of the static structure factors for each of these simulations revealed no significant differences (Figure A5), we expected discrepancies in the dynamics, as it is well established that the viscosity of polymer systems above the glass transition temperature is influenced by the polymer molecular weight.[74] Figure 4.3.3 shows that molecular weight indeed has a large impact on the I(Q, t) calculated from MD simulations. A clear shift is observed between the 40-mers system and the 20-mers system, while the shift observed between the 60-mers system and the 40-mers system is less pronounced. This implies a nonlinear dependence of the dynamics of the simulated system with respect to molecular weight. There is a crossover molecular weight between

20-mers and 40-mers, after which increasing molecular weight has a minimal effect on I(Q, t) over this time window. A primary contributor to the accelerated dynamics for the 20-mers system is increased backbone torsion (α) as can be seen in Figure 4.3.3 a-b. The discrepancy between DACFs for backbone torsion at the ends of each chain versus backbone torsion in the middle of the chain for the 20-mers simulation is clear. Here we define 'End Group' segments as those located four or less monomer units from a chain-end. It is clear that backbone torsional motions along α-bonds are much faster for the end group segments in the chain versus the mid-chain segments. This trend is also observed for the 60-mers and 40-mers systems (Figure A6) but the overall concentration of end groups is much lower. For 20-mers, 42% of each chain is comprised of end groups as defined in this work, which is lower when compared to high molecular weight chains where only 21% and 14% of segments correspond to end groups for 40-mers and 60-mers respectively.

After determining a suitable equilibration method and fixing the molecular weight used in our MD simulations to that of the experimental system (60-mers), we proceeded to compare all of the static structure factors, which are calculated from simulations using the five different force fields, to our experimental WAXS data. Interestingly, all five force fields showed reasonable agreement with experimental WAXS data at different temperatures (Figure A10). This indicated that using WAXS data alone as a means for validating MD simulations of amorphous P3HT was insufficient for determining which force field was best suited for simulating these systems.

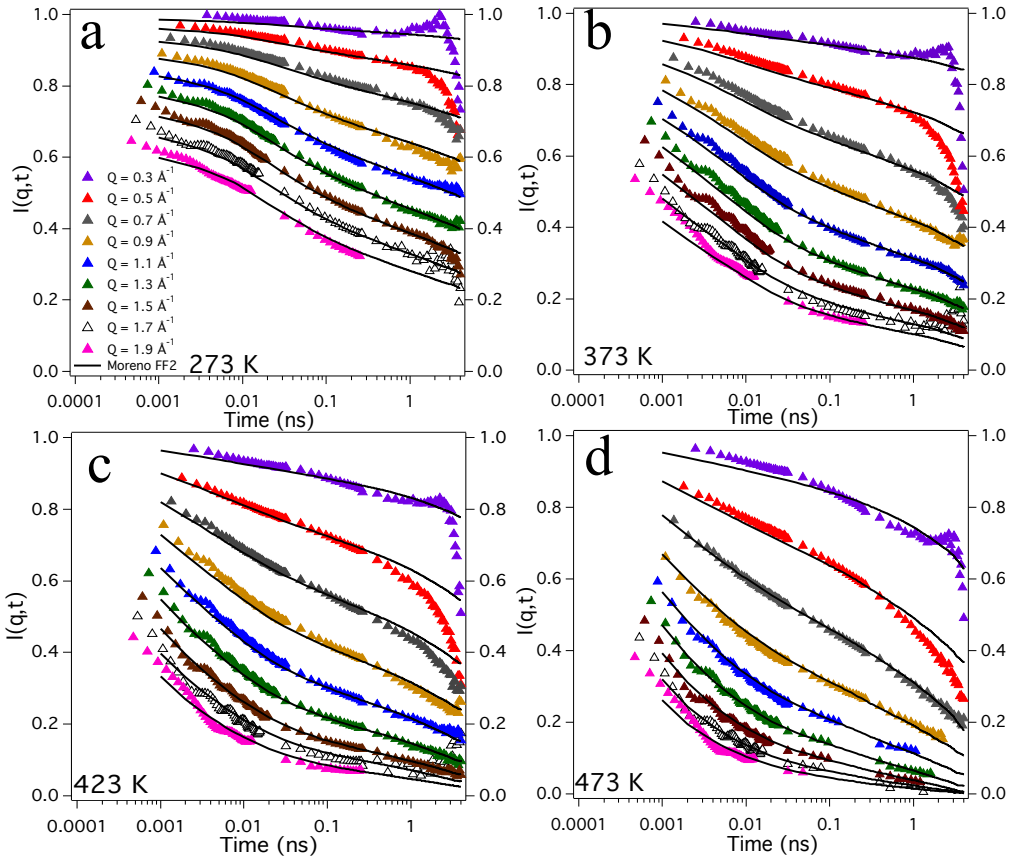

Figure 4.3.4: Comparisons of the I(Q, t)s from MD simulations of P3HT-RRa using the Moreno FF2 force field with experimental QENS data at 273 K (a), 373 K (b), 423 K (c), and 473 K (d). Experimental error bars are not shown for clarity, and are smaller than the symbols except at very long times (see figure A15).

In order to better assess the accuracy of different force fields, we compared experimental I(Q, t)s with those calculated from production trajectories of MD simulations. All of the I(Q, t)s calculated from MD simulations showed reasonable agreement when compared to experimental QENS data at high Q (Q > 1.1 Å^{-1}). Yet, clear differences between experimental and calculated I(Q, t)s were observed. Initially, we observed large discrepancies between the I(Q, t) calculated from the original Bhatta et al. force field simulation at 473 K compared to the other FFs investigated (Figure A2). This triggered the re-examination of the side-chain torsion potentials for this force field (Figure A1), and resulted in a marked improvement in the agreement between

computational and experimental data as seen by comparisons with the Mod. Bhatta FF (Figure A11). Figure 4.3.4 shows the comparison for simulations run using the Moreno FF2 force field, which is one of three force fields that show good match with experimental data over the full range of temperatures and Q values. The other two force fields that closely approximated the data were the Huang FF and Moreno FF3. Quantitative comparisons of QENS experiments to MD simulations using all the different force fields are included in Figure 6 and in the supplemental information section (Figures A11-A14). I(Q, t)s calculated from simulations using the Huang FF (Figure A14) are very similar those using Moreno FF2 indicating that this is also a very accurate force field. Still, for both of these force fields, the I(Q, t)s do not decay fast enough when compared to the experimental data at low-Q ($Q < 0.9$ Å^{-1}) and long times. Still, Huang's FF was found to have slightly weaker decays at low temperature and low-Q when compared to Moreno FF2 and to the experimental QENS data. While Moreno FF1 and Moreno FF3 show good agreement for low Q values (Figure S12-S13), they underestimate the high-Q data at high temperatures (473 K). Finally, in spite of significantly improving the original Bhatta FF with new side-chain torsion potentials, results from simulations using the Mod. Bhatta FF show the worst agreement with experimental data. These simulations fail to describe the data at low temperatures over all Q, and greatly overestimate the decay at high temperatures and low Q. These trends were further quantified by calculating average χ^2 values between the modeled and the experimental QENS data using data from all measured temperatures (Figure 4.3.5).

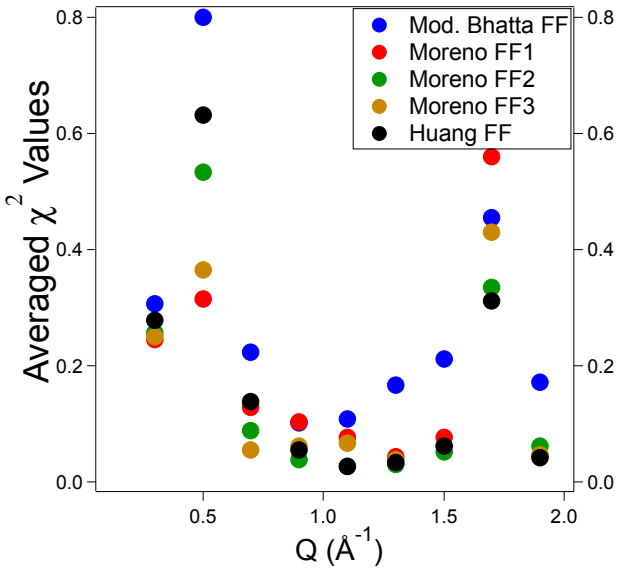

Figure 4.3.5: Average χ^2 values calculated when vertically shifting the experimental QENS data to match I(Q, t)s calculated from five MD simulations run using different force fields.

Results from MD simulations with different force fields were also compared to experimental density and glass transition temperature values (Figure 3.3.1). We identified significant discrepancies between the glass transition temperatures and densities of the simulated systems and the experimental values. The glass transition temperatures extracted from the simulations were 254 ± 15 K (Moreno FF1), 247 ± 15 K (Moreno FF2), 252 ± 15 K (Moreno FF3), 283 ± 15 K (Mod. Bhatta FF), and 319 ± 15 K (Huang FF). Interestingly, although the Mod. Bhatta FF shows the poorest agreement with the experimental QENS data, the glass transition temperature for this system has the closes agreement with the experimental value of 277.4 K (Figure A8) as obtained from DSC measurements. Moreover, all of the simulations also underestimate the experimental density by 4.0 to 7.2 % (Figure 3.3.1). Here, the Huang FF is found to come closest to approximating experimental density values obtained from neutral buoyancy. Guilbert and coworkers have also reported an underestimation of the experimental density from simulations of amorphous regio-regular P3HT, and have ascribed the difference to the

presence of crystalline domains in the experimental system.[25] We have shown here that this discrepancy exists even for purely amorphous systems.

From these results, we can determine that the most significant differences in the force field parameters come from the backbone torsion potential, the partial charges, and the torsion potential of the first bond to the side-chain. All other parameters are very similar or identical between all of the evaluated force fields. Given that the Mod. Bhatta FF showed the poorest agreement with the QENS data, we investigated the effect of changing these three parameters for this force field to see if it is possible to improve the agreement of the dynamics in the simulation system with those of the experimental QENS data.

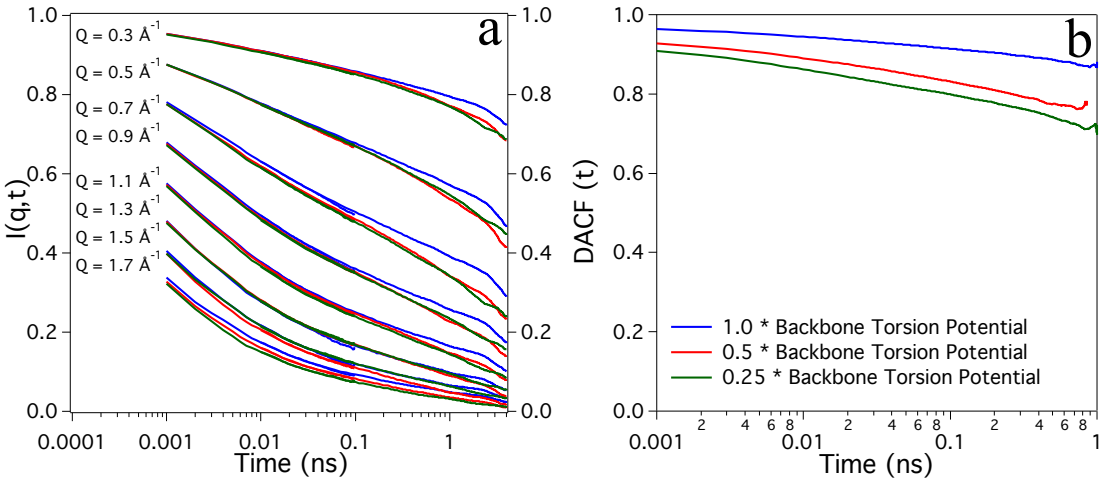

Figure 4.3.6: a) I(Q, t)s calculated for three MD simulations run using the Mod. Bhatta FF with the backbone (α in Figure 4.2.2) torsion potential unscaled, scaled by a factor of 0.5, or scaled by a factor of 0.25. b) Dihedral autocorrelation functions of the backbone for the same MD simulations.

We first investigated the effect of reducing backbone torsion potentials corresponding to the bonds connecting adjacent monomers (α). This potential is applied in MD simulations of P3HT to account for the increased rigidity and planarity of the thiophene rings which is a result of pi-orbital conjugation. This parameter is extremely

relevant because torsional motions of the backbone will affect the degree to which pi-orbital overlap occurs for both intra-chain and inter-chain charge hopping events.[37,75] Both the Moreno and Bhatta backbone torsion potentials have similar features, but differ in both the height of the torsion potential barrier and in the energy difference between states corresponding to *cis* and *trans* dihedral angles. The potential used by Huang has the highest torsion potential and has a much steeper slope compared to the other two force fields. Interestingly, previous *ab initio* calculations have also shown that the height of the backbone torsion potential increases with increasing conjugation length.[76] This is also evident when comparing the Bhatta and Moreno backbone torsion potentials, which were each, obtained from *ab initio* calculations on a decamer and a tetramer, respectively. Two new MD simulations were thus run using the Mod. Bhatta FF in which the backbone torsion potential was scaled by factors of 0.5 and 0.25 (Figure A17). Figure 4.3.6 shows the effect that the backbone torsion potential scaling had on the relaxation dynamics of the simulated system. A modest downward shift in I(Q, t) is observed at low-Q for the simulations with scaled torsion potentials relative to that with the original Mod. Bhatta FF. A similar shift is also observed in the backbone DACF, indicating that these are the modified fluctuations. Further scaling the backbone torsion potential by a factor of 0.25 does not cause a further shift in either the I(Q, t) or the backbone DACF.

Given that the magnitude of the partial charges in the Mod. Bhatta FF were also an order of magnitude higher than those in the Moreno force fields, we also investigated the effect of scaling down these parameters. We observed that the overall side-chain dynamics of the simulated P3HT system were greatly accelerated as the magnitudes of the partial charges in the backbone are scaled down (Figure A16). Lastly, motivated by a

similar rationale, we also probed the effect of removing the torsion potential that is applied to the bond linking the side-chain to the thiophene ring (β_1). This potential is very different between the Moreno and Bhatta FF's and it is not applied at all in the Huang FF (Figure 4.2.2b). We found that this parameter did not significantly affect the observed dynamics to the same extent that the partial charges and the backbone torsion potential did (Figure A18). Yet, it is also clear that a torsion potential should be in place for this bond in order for the force fields to be physically meaningful.

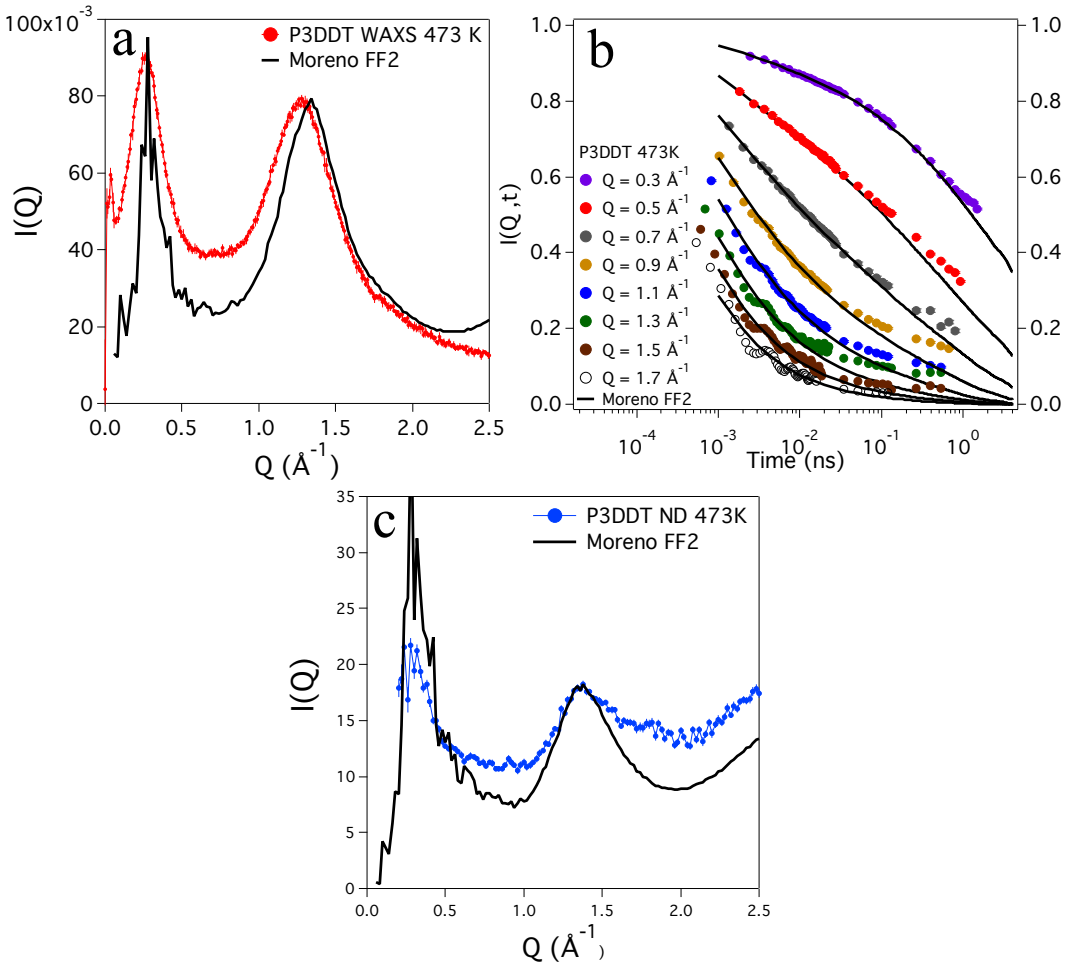

Figure **4.3.7**: a) Comparisons of the X-Ray static structure factor calculated from an MD simulation of amorphous P3DDT using the Moreno FF2 force field with experimental WAXS data at 473 K. b) Comparison of the calculated I(Q, t)s from the same simulation with experimental QENS data. c) Comparisons of the static coherent structure factor calculated from the same simulation with experimental ND data.

Having determined that the Moreno FF2 force field provided the best agreement with experimental data and was based on physically meaningful parameters, we investigated the applicability of the force field to a different poly(3-alkylthiophene), regio-regular P3DDT. P3DDT has a similar structure to P3HT but has twelve carbons in the side-chain instead of six, making it fully amorphous at relatively low temperatures. The same equilibration procedure was used to prepare the simulations, and the static and dynamic structure factors were calculated for comparison with WAXS and QENS experimental data using identical methods. Figure 4.3.7 shows that the simulation run using the Moreno FF2 force field accurately represents the structure and dynamics of P3DDT in the bulk melt phase at 473 K for the time scale less than 0.1 ns. Unlike the P3HT comparisons, for which the simulations overestimate the decays at long times only for low Q values, the experimental I(q, t)s are underestimated for all Q values at longer time scale. In addition, there are slight disagreements in the broadness and in the position of the second peak in the X-Ray static structure factors between the MD simulation and the experiment. Contributions to the second peak come from both inter-chain and intra-chain thiophene ring correlations. We hypothesize that the disagreement in the second peak comes from inter-chain ring-ring distances that are shorter in the simulated system when compared to the experimental sample. However, this shift to lower Q corresponds to a small difference in real distance equal to ~0.01 Å. Moreover, this discrepancy does not appear when comparing the simulation to the second peak of the neutron diffraction data (Figure 4.3.7c).

4.4 Discussion

Since MD simulations are increasingly used as the foundation for *ab initio* calculations to evaluate the electronic properties of conjugated polymers, it is necessary to assess the accuracy of force fields used in MD simulations using a variety of experimental methods to validate them. Our results show that there are still discrepancies between the experimental data and observables calculated from simulations when using different force field parameters. Moreover, certain force fields show better agreement with experiments depending on the specific benchmark that is being used to assess them. For example, the statistical analysis in Figure 4.3.5 points to Moreno FF2, Moreno FF3, and Huang FF as being equally suitable for use in MD simulations. However, out of these two force fields, Figure 3.3.1 shows that the Moreno force fields better approximate the experimental glass transition temperature while the mass density of the Huang FF simulation comes closest to the experimental density. In addition to experimental validation, it is also necessary to investigate the physical basis that is used to develop the force field parameters. When applying this additional scrutiny to the best performing force fields in Figure 4.3.5, it is clear that only Moreno FF2 can be recommended for future simulations of polythiophenes in order to accurately capture their dynamics. The Huang FF does not include any torsion potential for the bond linking the side-chain to the thiophene ring (i.e. this is a freely rotating bond), which is not physically accurate. Moreno FF3 and Moreno FF2 only differ in their atomic partial charges. While the partial charges in Moreno FF2 were derived from well-grounded *ab initio* calculations, the Moreno FF3 partial charges were determined by taking the arithmetic mean of the

Moreno FF2 partial charges with those of the classical OPLS FF (i.e. Moreno FF1). Ultimately, this is not a physically meaningful method to determine partial charges.

Given that Moreno FF2 shows the best overall agreement when considering the above criteria, we must acknowledge its greatest shortcoming when used to simulate amorphous P3HT: the disagreement with the experimental QENS data at low Q values. To further explore this issue, we turn to Figure 4.3.3 and note that all comparisons between simulations and QENS data have been run using monodisperse chains in the simulations. Figures 4.3.3b and 4.3.3c show that the increased torsion of the backbone as well as the smaller size of the 20-mers are both conducive to faster segmental and translational motions, which are responsible for the faster decay of I(Q, t) at low Q ($Q < 1.3$ $Å^{-1}$). Additionally, in polydisperse polymer systems above the glass transition, it has been shown that low molecular weight chains can act as plasticizers, increasing the self-diffusivity of longer chains.[55] We hypothesize that accounting for polydispersity in the simulation would likely increase the decay of the calculated I(Q, t)s at low-Q, while the high-Q I(Q, t)s will remain relatively unchanged since this region is dominated by localized side-chain motions. However, this hypothesis does not address the discrepancy regarding the P3DDT QENS data, seen in Figure 4.3.7b. The fact that the Moreno FF2 simulation now seems to underestimate the data for all Q values is surprising, especially when considering that no extra *ab initio* parameterization should be necessary for the P3DDT polymer. The only change comes from the addition of six more carbons in the side-chain, but as seen in Figure A1, the torsion potentials for the side-chain carbons converge to the polyethylene torsion potential as the distance to the thiophene backbone increases. This puzzling limitation of the Moreno FF2 force field necessitates an in depth

look at force field transferability for different conjugated polymer systems, which is beyond the scope of this work.

Overall, in order to achieve high experimental accuracy when simulating amorphous P3HT, we recommend using the Moreno FF2 force field, simulating an accurate molecular weight (accounting for polydispersity if possible), and using an equilibration method that approximates the real chain conformation in the solid state, which could be probed with contrast variation SANS experiments. Moreover, we can also qualitatively assess the extent to which the observed fluctuations in MD simulations could affect the results of an *ab initio* modeling of electronic properties in conjugated polymers.[46]

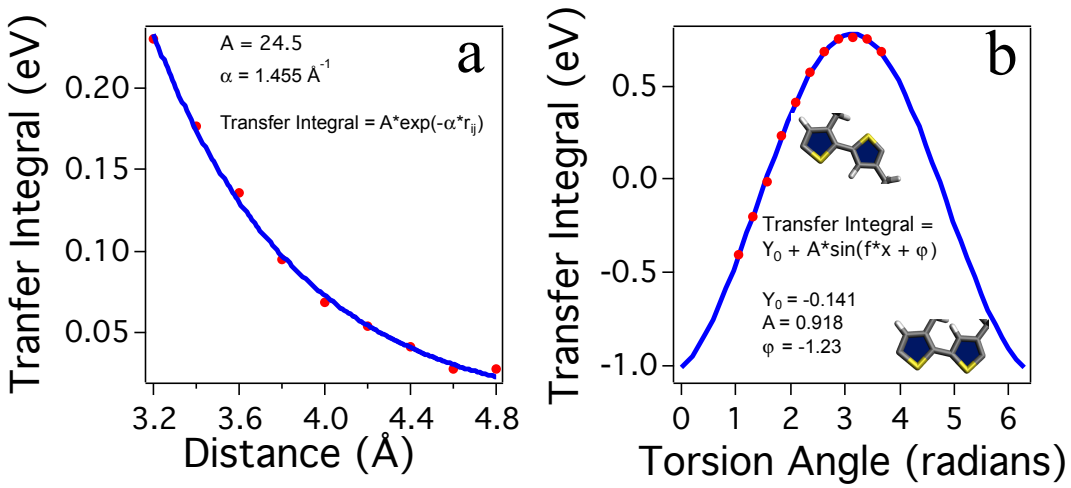

Figure 4.4.1: a) Plot of the transfer integral versus distance for electronic coupling between P3HT monomers on neighboring chains. b) Plot of the transfer integral versus torsion angle for electronic coupling between neighboring P3HT monomers on the same chain. The data points are taken from DFT calculations run in a previous study by Lan and coworkers[50].

The Marcus rate is a general expression commonly used to analytically describe charge transport in conjugated polymers using a hopping model that is temperature-dependent. The equation is as follows:[49]

$$k_{A\rightarrow B} = \frac{2\pi}{\hbar}\frac{|J_{AB}|^2}{\sqrt{4\pi\lambda kT}}\exp\left[-\frac{(\Delta U_{AB}-\lambda)^2}{4\lambda kT}\right] \quad (5)$$

where $k_{A\rightarrow B}$ is the rate for a charge hopping from site A to site B, ħ is Planck's constant, and k is Boltzmann's constant. λ is the configurational reorganization energy, which is a measure of how much the geometry of the charge transfer complex changes as charge is transferred from site A to B. ΔU_{AB} is the total driving force for the charge to hop from site A to site B. J_{AB} refers to the electronic coupling between the two sites, and is represented by the transfer integral. While most of these parameters can only be evaluated for P3HT by means of computationally expensive *ab initio* calculations, the dependence of the charge transfer integral on the relative positions of the conjugated rings is well established.[75] Figure 4.4.1 shows values of the charge transfer integral calculated using quantum mechanical methods for both inter-chain and intra-chain charge hopping in P3HT along with fits.[75] It is evident that the magnitude and sign of the transfer integral for intra-chain charge transport (Figure 4.4.1b) are highly dependent on the backbone torsion angle (α). Similarly, the strength of the inter-chain transfer integral exponentially decays as the distance between adjacent thiophene rings increases. It is therefore possible to qualitatively assess how charge transport properties calculated from snapshots of bulk MD simulations of P3HT could be affected by the choice of force field in a particular MD simulation.

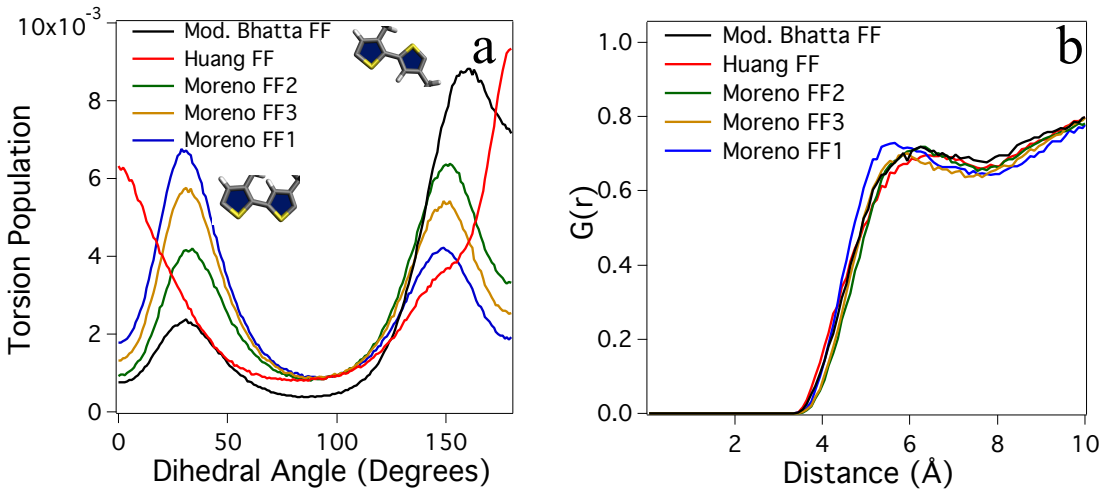

Figure 4.4.2: a) Normalized backbone torsion populations for MD simulations of P3HT-RRa using five different MD force fields. A dihedral angle of 0° corresponds to a *cis* backbone configuration while 180° corresponds to a *trans* configuration. b) Inter-chain ring-ring radial distribution functions calculated from the same MD simulations.

Despite the apparent similarities in the static structure factors calculated for simulations run using different force field parameters, Figure 4.4.2 demonstrates that the simulations show significant differences in the distribution of backbone torsion angles (α) and in the inter-chain radial distribution function of the thiophene rings. The peaks of the distribution of P3HT backbone configurations in the Huang FF simulation are centered at 0° and 180°, which respectively correspond to *cis* and *trans* backbone configurations. This implies a higher coplanarity between thiophene rings when compared to the Mod. Bhatta FF and Moreno FFs, for which the peaks are shifted to 30° and 150°. Differences in the exact location of the *cis* and *trans* peaks in Figure 4.4.2a stem from the differences in the shape of the backbone torsion potential for each force field (Figure 4.2.2). For the Moreno and modified Bhatta backbone torsion potentials, the regions corresponding to *cis* and *trans* configurations have a relatively flat potential profile, allowing for a wider range of accessible torsion angles without any energetic penalty from the torsion potential. In contrast, the backbone torsion potential used in Huang FF is steeper than the

other two with fewer flat regions that cause the distribution of torsion angles to *cis* and *trans* configurations at 0˚ and 180˚ respectively. Both the normalized torsion population and the inter-chain ring-ring radial distribution function are extremely important parameters, as they play a significant role in determining the charge transport properties for the simulated system.[49,75]

Additionally, we also found that the choice over partial charges can also influence the relative number of *cis* and *trans* configurations for the backbone. Figure 4.4.2 shows the distribution of backbone dihedral angles for MD simulations run using the three Moreno force fields, for which the only differences come from the atomic partial charges since the backbone torsion potential is identical. Although each simulation was initialized with identical backbone dihedral angle distributions, after equilibration, either *cis* or *trans* configurations are more abundant depending on the set of partial charges that is used.

These observations are of particular importance when using combined MD simulations and *ab-initio* methods to calculate parameters related to charge transport. For example, the value of the charge transfer integral for intra-chain charge hopping is positive for a *trans* backbone configuration, which indicates a bonding molecular orbital is formed between the hopping sites.[75] The same parameter for a *cis* backbone configuration is negative, indicating an anti-bonding molecular orbital, which requires more energy to be filled than its bonding counterpart. This has also been shown in a recent study of oligothiophenes, which suggested that the presence of *cis* conformations caused asymmetry in the density of states for the lowest unoccupied molecular orbitals of the molecule.[77] Furthermore, both the distribution of positive and negative atomic partial charges on the thiophene ring as well as their magnitudes will impact the inter-chain ring-

ring separation distance, which also affects inter-chain charge transport.[75] This is evident when looking at the ring-ring radial distributions for the three Moreno force fields in Figure 4.4.2. Figure 4.4.3 demonstrates that chains in simulations using the Moreno force fields show increased torsional motions of the thiophene backbone units when compared to identical simulations using the Mod. Bhatta FF and Huang FF. Additionally, there is a large discrepancy in the time evolution of the mean squared relative displacement (MSRD) of the thiophene rings on a given chain relative to their closest neighbouring rings on other chains (i.e. the conjugated rings that are amenable to inter-chain charge transport). Therefore, the timescales for both intra-chain and inter-chain electronic coupling and the time dependence of charge transport events for these systems are also anticipated to be significantly different depending on the force field used in the simulation.

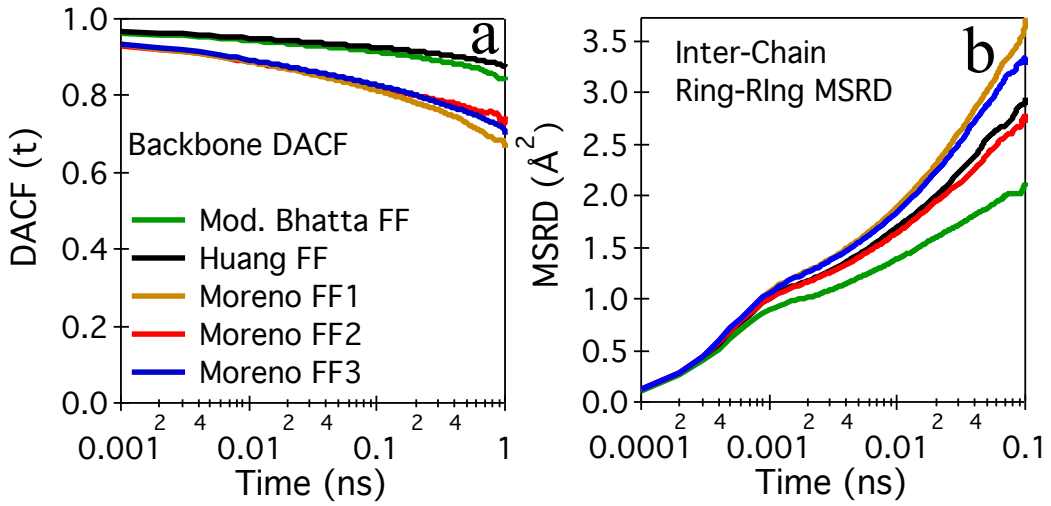

Figure 4.4.3: a) Backbone dihedral autocorrelation functions for MD simulations run using five different force fields. b) Inter-chain ring-ring mean squared displacement for the same simulations.

When examining Figures 4.4.2 and 4.4.3 through the Marcus theory lens, it is immediately clear that different force field parameters (particularly those parameterized from *ab initio* methods) will affect the accuracy of an *ab initio* calculation made from a

snapshot of an MD simulation. For example, Figure 4.4.1 suggests that the Mod. Bhatta FF would represent a system with facilitated intra-chain charge transport when compared to Moreno FF1 because more *trans* backbone configurations would be present. The reverse would be true when considering inter-chain charge transport because the probability of "seeing" a ring from another chain within the range required for inter-chain charge hopping is greater for Moreno FF1 (Figure 4.4.2b). This points to the need for more rigorous scrutiny when calculating force field parameters using *ab initio* methods.

We have also gained insight as to the limitations of experimental methods that lack of sensitivity to key parameters that could only be probed *in silico*. For example, none of the x-ray or neutron scattering data was determined to be sensitive to differences in the torsion populations and radial distribution functions as observed in Figure 4.4.2. Neutron diffraction with selective deuteration and/or solid state NMR measurements may provide the means to more accurately validate the torsion populations that are observed in simulations as shown in Figure 4.4.2a. Furthermore, comparison of experimental QENS data to simulated I(Q, t)s was not sufficient, on its own, to select the optimum force field from Moreno FF2, Moreno FF3, and Huang FF. This problem could be solved by utilizing instruments with improved energy resolution (i.e. Neutron Spin Echo spectrometers) since more significant differences between simulations with variable force fields and experimental data could become apparent at longer length scales and time scales. This work also suggests the need to develop accurate, high-throughput methods for force field parameterization with validation in order to enable *in-silico* design of novel materials. The bottleneck in this work is the exploration of the simulation parameter space with a large number of MD simulations with high uncertainty.

Streamlining this process may allow for efficient *in silico* materials design that informs chemical synthesis.

4.5 Conclusions

In this work, we have extensively explored the different parameters involved in running MD simulations of conjugated polymers. We found that crystallinity, molecular weight, and equilibration procedures are key parameters that will affect the structure and dynamics of the simulation regardless of which force field is used. Molecular weight strongly impacts the I(Q, t)s calculated from these simulations, and it is necessary to implement an accurate molecular weight distribution when comparing simulation results to experimental QENS data. We also found that Moreno FF2, Moreno FF3, and Huang FF show the best match when compared to the dynamics of P3HT-RRa. Of these three force fields, the Moreno force fields better approximated the glass transition temperature of P3HT-RRa, whereas the Huang FF came closest to matching the experimental density. However, by examining the methods used for parameterizing these force fields, we concluded that Moreno FF2 should be used for subsequent MD simulations of polythiophenes. Still, even with the Moreno FF2 force field, there are discrepancies at low-Q values when comparing to experimental QENS data. We hypothesize that the disagreement at low-Q could be resolved by taking into account the polydispersity of the chains. We also show that both the magnitude and the sign of the atomic partial charges play a significant role in determining the dynamics and the structure of the system. By comparing the three Moreno force fields, we saw that the sign of the partial charges will affect both the relative number of *cis* and *trans* backbone configurations and the average inter-chain ring-ring separation distances. Both of these parameters are crucial for

determining charge transport properties since they both affect the charge transfer integral and charge-hopping rates in conjugated polymers according to Marcus theory. Our results also suggest that proper care must be taken when running quantum mechanical calculations to parameterize MD force fields of conjugated polymers. For example, using a hybrid density functional theory approach and enforcing charge neutrality over a single monomer of P3HT (Moreno) versus using a post-Hartree-Fock approach and only enforcing charge neutrality over a whole decamer (Bhatta) results in widely different values for the atomic partial charges. Finally, we demonstrated that the Moreno FF2 force field is also applicable to other amorphous P3ATs by comparing the static and dynamic structure factors for an MD simulation of P3DDT to experimental QENS and WAXS data of the same system.

Chapter 5: Future Work

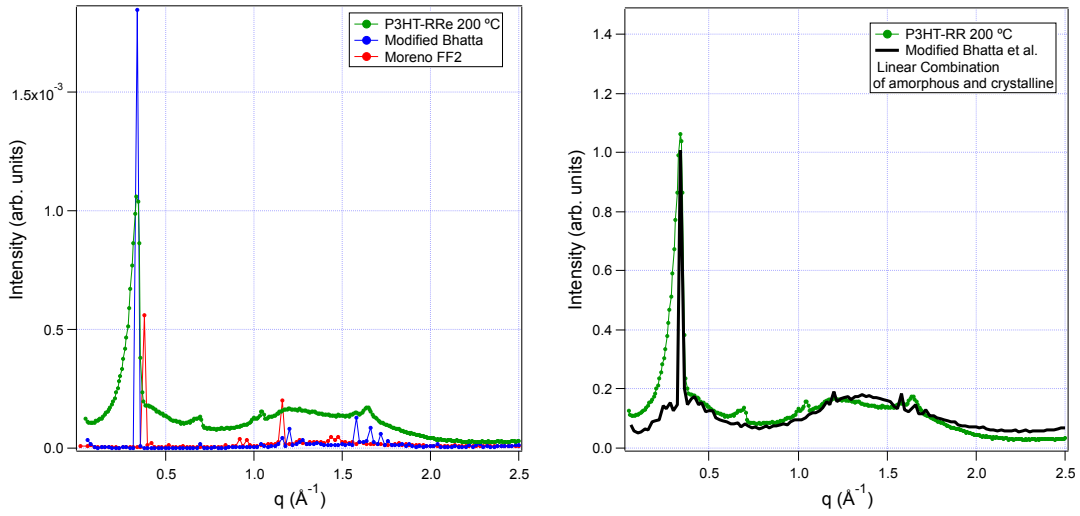

Figure 5.1: Left: Comparisons of the X-ray static structure factors calculated from MD simulations of crystalline regio-regular P3HT run using the Mod. Bhatta FF and Moreno FF2. Right: A linear combination of the static structure factors calculated from MD simulations of fully amorphous and fully crystalline P3HT.

In the short term, we recommend extending the approach used in this work to semi-crystalline systems. Figure 5.1 shows comparisons between the static structure factors calculated from MD simulations of fully crystalline regio-regular P3HT and the corresponding WAXS data. Unsurprisingly, the Mod. Bhatta FF shows better agreement with the experimental data compared to Moreno FF2. This is because the partial charges applied to the backbone when using the Mod. Bhatta FF are an order of magnitude greater than those applied when using Moreno FF2, promoting stronger electrostatic attractions between thiophene rings which corresponds to a stronger pi-stacking interaction. Figure 5.1 (right) also shows a linear combination of amorphous and crystalline P3HT simulations compared to the same experimental WAXS profile. The force field used was the Mod. Bhatta FF, and the amorphous simulation was regio-

random instead of regio-regular, so the comparison is not ideal. Despite this, the strong agreement between the linear combination and the experimental data suggests that this method could be used to validate simulations of conjugated polymers with semicrystalline phases by properly weighing a fully crystalline simulation with a fully amorphous simulation of identical systems. Unfortunately, simulations that include amorphous and crystalline domains require much larger systems and computational resources.

A key challenge in performing accurate MD simulations of conjugated polymers is to account for electron delocalization. Force fields parameterized for conjugated polymers have assumed an electron density that either corresponds to pi-stacking or to delocalization along single chains. It is exceedingly difficult to account for all possible combinations of these cases using traditional force fields. Implementing polarizable force fields could provide a solution to this problem[78]. They could allow the atomic partial charges of the backbone to fluctuate so as to facilitate pi-stacking only when certain criteria are met (i.e. another thiophene ring is within some cutoff and has a suitable orientation). However, this would also require increased computation time.

In the long term we hope to automate the parameterization of the an MD force field given certain experimental inputs such as QENS and WAXS data, density, glass transition, etc. It may be possible to train a neural network machine-learning algorithm to optimize the force field so as to get maximum agreement with the experimental inputs[79]. However, given the large size of the parameter space, a significantly larger training data set would be required.

Chapter 6: Summary

This work presents a set of experimental techniques that can be used to validate MD simulations of bulk conjugated polymer systems and systematically investigates the relevant simulation parameters. QENS data provides a powerful method for validating the dynamics of an MD simulation. WAXS data alone is insufficient for validating the thermodynamic properties, and supplementing this with DSC and density measurements is necessary. The atomic partial charges derived from *ab initio* calculations are the simulation parameters with the greatest uncertainty, and they also have the greatest effect on the dynamics and configurations (i.e. *cis* and *trans* populations) of the polymer chains. By using this work as a foundation for studies of more complex conjugated polymer systems, a greater understanding of the relationship between polymer chemistry and performance will be obtained.

Appendix

Force Field Parameters

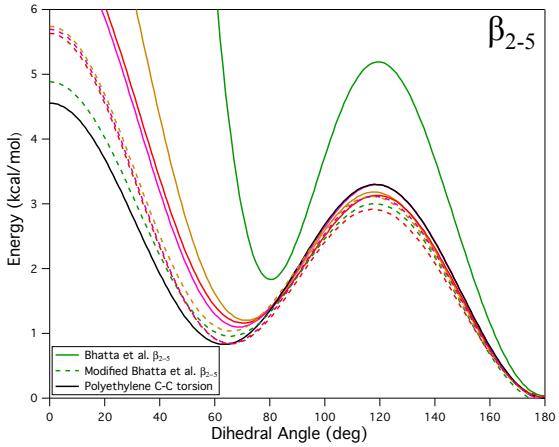

Figure A1: Torsion potentials for the side-chain carbon-carbon bonds ($\beta_{2\text{-}5}$ in Figure 4.2.2) for Bhatta FF (solid colored lines) and Mod. Bhatta FF (dotted colored lines) as well as the torsion potential for polyethylene from the base OPLS-AA force field (black), which was used for the Moreno FFs and Huang FF.

QENS Comparison using Bhatta et al. Force Field

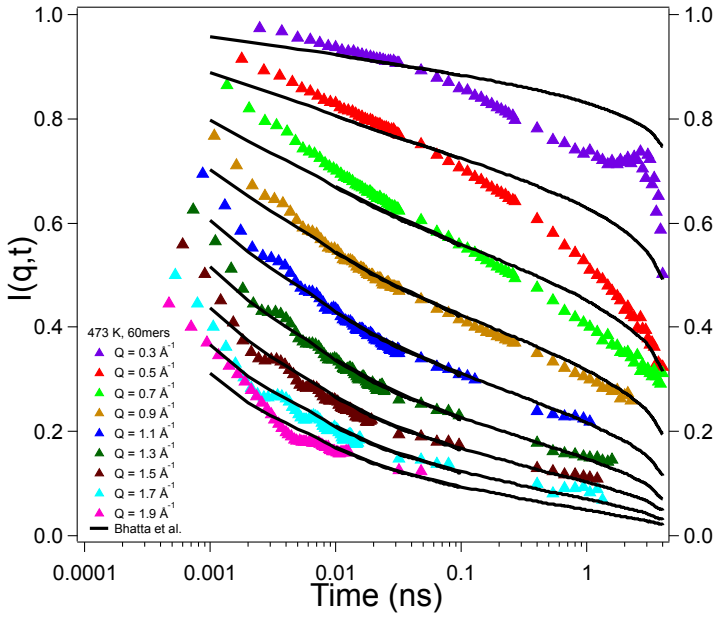

Figure A2: Comparison of the DISF calculated from MD simulations of P3HT-RRa run using the Bhatta et al. force field with QENS data of P3HT-RRa.

Comparison of QENS Data for Regio-regular and Regio-random P3HT

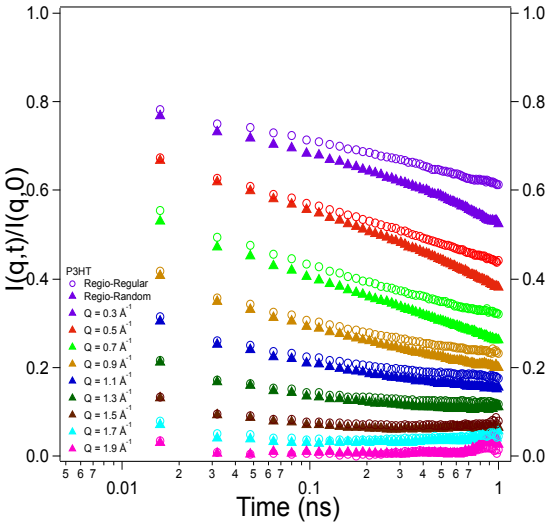

Figure A3: Comparisons of QENS data from BASIS for regio-regular and regio-random P3HT at 473 K.

The presence of crystalline domains causes a decreased decay in the dynamic structure factor at high temperatures for $Q < 1.1$ Å^{-1}. This indicates that segmental dynamics in the crystalline phase take longer to decorrelate, either due to slower segmental motions or greater confinement of the side-chains in the crystalline domains. The fact that the decays of the intermediate scattering functions are the same for higher Q suggests that there is enough free volume for motions localized to a single side-chain to occur irrespective of polymer phase.

Monte Carlo Algorithm used to Initialize Torsion Populations

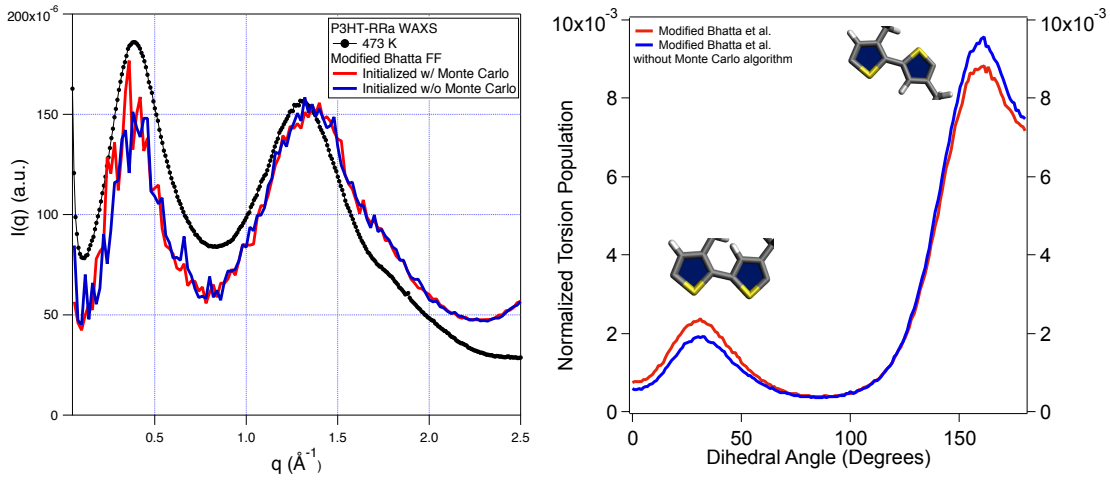

Figure A4: Left: Comparisons of the static structure factor calculated from MD simulations run using the Mod. Bhatta FF to WAXS data of P3HT-RRa. One simulation (red) was initialized using a Monte Carlo algorithm to determine its initial backbone torsion angle distribution, and the other (blue) was initialized with a completely *trans* distribution. Right: The normalized torsion populations for each simulation.

A key factor to take into account when equilibrating these systems is the relative population of *cis* and *trans* conformations of the backbone. The high energetic barriers for backbone torsion necessitate an exceedingly long equilibration period to accurately reflect a system with torsion populations suggested by the backbone torsion potential calculated from DFT. This means that, starting from an all *trans* configuration, a standard equilibration method will provide a backbone torsion population that is inaccurately biased towards *trans* configurations. In order to solve this issue, we implemented a Monte Carlo algorithm with a Metropolis criterion to set the initial distribution of backbone dihedral angles as indicated by the backbone torsion potentials of each force field. Figure A4 shows the effect that implementing this algorithm had on the structure and final torsion population of MD simulations run using the Mod. Bhatta FF. While there is no clear change in the calculated structure factors, the backbone torsion

population shows a clear increase in the number of *cis* configurations. It is important to note that even when equilibrating at high temperature and low initial density, the polymer chains were still biased towards adopting more *trans* configurations. The problem would likely be more exacerbated if the system was initialized with a higher initial density or a crystalline configuration. In this scenario, increased sterics would further prevent *trans* to *cis* flips from occurring, causing differences more dramatic than those seen in Figure A4. This is particularly significant when running combined MD-DFT experiments, as both orbital structure and conjugation length are affected by introducing *cis* conformations to a chain[47].

Effect of Chain Length on the Static Structure Factor

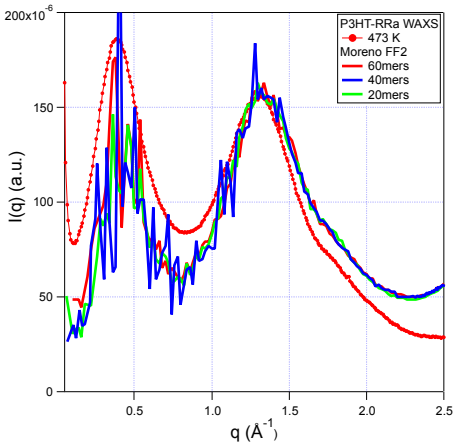

Figure A5: Comparisons of the static structure factor calculated from three MD simulations with different chain lengths to WAXS data of P3HT-RRa. The simulations were run using the Moreno FF2 force field.

Backbone Dihedral Autocorrelation Functions for 60-mers and 40-mers Moreno FF2 Simulations

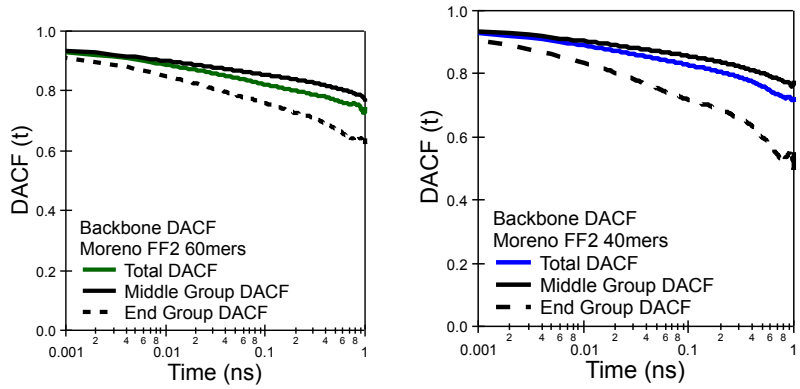

Figure A6: Middle group versus End group contributions to the backbone DACF for simulations consisting of 60-mers and 40-mers run using the Moreno FF2 force field.

Side Chain Dihedral Autocorrelation Functions for Moreno FF2 Simulations with Different Molecular Weights

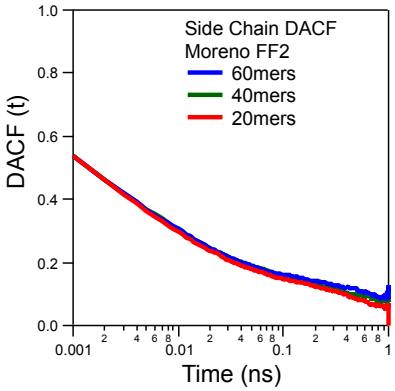

Figure A7: Side-chain DACFs calculated for 3 MD simulations of P3HT-RRa using the Moreno FF2 force field with different molecular weights.

Differential Scanning Calorimetry (DSC) of P3HT-RRa

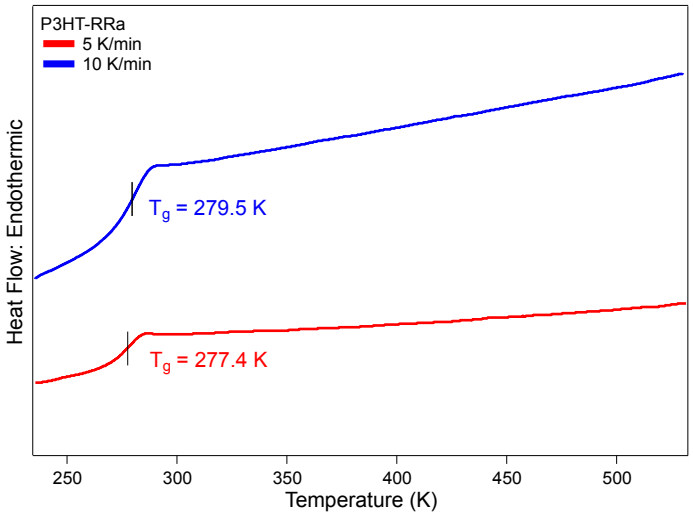

Figure A8: DSC thermograms were taken at heating rates of 10 K/min and 5 K/min, and were used to determine the glass transition temperature of regiorandom P3HT.

Effect of Simulation Size

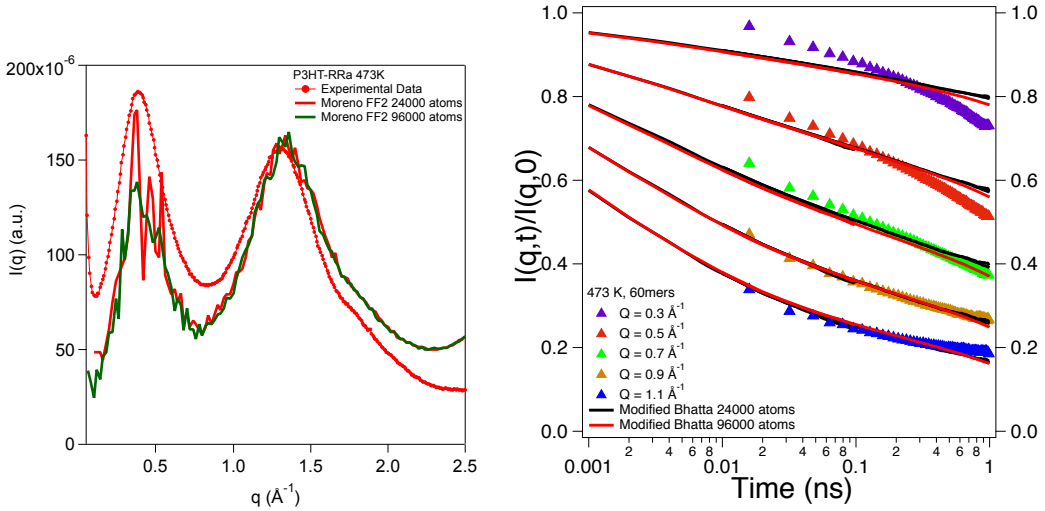

Figure A9: Left: Comparison of the static structure factors calculated from two MD simulations of P3HT-RRa using the Mod. Bhatta FF with system size of 24000 atoms and 96000 atoms. Right: Comparison of the dynamic structure factors calculated from the same MD simulations.

The result of quadrupling the system size from 24000 atoms to 96000 atoms is better statistics for the first peak with fewer fluctuations in the intensity for Q < 1.0 Å^{-1}. No significant differences in the dynamic structure factor are observed.

Structure Factors from MD Simulations with Different Force Fields

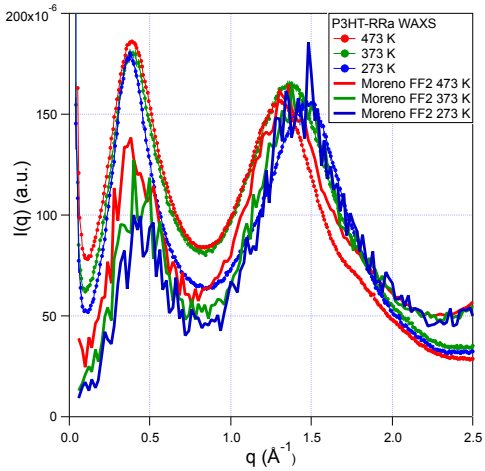

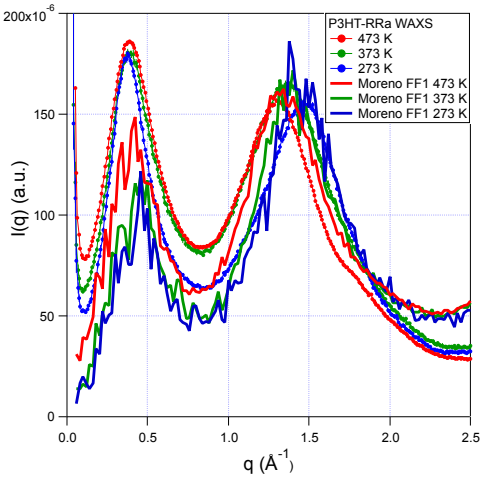

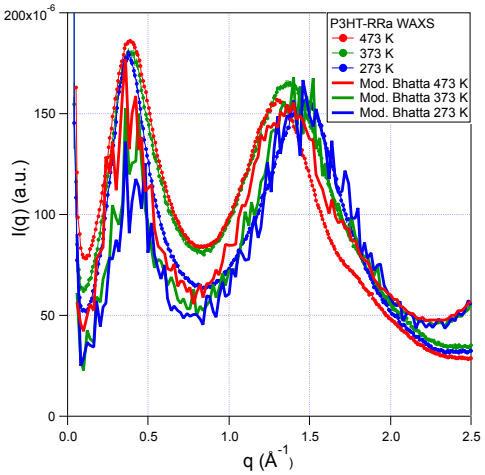

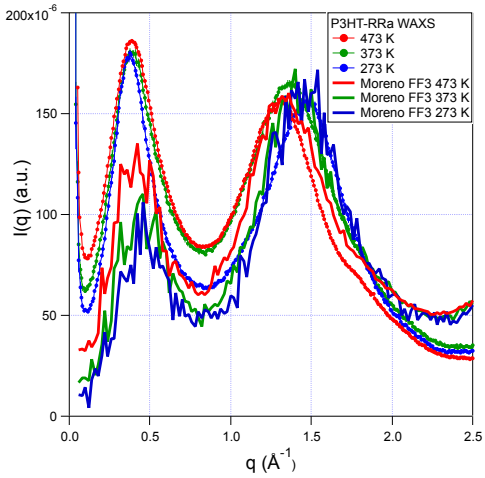

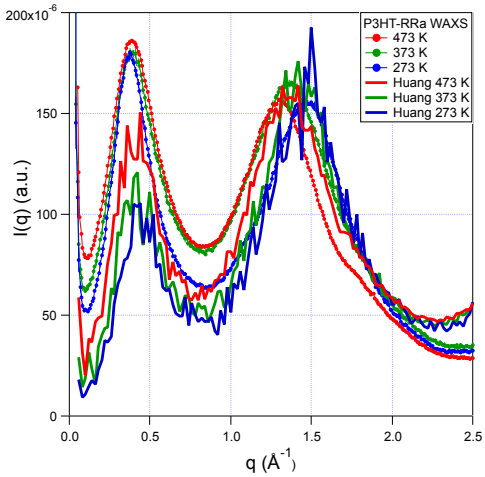

Figure A10: Comparisons of the static structure factors calculated from MD simulations of P3HT-RRa at 473 K, 373 K, and 273 K using different force field parameters with the corresponding experimental WAXS profiles.

For all of the static structure factors calculated, the height of the first peak, which corresponds to inter-chain separation distances increases with increasing temperature. Furthermore, the height of the first peak calculated from simulations is always underestimated compared to the height of the experimental peak. This likely indicates that the total system size of the simulation is not large enough to allow for a higher number of inter-chain correlations that have length scales corresponding to the Q range of the first peak.

QENS Comparison with MD Simulations using Different Force Fields

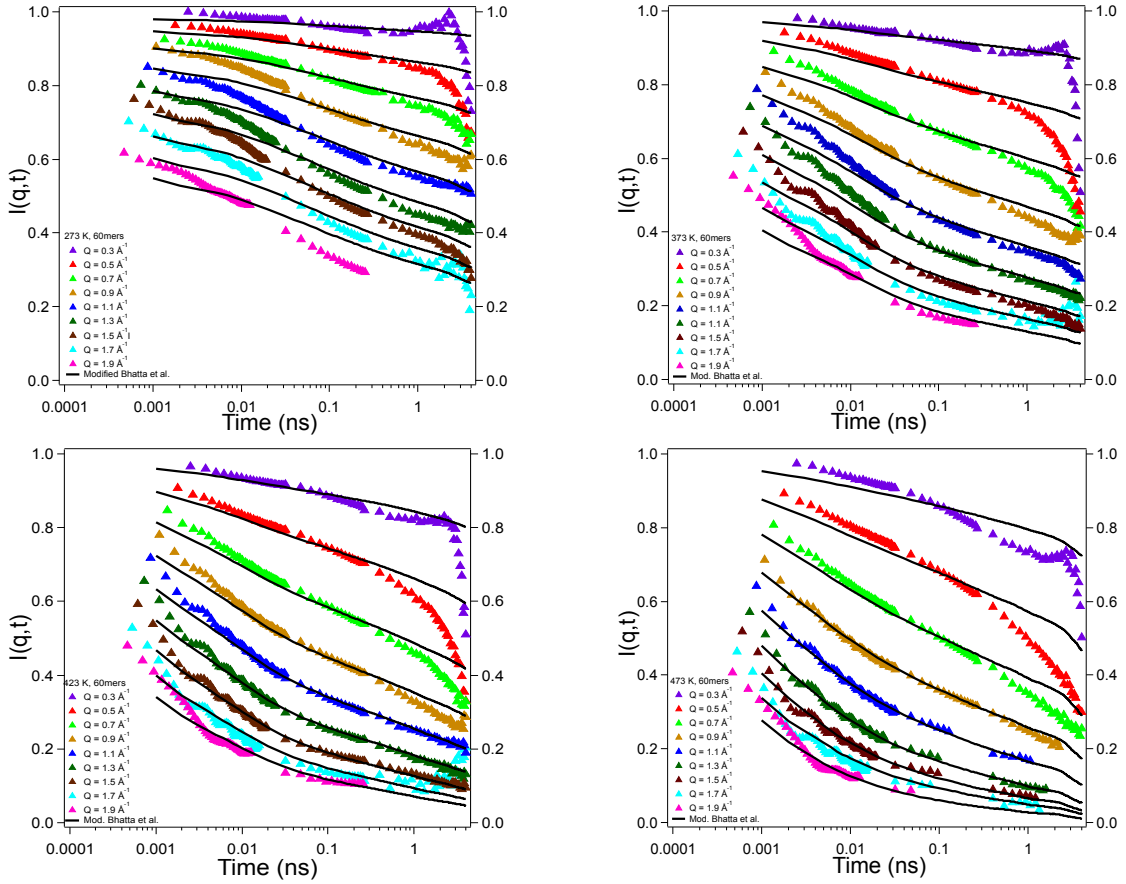

Figure A11: Comparisons of the calculated dynamic incoherent structure factors from MD simulations of P3HT-RRa using the Mod. Bhatta FF with experimental QENS data at 273 K (top right), 373 K (top left), 423 K (bottom right), and 473 K (bottom right).

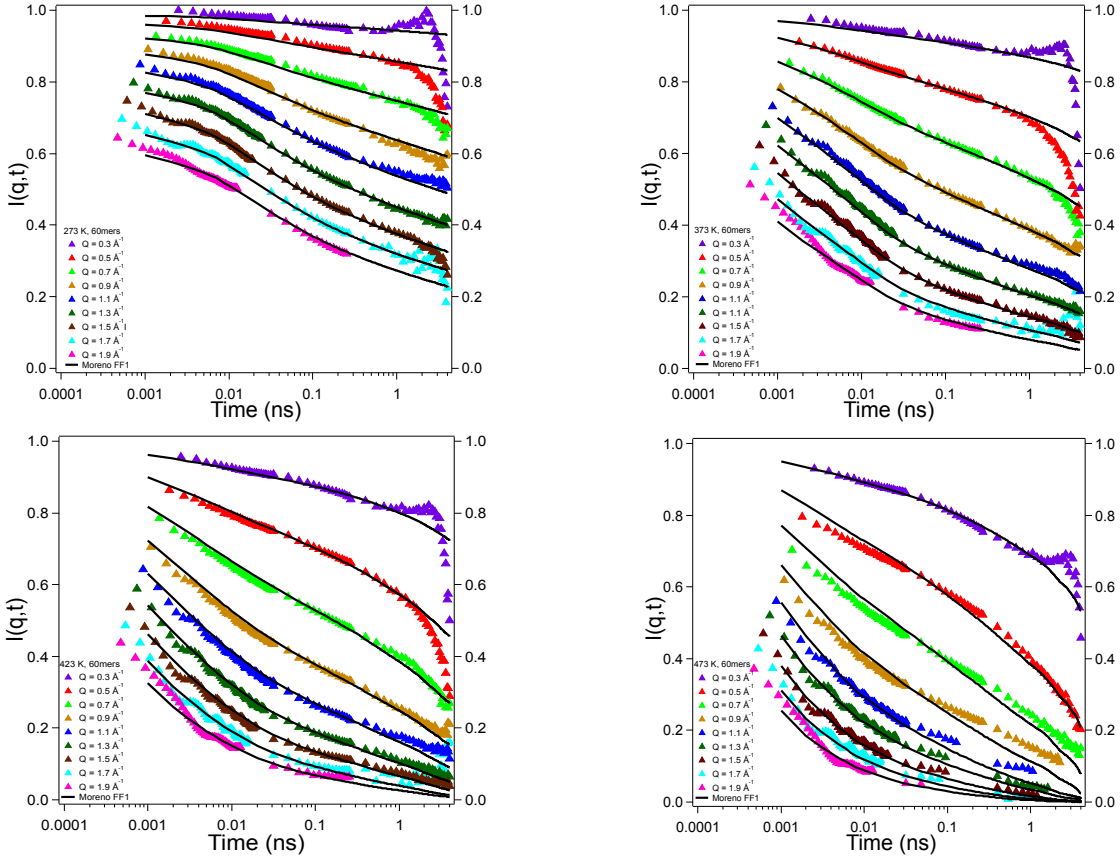

Figure A12: Comparisons of the calculated dynamic incoherent structure factors from MD simulations of P3HT-RRa using the Moreno FF1 force field with experimental QENS data at 273 K (top right), 373 K (top left), 423 K (bottom right), and 473 K (bottom right).

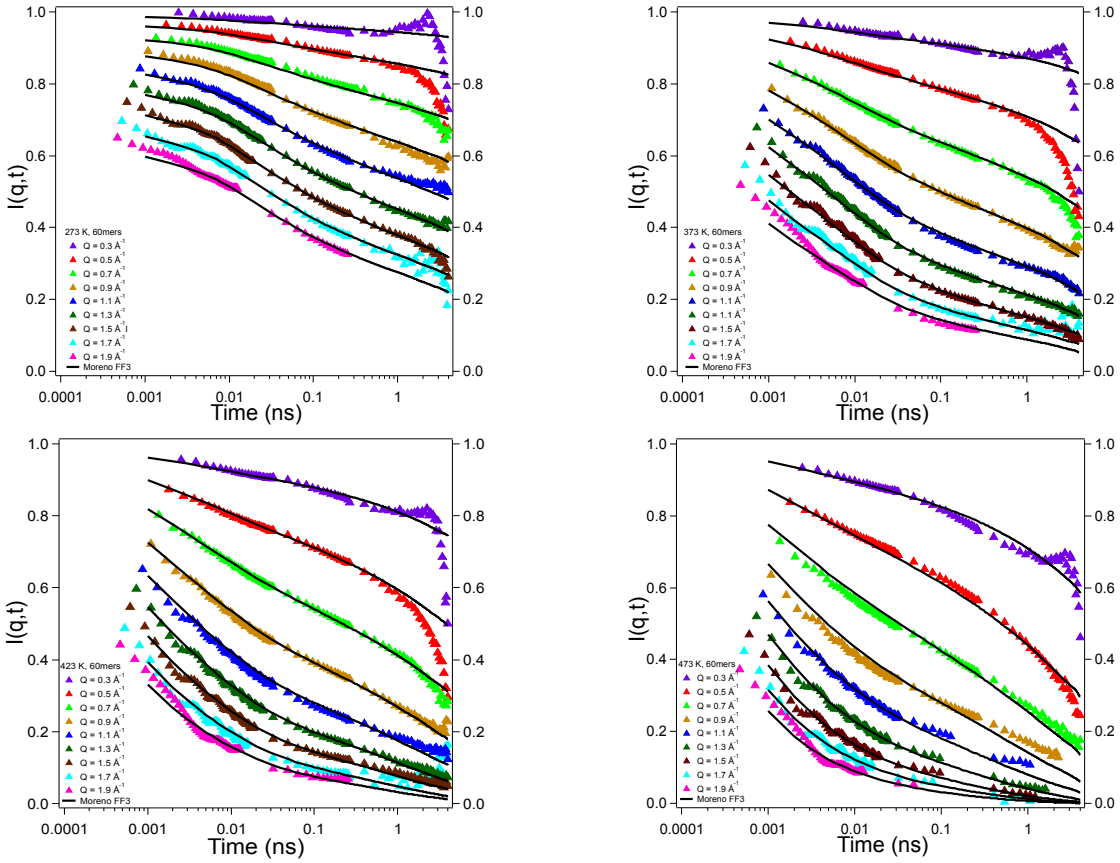

Figure A13: Comparisons of the calculated dynamic incoherent structure factors from MD simulations of P3HT-RRa using the Moreno FF3 force field with experimental QENS data at 273 K (top right), 373 K (top left), 423 K (bottom right), and 473 K (bottom right).

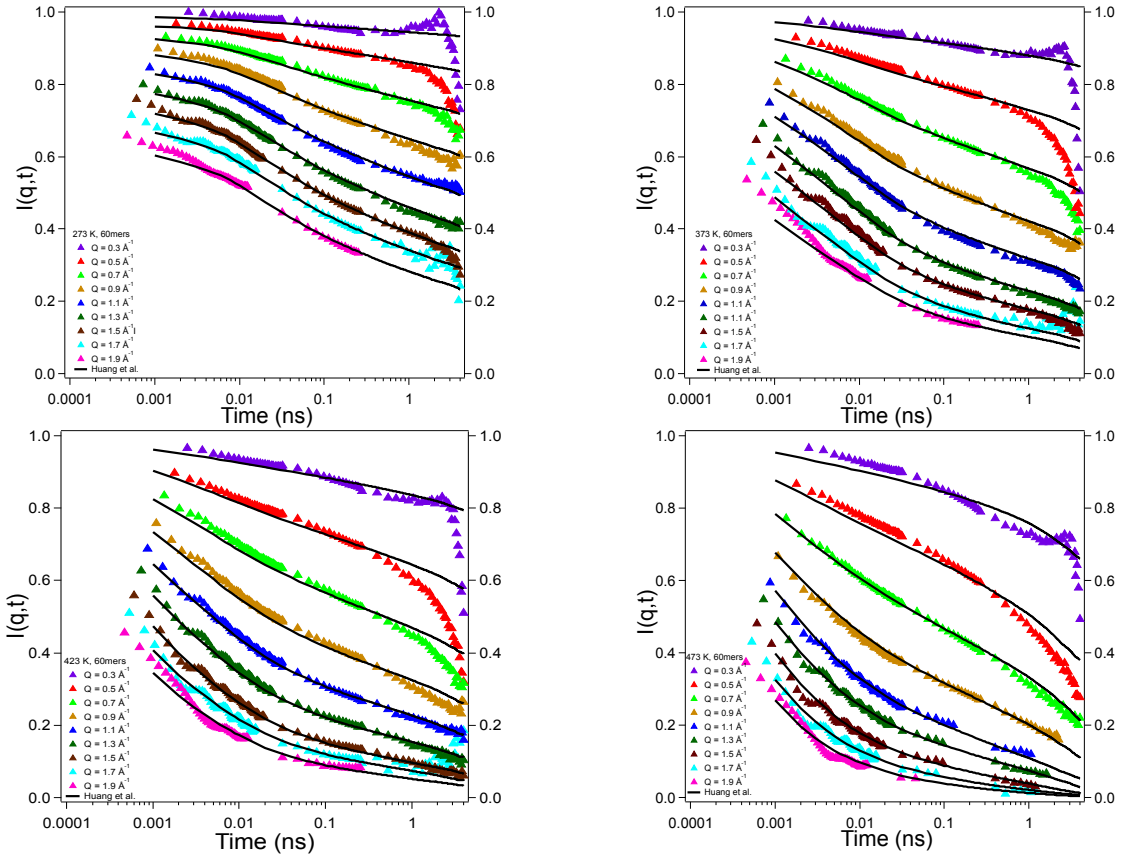

Figure A14: Comparisons of the calculated dynamic incoherent structure factors from MD simulations of P3HT-RRa using the Huang FF with experimental QENS data at 273 K (top right), 373 K (top left), 423 K (bottom right), and 473 K (bottom right).

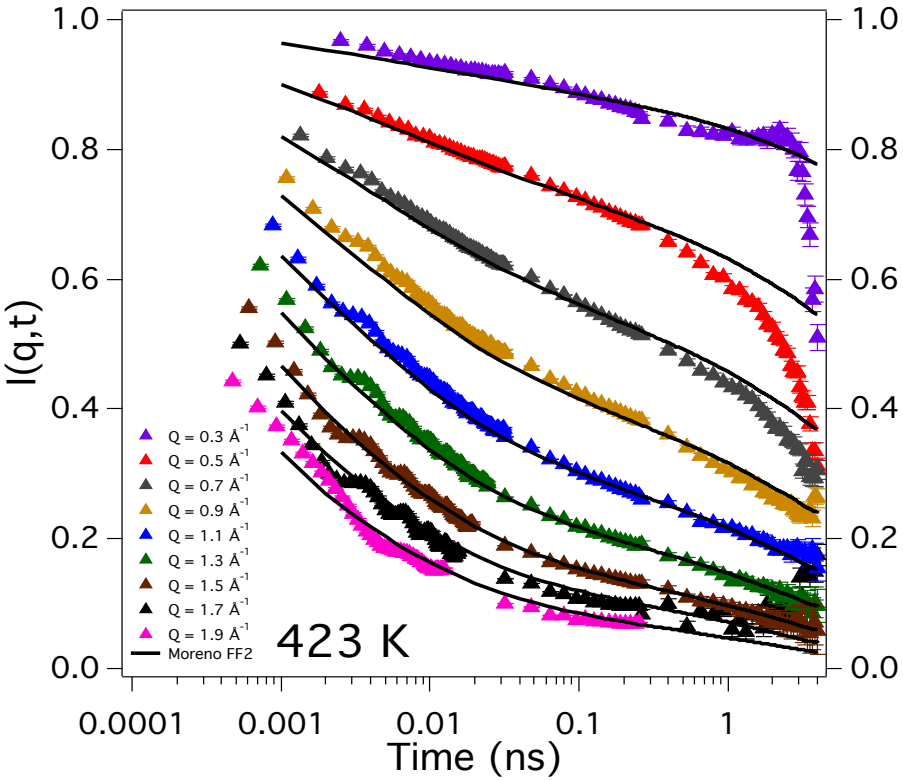

Figure A15: Figure 4.3.4c with error bars included for the experimental QENS data. The error bars are determined using the DAVE Fourier Transform Toolkit, which uses a "Bootstrap Monte-Carlo" method, and represent a single standard deviation. One million iteration steps were used when calculating the error using this method, which was far greater than the number of iterations required for the error values to converge.

Effect of Scaling Partial Charges

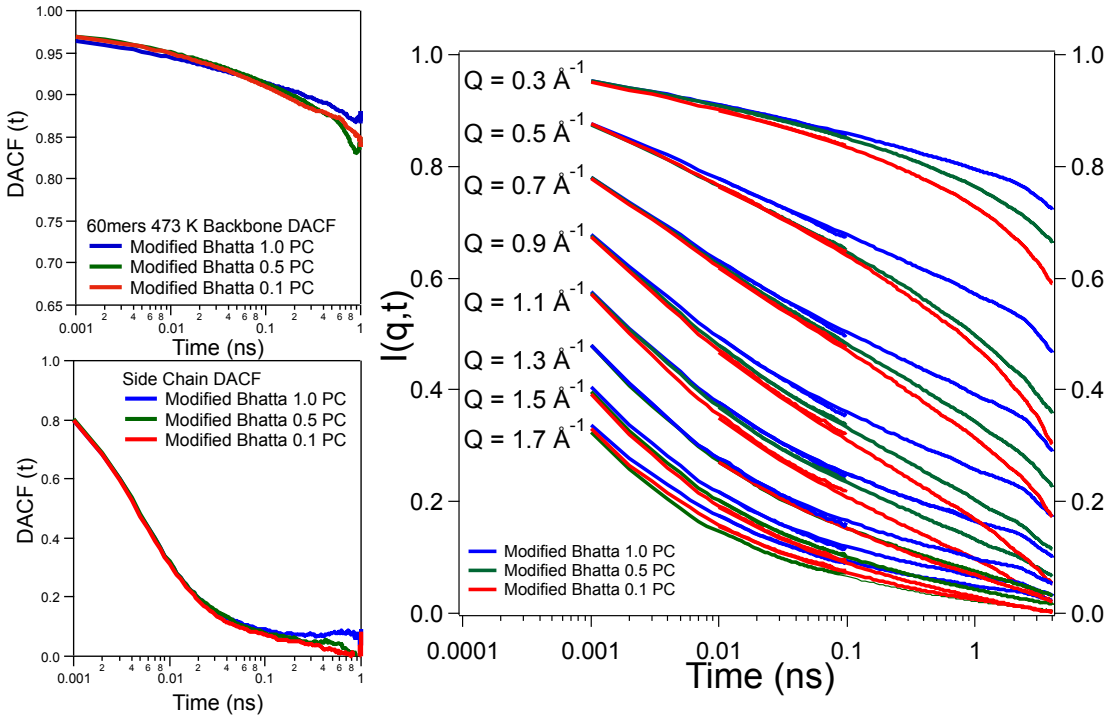

Figure A16: Right: Dynamic incoherent structure factors calculated for three MD simulations run using the Mod. Bhatta FF with all atomic partial charges are unscaled, scaled by a factor of 0.5, or scaled by a factor of 0.1. Left: Dihedral autocorrelation functions for the (Top) third side-chain carbon bond and the (Bottom) backbone for the same MD simulations.

In order to determine how differences in the magnitude of partial charges affect MD simulations, two simulations were run using the Mod. Bhatta FF: one with the atomistic partial charges scaled by 0.5, and another with the charges scaled by 0.1. Figure A16 shows the effect of scaling the atomic partial charges on the dynamic structure factor and DACFs calculated from MD simulations. The dihedral autocorrelation functions calculated for the backbone and for the third carbon-carbon bond show minimal changes as the partial charges are scaled. However, the calculated dynamic structure factors show noticeable changes for all Q values, with downward shifts occurring as the magnitude is

reduced by 50% and 90%. This may indicate that reducing the magnitude of the partial charges causes increased translational motions of the backbone and side chain.

Scaling Backbone Torsion Potentials

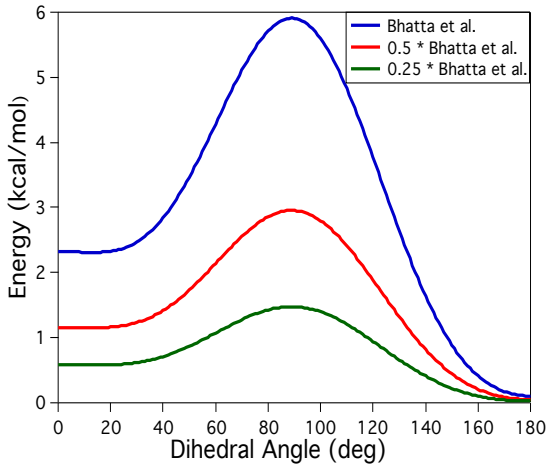

Figure A17: Backbone torsion potentials used in MD simulations to generate the dynamic structure factors and backbone DACFs of Figure 4.3.6 in the main text.

Effect of Changing Torsion Potential of Thiophene Bond with First Carbon in Side-Chain

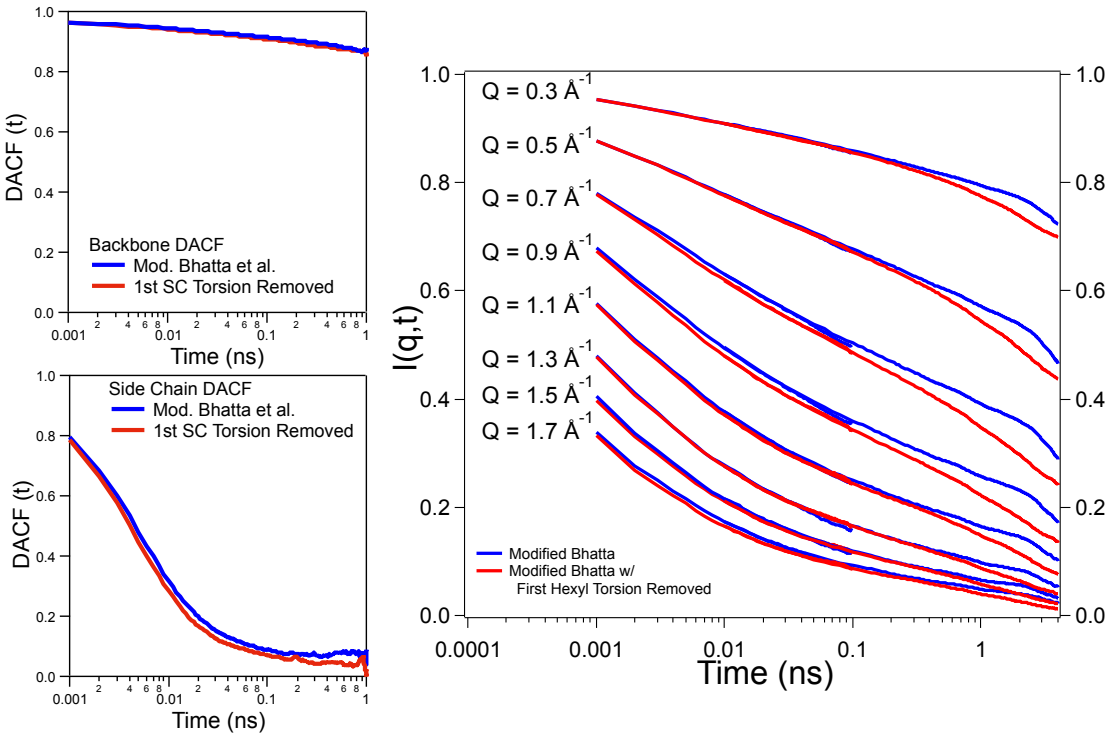

Figure A18: Right: Dynamic incoherent structure factors calculated for two MD simulations run using the Mod. Bhatta FF with the first side-chain torsion potential unchanged (blue) and with the same torsion potential removed (red). Left: Dihedral autocorrelation functions for the (Top) third side-chain carbon bond and the (Bottom) backbone for the same MD simulations.

We examined the effect of the torsion potential applied to the bond linking the side-chain to the thiophene ring (β_1) on the simulated dynamics. Figure A18 shows the effect of removing this torsion potential from the modified Bhatta et al. force field. The DACF calculations in Figure A18 show that the first side-chain hexyl torsion potential does not affect backbone torsion or torsional motions within the side-chain. However, the DISF calculated for the simulation without the β_1 torsion potential applied was shifted down relative to the DISF for the simulation with the neat modified Bhatta et al. force field. The shift was more prominent for $Q < 1.3$ Å^{-1}, which indicated an increase in

collective motions of the side-chain. This suggests that the bond to which this potential is applied acts as a "hinge", which hinders translational motions of the side-chain as a whole.

Reorientational Autocorrelation Function

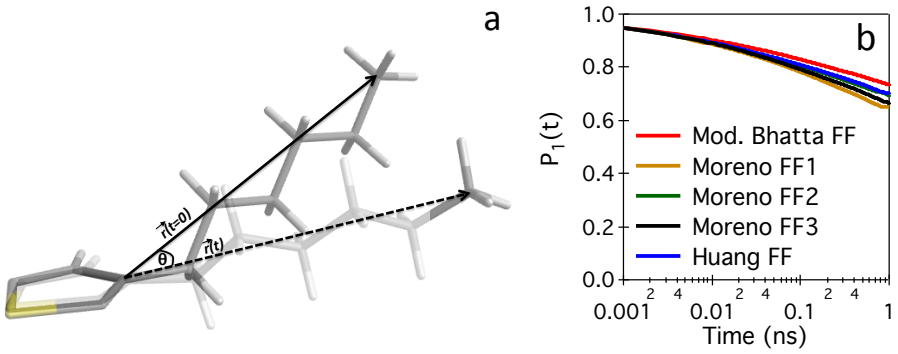

Figure A19: a) Schematic showing the vectors used for the P_1 calculation done for five MD simulations of amorphous P3HT run with different force fields. b) The results of the P_1 autocorrelation calculations for the same simulations.

Given that the QENS signal is dominated by the motions of the alkyl side-chains, it is necessary to determine the extent to which these motions were influenced by the motions of the thiophene backbone. We calculate the reorientational autocorrelation function P_1 using the following formula[80]:

$$\boldsymbol{P_1(t) = \langle Cos(\theta(t)) \rangle} \tag{A1}$$

given that

$$\boldsymbol{Cos(\theta(t)) = \vec{r}(t) * \vec{r}(t=0).} \tag{A2}$$

Here, $\vec{r}$ refers to the vector starting from the alkyl-substituted carbon (C2 in Figure 4.2.2d) at a given time, *t*, as seen in Figure A19a. The results are shown in Figure A19b. The Mod. Bhatta FF had the slowest P_1 relaxation because it had the strongest side-chain torsion potentials out of all of the force fields investigated, and it also showed reduced backbone torsional motions (see Figure 4.2.2). The Huang FF and Moreno FF2 show

nearly the same relaxation. This could suggest that the lack of the first side-chain torsion potential in the Huang FF is offset by its relatively stronger backbone torsion potential, when compared to Moreno FF2. Finally, when looking at the three Moreno force fields, which only differ in the atomic partial charges applied to the thiophene rings, there is a clear downward shift in the relaxation when going from Moreno FF2 to Moreno FF1 (and passing through Moreno FF3, which has the averaged partial charges of the other two Moreno force fields). By only tuning a single parameter related to the conjugated backbone, the atomic partial charges, a noticeable impact was observed on the motions of the hexyl side-chains. This clearly demonstrates that the backbone and side-chain motions are linked, and it is insufficient to parameterize force fields without accounting for this interdependence to a certain extent.

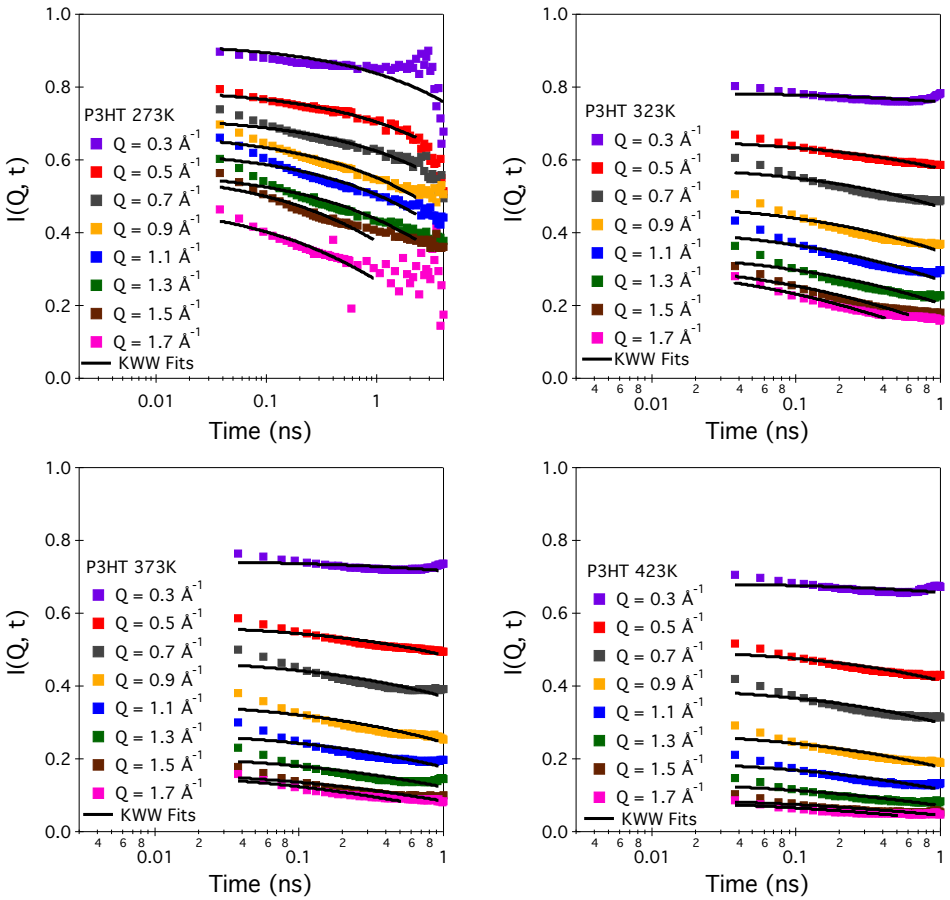

Figure A20: QENS data of regio-regular P3HT with fits corresponding to equation 2.2.5.

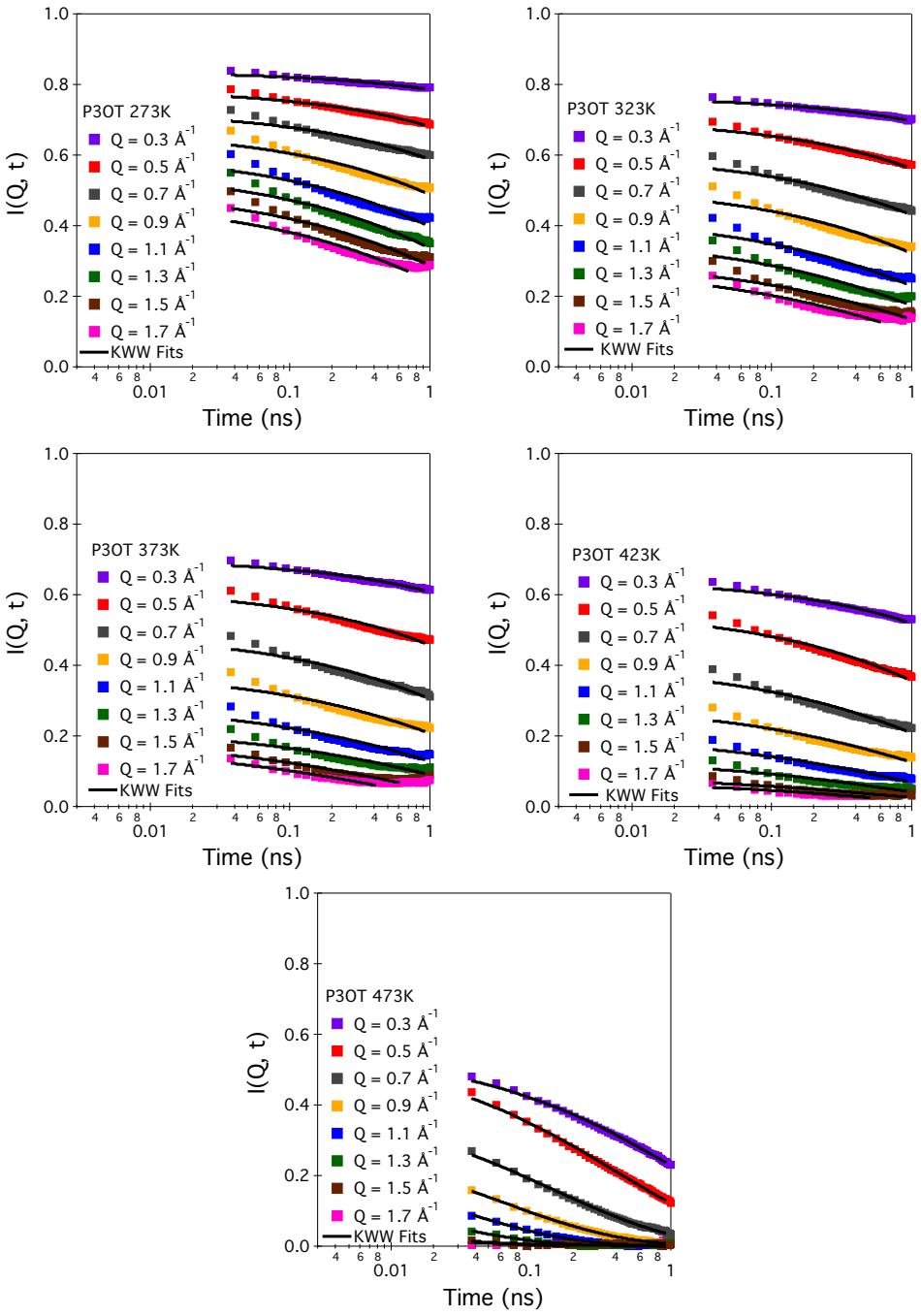

Figure A21: QENS data of regio-regular P3OT with fits corresponding to equation 2.2.5.

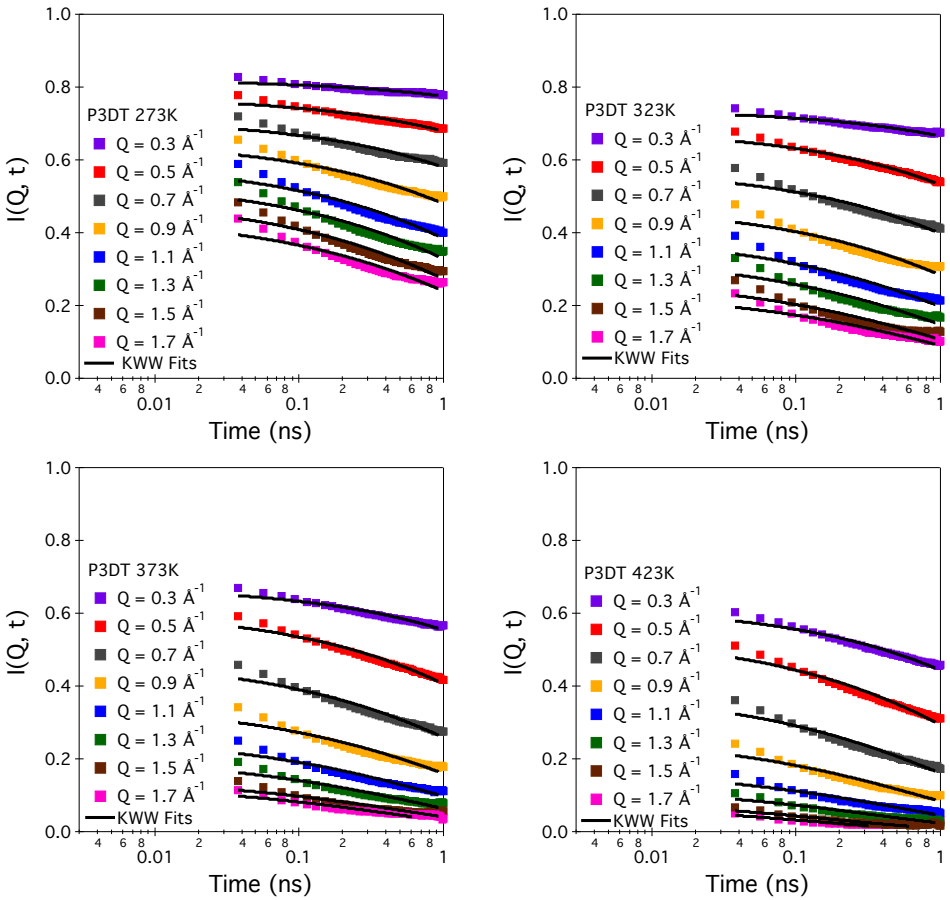

Figure A22: QENS data of regio-regular P3OT with fits corresponding to equation 2.2.5.

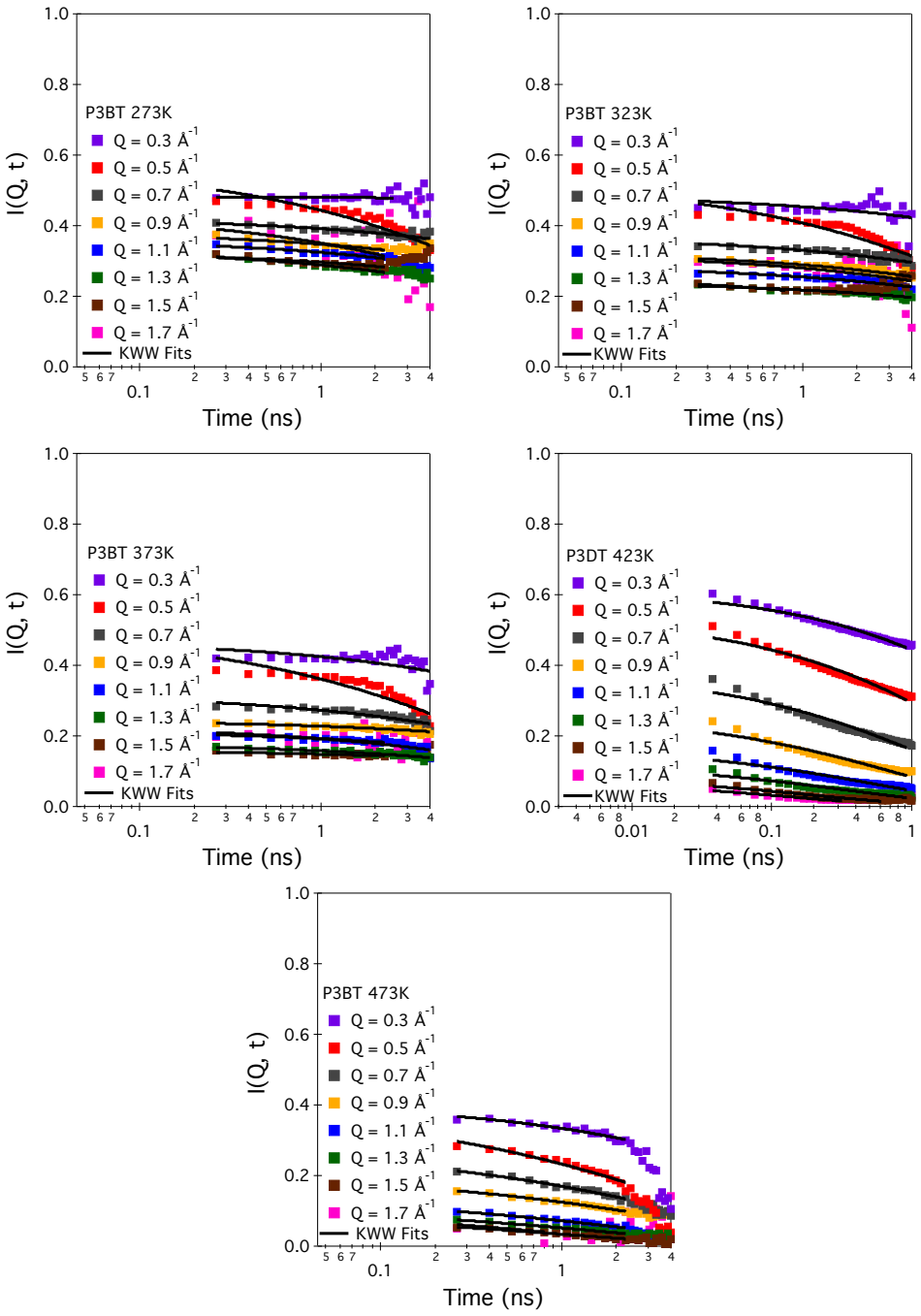

Figure A23: QENS data of regio-regular P3BT with fits corresponding to equation 2.2.5.

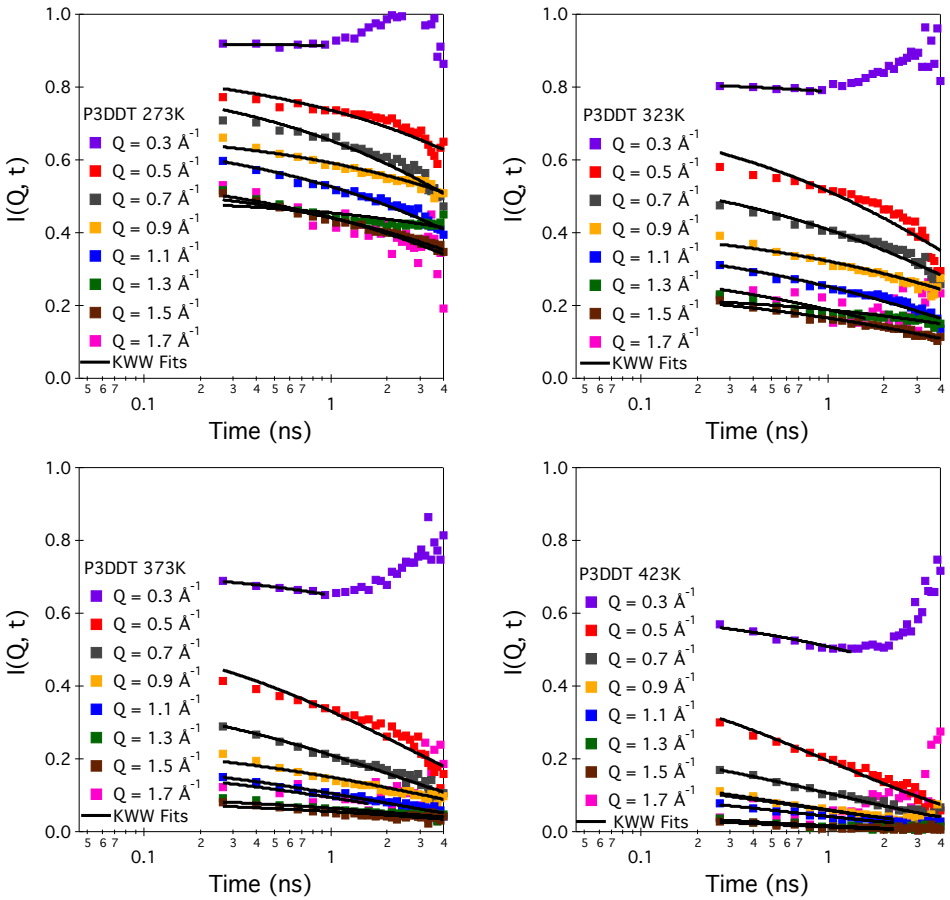

Figure A24: QENS data of regio-regular P3DDT with fits corresponding to equation 2.2.5.

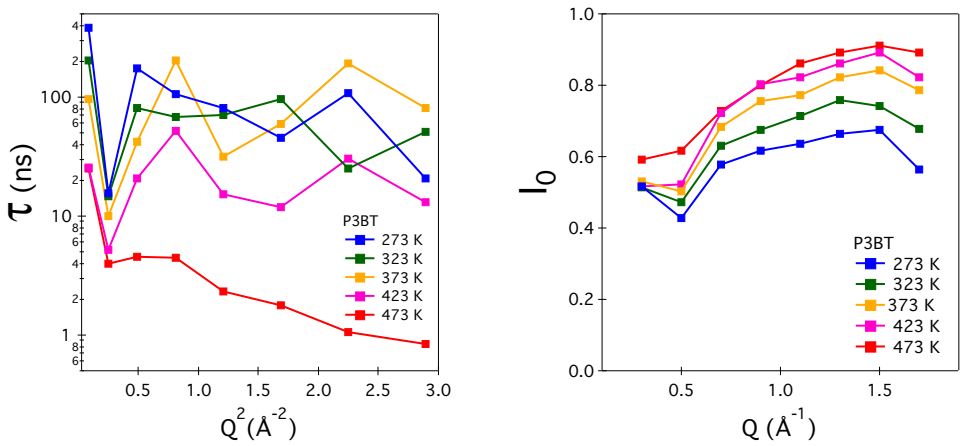

Figure A25: Characteristic relaxation times (τ) and constants (I_0) from fits of equation 2.2.5 to QENS data of P3BT.

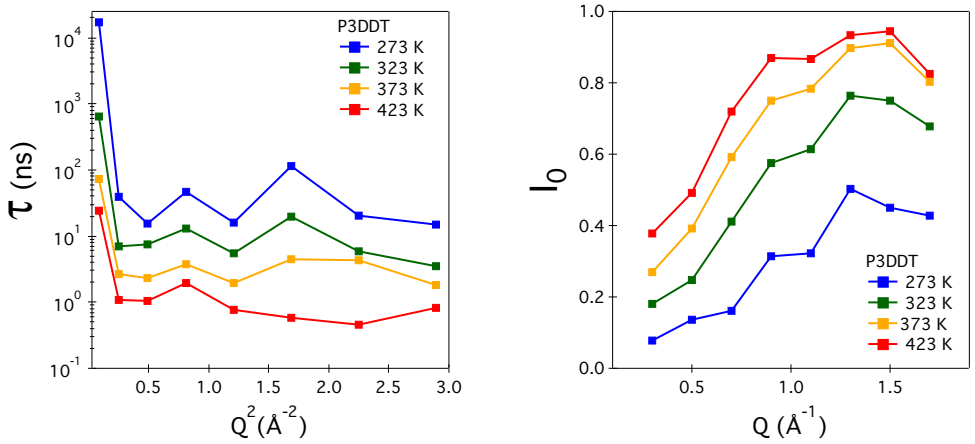

Figure A26: Characteristic relaxation times (τ) and constants (I_0) from fits of equation 2.2.5 to QENS data of P3DDT.

IGOR Code

WAXS Binning Code

```
#pragma rtGlobals=3             // Use modern global access method and strict wave access.
#include "linspace"             //Include linspace function similar to MATLAB linspace

Function Binning(a,b,n) //Function that requires user to pick a folder containing .pdh or
.txt files from SAXSQUANT.
                        // The program will go through each file and cut and bin the WAXS
data from a q value of a to b with n number of bins
        Variable a,b,n          //Parameters specified when calling function
        Wave loadedwave0,loadedwave1,loadedwave2
        Variable step, avg_range, i, j,qwave_range, qmin, qmax, i_sum, i_count, i_dev,
f1,l1,currentline,index,num                 //Declare local variables and waves
        String pathname,filename,fileadd

        NewPath/O pathname // This will put up a dialog
                if (V_flag != 0)
                        return -1 // User cancelled
                endif

        do



                fileName = IndexedFile(pathName, index, ".txt")

                if (strlen(fileName) == 0) // No more files?
                        break // Break out of loop
                endif

                currentline = 5 //Set to 0 if deleted first 5 lines of text files.

                Open/R/P=pathname l1 as filename


        LoadWave/O/G/P=pathname/N=loadedwave/L={0,currentline,0,0,0}/Q  fileName

                        if (V_flag==0) // No waves loaded. Perhaps user canceled.

                                Abort "Unexpected end of file"

                        endif

                Close l1
```

```
		Make/D/N=(dimsize(loadedwave0,0))/O q_wave = loadedwave0
		Make/D/N=(dimsize(loadedwave1,0))/O i_wave = loadedwave1

		Make/D/N=(dimsize(loadedwave2,0))/O s_wave = loadedwave2

		step = (b-a)/(n-1)					//Calculate stepsize
(see linspace procedure)

		Make/D/N=(n)/O binpoints_q = linspace(a,b,n)		//Make output q, i,
and s arrays
		Make/D/N=(n)/O binpoints_i = binpoints_q
		Make/D/N=(n)/O binpoints_s = binpoints_q

		avg_range = step/2					//Specify range of
each bin

		qwave_range = numpnts(q_wave)				//determine the total
number of points in input q wave

		for (i=0; i<n; i+=1)
		//going through all n points defined by user
			qmin = binpoints_q[i]-avg_range				//
			qmax = binpoints_q[i]+avg_range
			i_sum = 0
			i_count = 0
			i_dev = 0
			for (j=0 ; j<qwave_range; j+=1)

				if (q_wave[j]>qmin && q_wave[j] <= qmax)

					i_sum += i_wave[j]
					i_count +=1

				endif

			endfor


			binpoints_i[i] = i_sum/i_count


			for (j=0 ; j<qwave_range; j+=1)

				if (q_wave[j]>qmin && q_wave[j] <= qmax)
```

```
                                        i_dev += ((i_wave[j]-binpoints_i[i])^2)/i_count

                                endif

                        endfor

                        binpoints_s[i] = i_dev^(1/2)

                endfor

                filename = RemoveEnding(filename, ".txt")
                sprintf fileadd "_%dpoints.pdh",n
                filename +=fileadd

                Open/P=pathname f1 as filename

                        fprintf f1, "\r"
                        fprintf f1, "SAXS BOX\r"
                        fprintf f1, "    %d        0        0        0        0        0        0        0
\r", n
                        fprintf f1, "  0.000000E+00   2.612000E+02   0.000000E+00
1.000000E+00   1.542000E-01 \r"
                        fprintf f1, "  2.500000E+01   1.557578E+00   0.000000E+00
0.000000E+00   0.000000E+00  \r"
                        wfprintf f1, "  %0.4E     %E   %E\r"
binpoints_q,binpoints_i,binpoints_s
                        fprintf f1, "<?xml version=\"1.0\" encoding=\"utf-8\"?>\r"
                        fprintf f1, "<fileinfo version=\"3.51.100918\"> \r"
                        fprintf f1, "  <column key=\"X\">\r"
                        fprintf f1, "    <value key=\"unit\">n_m^-1</value>\r"
                        fprintf f1, "    <value
key=\"quantity\">SCATTERING_VECTOR</value>\r"
                        fprintf f1, "  </column>\r"
                        fprintf f1, "  <column key=\"Y\">\r"
                        fprintf f1, "    <value key=\"unit\">u_m^-2</value>\r"
                        fprintf f1, "    <value
key=\"quantity\">COUNTS_PER_AREA</value>\r"
                        fprintf f1, "  </column>\r"
                        fprintf f1, "  <parameter key=\"CounterSlitLength\">\r"
                        fprintf f1, "    <value key=\"value\">1.55757776118539</value>\r"
                        fprintf f1, "    <value key=\"stddev\">-1</value>\r"
                        fprintf f1, "    <value key=\"unit\">n_m^-1</value>\r"
                        fprintf f1, "    <value
key=\"quantity\">SCATTERING_VECTOR</value>\r"
                        fprintf f1, "  </parameter>\r"
                        fprintf f1, "  <parameter key=\"SampleDetector\">\r"
```

```
                        fprintf f1, "    <value key=\"value\">261.2</value>\r"
                        fprintf f1, "    <value key=\"stddev\">-1</value>\r"
                        fprintf f1, "    <value key=\"unit\">m_m</value>\r"
                        fprintf f1, "    <value key=\"quantity\">DISTANCE</value>\r"
                        fprintf f1, "  </parameter>\r"
                        fprintf f1, "  <parameter key=\"DetectorRadius\">\r"
                        fprintf f1, "    <value key=\"value\">260</value>\r"
                        fprintf f1, "    <value key=\"stddev\">-1</value>\r"
                        fprintf f1, "    <value key=\"unit\">m_m</value>\r"
                        fprintf f1, "    <value key=\"quantity\">DISTANCE</value>\r"
                        fprintf f1, "  </parameter>\r"
                        fprintf f1, "  <parameter key=\"Wavelength\">\r"
                        fprintf f1, "    <value key=\"value\">0.1542</value>\r"
                        fprintf f1, "    <value key=\"stddev\">-1</value>\r"
                        fprintf f1, "    <value key=\"unit\">n_m</value>\r"
                        fprintf f1, "    <value
key=\"quantity\">WAVELENGTH</value>\r"
                        fprintf f1, "  </parameter>\r"
                        fprintf f1, "  <parameter key=\"Absorption\">\r"
                        fprintf f1, "    <value key=\"value\">1</value>\r"
                        fprintf f1, "    <value key=\"stddev\">-1</value>\r"
                        fprintf f1, "    <value key=\"unit\">u_m^-2</value>\r"
                        fprintf f1, "    <value
key=\"quantity\">COUNTS_PER_AREA</value>\r"
                        fprintf f1, "  </parameter>\r"
                        fprintf f1, "  <parameter key=\"Temperature\">\r"
                        fprintf f1, "    <value key=\"value\">25</value>\r"
                        fprintf f1, "    <value key=\"stddev\">-1</value>\r"
                        fprintf f1, "    <value key=\"unit\">degC</value>\r"
                        fprintf f1, "    <value
key=\"quantity\">TEMPERATURE</value>\r"
                        fprintf f1, "  </parameter>\r"
                        fprintf f1, "  <parameter key=\"Concentration\">\r"
                        fprintf f1, "    <value key=\"value\">0</value>\r"
                        fprintf f1, "    <value key=\"stddev\">-1</value>\r"
                        fprintf f1, "    <value key=\"unit\">g*l^-1</value>\r"
                        fprintf f1, "    <value
key=\"quantity\">CONCENTRATION_MASS</value>\r"
                        fprintf f1, "  </parameter>\r"
                        fprintf f1, "</fileinfo>\r"
                Close f1

                //Save/J/O/W/F/P=Downloads binpoints_i,binpoints_q,binpoints_s as
"binpoints_q++.pdh"

                index +=1
```

```
	while (1)

end
```

Code to calculate vertical shift factors (Both for aligning QENS data from separate instruments and for aligning stitched QENS data to simulated I(q, t)s

```
#pragma rtGlobals=3		// Use modern global access method and strict wave access.

Function InterpFit(InwaveA_Y, InwaveA_X, InwaveB_Y, InwaveB_X,xstart,xend) // Function takes input wave A, asks for range in X values, interpolates Y values for the X range, then uses least squares minimization to fit the interpolated Y values to the same interpolation done for input wave B. The output is a vertical shift factor.

	Wave InwaveA_Y, InwaveA_X, InwaveB_Y, InwaveB_X
	Variable xstart,xend

	Variable xstep, xrange,comp_xstart, indexcounter1,indexstart_AX,indexstart_BX, indexend_AX, indexend_BX, i, shift,Sumsq_Resid1,Sumsq_Resid2, Norm_SSR


	//First need to grab index values from the input wave X values

	indexstart_AX = 0
	indexstart_BX = 0

	indexend_AX = 0
	indexend_BX = 0


	for (indexcounter1 = 0 ; indexcounter1 < dimsize(InwaveA_X,0) ; indexcounter1+=1)

		if (InwaveA_X[indexcounter1] >= xstart && indexstart_AX ==0)
			indexstart_AX = indexcounter1-1
			if (indexstart_AX == 0)
				print/F "range is out of bounds"
			endif
		endif

		if (InwaveA_X[indexcounter1] >= xend && indexend_AX ==0)
			indexend_AX = indexcounter1-1
			if (indexend_AX == 0)
```

```
                print/F "range is out of bounds"
            endif
        endif

        indexcounter1 +=1

    endfor


    for (indexcounter1 = 0 ; indexcounter1 < dimsize(InwaveB_X,0) ;
indexcounter1+=1)

        if (InwaveB_X[indexcounter1] >= xstart && indexstart_BX ==0)
            indexstart_BX = indexcounter1-1
            if (indexstart_BX == 0)
                print/F "range is out of bounds"
            endif
        endif

        if (InwaveB_X[indexcounter1] >= xend && indexend_BX ==0)
            indexend_BX = indexcounter1-1
            if (indexend_BX == 0)
                print/F "range is out of bounds"
            endif
        endif

        indexcounter1 +=1

    endfor



    //Determine outer bounds for interpolation

    if (InwaveA_X[indexstart_AX] > InwaveB_X[indexstart_BX])

        comp_xstart = InwaveB_X[indexstart_BX]

        if (InwaveA_X[indexend_AX] < InwaveB_X[indexend_BX])

            xrange = InwaveA_X[indexend_AX] -
InwaveB_X[indexstart_BX]

        endif

        if (InwaveA_X[indexend_AX] > InwaveB_X[indexend_BX])
```

```
                xrange = InwaveB_X[indexend_BX] -
InwaveB_X[indexstart_BX]

            endif
        endif

        if (InwaveA_X[indexstart_AX] < InwaveB_X[indexstart_BX])

            comp_xstart = InwaveA_X[indexstart_AX]

            if (InwaveA_X[indexend_AX] < InwaveB_X[indexend_BX])

                xrange = InwaveA_X[indexend_AX] -
InwaveA_X[indexstart_AX]

            endif

            if (InwaveA_X[indexend_AX] > InwaveB_X[indexend_BX])

                xrange = InwaveB_X[indexend_BX] -
InwaveA_X[indexstart_AX]

            endif
        endif

        xstep = xrange/100

        // Make comparison X wave

        Make/D/N=100/O comp_xwave

        for (i = 0 ; i <100 ; i +=1)

            comp_xwave[i] = comp_xstart + i*xstep


        endfor

        //Make comparison Y wave for inputwave A

        Make/D/N=100/O comp_ywaveA

        for (i = 0 ; i <100 ; i +=1)

         comp_ywaveA[i] = interp(comp_xwave[i], InwaveA_X, InwaveA_Y)
```

```
        endfor

        //Make comparison Y wave for inputwave B

        Make/D/N=100/O comp_ywaveB

        for (i = 0 ; i <100 ; i +=1)

                comp_ywaveB[i] = interp(comp_xwave[i], InwaveB_X, InwaveB_Y)

        endfor

        //Define shift factor as difference between averages of comp_ywaveA and
comp_ywaveB

        Shift = sum(comp_ywaveA)/100 - sum(comp_ywaveB)/100


        Make/D/N=100/O comp_Resid


        comp_Resid = ((comp_ywaveB+Shift)-comp_ywaveA)^2

        Sumsq_Resid1 = sum(comp_Resid)

        print/F Shift
        print/F Sumsq_Resid1


        Return Shift


end
```

Bibliography

1 R. D. McCullough, *Adv. Mater.*, 1998, **10**, 93–116.
2 C. Sekine, Y. Tsubata, T. Yamada, M. Kitano and S. Doi, *Sci. Technol. Adv. Mater.*, 2014, **15**, 34203.
3 J. Mei, Y. Diao, A. L. Appleton, L. Fang and Z. Bao, 2013.
4 M. He, F. Qiu and Z. Lin, *Energy Environ. Sci.*, 2013, **6**, 1352.
5 K.-Y. Jen, G. G. Miller and R. L. Elsenbaumer, *J. Chem. Soc.{,} Chem. Commun.*, 1986, 1346–1347.
6 R. D. McCullough and R. D. Lowe, *J. Chem. Soc.{,} Chem. Commun.*, 1992, 70–72.
7 a. Salleo, T. W. Chen, a. R. Völkel, Y. Wu, P. Liu, B. S. Ong and R. a. Street, *Phys. Rev. B - Condens. Matter Mater. Phys.*, 2004, **70**, 1–10.
8 I. McCulloch, M. Heeney, C. Bailey, K. Genevicius, I. Macdonald, M. Shkunov, D. Sparrowe, S. Tierney, R. Wagner, W. Zhang, M. L. Chabinyc, R. J. Kline, M. D. McGehee and M. F. Toney, *Nat. Mater.*, 2006, **5**, 328–333.
9 H. N. Tsao, D. M. Cho, I. Park, M. R. Hansen, A. Mavrinskiy, D. Y. Yoon, R. Graf, W. Pisula, H. W. Spiess and K. Müllen, *J. Am. Chem. Soc.*, 2011, **133**, 2605–2612.
10 P. Lindner and T. Zemb, Eds., *Neutrons, X-rays and Light: Scattering Methods Applied to Soft Condensed Matter*, Elsevier B.V., Amsterdam, 1st edn., 2002.
11 R. Noriega, J. Rivnay, K. Vandewal, F. P. V Koch, N. Stingelin, P. Smith, M. F. Toney and A. Salleo, *Nat. Mater.*, 2013, **12**, 1038–44.
12 S. Dag, L. Wang, R. V January, V. Re, M. Recei and V. March, 2010, 5997–6000.
13 J. Balko, R. H. Lohwasser, M. Sommer, M. Thelakkat and T. Thurn-Albrecht, *Macromolecules*, 2013, **46**, 9642–9651.
14 A. Furrer, J. Mesot and T. Strassle, *Neutron Scattering in Condensed Matter Physics*, World Scientific Publishing Company, 1st edn., 2009.
15 J. Colmenero and A. Arbe, *J. Polym. Sci. Part B Polym. Phys.*, 2013, **51**, 87–113.
16 I. Hoffmann, *Colloid Polym. Sci.*, 2014, 2053–2069.
17 T. Liu and A. Troisi, *Adv. Funct. Mater.*, 2014, **24**, 925–933.
18 O. D. Bernardinelli, S. M. Cassemiro, L. a O. Nunes, T. D. Z. Atvars, L. Akcelrud and E. R. De Azevedo, *J. Phys. Chem. B*, 2012, **116**, 5993–6002.
19 D. P. McMahon, D. L. Cheung, L. Goris, J. Dacuña, A. Salleo and A. Troisi, *J. Phys. Chem. C*, 2011, **115**, 19386–19393.
20 J. C. Phillips, *Reports Prog. Phys.*, 1999, 59, 1133–1207.
21 A. Arbe, F. Alvarez and J. Colmenero, *Soft Matter*, 2012, **8**, 8257.
22 J. Obrzut and K. a. Page, *Phys. Rev. B*, 2009, **80**, 195211.
23 G. Paternó, F. Cacialli and V. García-Sakai, *Chem. Phys.*, 2013, **427**, 142–146.
24 T. Etampawala, D. Ratnaweera, B. Morgan, S. Diallo, E. Mamontov and M. Dadmun, *Polymer (Guildf).*, 2015, **61**, 155–162.
25 D. Djurado, M. Bée, M. Sniechowski, S. Howells, P. Rannou, A. Pron, J. P. Travers and W. Luzny, *Phys. Chem. Chem. Phys.*, 2005, **7**, 1235–1240.
26 M. Śniechowski, W. Łuzny, D. Djurado, B. Dufour, P. Rannou, a. Proń, M. Bee, M. Johnson and M. Gonzales, *Fibres Text. East. Eur.*, 2005, **13**, 96–99.
27 D. Djurado, M. Sniechowski, M. Bée, M. Johnson, M. a. Gonzalez, P. Rannou and

A. Pron, *Macromol. Symp.*, 2006, **241**, 28–33.
28 M. Moreno, M. Casalegno, G. Raos, S. V. Meille and R. Po, *J. Phys. Chem. B*, 2010, **114**, 1591–1602.
29 R. S. Bhatta, Y. Y. Yimer, D. S. Perry and M. Tsige, *J. Phys. Chem. B*, 2013, **117**, 10035–45.
30 R. W. Darbeau, *Appl. Spectrosc. Rev.*, 2006, **41**, 401–425.
31 T.-A. Chen, X. Wu and R. D. Rieke, *J. Am. Chem. Soc.*, 1995, **117**, 233–244.
32 K. Yazawa, Y. Inoue, T. Shimizu, M. Tansho and N. Asakawa, 2010, 1241–1248.
33 J. C. Moore, *J. Polym. Sci. Part A Gen. Pap.*, 1964, **2**, 835–843.
34 Z. Grubisic, P. Rempp and H. Benoit, *J. Polym. Sci. Part B Polym. Lett.*, 1967, **5**, 753–759.
35 J. Liu, R. S. Loewe and R. D. Mccullough, *Macromolecules*, 1999, 5777–5785.
36 E. Turi, *Thermal characterization of polymeric materials*, Elsevier, 2012.
37 K. Yazawa, Y. Inoue, T. Yamamoto and N. Asakawa, 2006, 1–13.
38 X. Shen, W. Hu and T. P. Russell, *Macromolecules*, 2016, acs.macromol.6b00799.
39 W. Koch and M. C. Holthausen, *A Chemist's Guide to Density Functional Theory*, 2001, vol. 3.
40 D. Frenkel and B. Smit, *Understanding Molecular Simulation: From Algorithms to Applications*, Elsevier Science, 2001.
41 M. A. González, *Collect. SFN*, 2011, **12**, 169–200.
42 D. M. Huang, R. Faller, K. Do and A. J. Moul, *J. Chem. Theory Comput.*, 2010, 1–11.
43 G. Raos, A. Famulari and V. Marcon, *Chem. Phys. Lett.*, 2003, **379**, 364–372.
44 C. S. Lee and M. D. Dadmun, *Polymer (Guildf).*, 2014, **55**, 4–7.
45 T. Róg, K. Murzyn, K. Hinsen and G. R. Kneller, *J. Comput. Chem.*, 2003, **24**, 657–667.
46 A. Salleo, *Mater. Today*, 2007, **10**, 38–45.
47 D. Alberga, A. Perrier, I. Ciofini, G. F. Mangiatordi, G. Lattanzi, and K. N. Houk, *Phys. Chem. Chem. Phys.*, 2015, **17**, 18742–18750.
48 M. Bernardi and J. C. Grossman, *Energy Environ. Sci.*, 2016.
49 C. Poelking, K. Daoulas, A. Troisi and D. Andrienko, in *P3HT Revisited -- From Molecular Scale to Solar Cell Devices*, ed. S. Ludwigs, Springer Berlin Heidelberg, Berlin, Heidelberg, 2014, pp. 139–180.
50 N. Vukmirovic and L. Wang, *J Phys Chem B*, 2012, **115**, 1792–1797.
51 M. Mladenović and N. Vukmirović, *Phys. Chem. Chem. Phys.*, 2014, **16**, 25950–25958.
52 C. Poelking and D. Andrienko, *Macromolecules*, 2013, **46**, 8941–8956.
53 M. Brodeck, F. Alvarez, a Arbe, F. Juranyi, T. Unruh, O. Holderer, J. Colmenero and D. Richter, *J. Chem. Phys.*, 2009, **130**, 94908.
54 J. Colmenero, M. Brodeck, A. Arbe and D. Richter, *Macromolecules*, 2013, **46**, 1678–1685.
55 A. Arbe, *J. Phys. Soc. Japan*, 2013, **82**, SA015.
56 A. A. Y. Guilbert, A. Urbina, J. Abad, C. Díaz-Paniagua, F. Batallán, T. Seydel, M. Zbiri, V. García-Sakai and J. Nelson, *Chem. Mater.*, 2015, **27**, 7652–7661.
57 C. R. Snyder, R. C. Nieuwendaal, D. M. DeLongchamp, C. K. Luscombe, P. Sista and S. D. Boyd, *Macromolecules*, 2014, **47**, 3942–3950.

58 E. Mamontov and K. W. Herwig, *Rev. Sci. Instrum.*, 2011, **82**.
59 J. R. D. Copley and J. C. Cook, *Chem. Phys.*, 2003, **292**, 477–485.
60 A. Meyer, R. M. Dimeo, P. M. Gehring and D. A. Neumann, *Rev. Sci. Instrum.*, 2003, **74**, 2759–2777.
61 R. T. Azuah, L. R. Kneller, Y. Qiu, P. L. W. Tregenna-Piggott, C. M. Brown, J. R. D. Copley and R. M. Dimeo, *J. Res. Natl. Inst. Stand. Technol.*, 2009, **114**, 341.
62 O. Arnold, J. C. Bilheux, J. M. Borreguero, A. Buts, S. I. Campbell, L. Chapon, M. Doucet, N. Draper, R. Ferraz Leal, M. A. Gigg, V. E. Lynch, A. Markvardsen, D. J. Mikkelson, R. L. Mikkelson, R. Miller, K. Palmen, P. Parker, G. Passos, T. G. Perring, P. F. Peterson, S. Ren, M. A. Reuter, A. T. Savici, J. W. Taylor, R. J. Taylor, R. Tolchenov, W. Zhou and J. Zikovsky, *Nucl. Instruments Methods Phys. Res. Sect. A Accel. Spectrometers, Detect. Assoc. Equip.*, 2014, **764**, 156–166.
63 L. V. N. R. Ganapatibhotla and J. K. Maranas, 2014.
64 F. Alvarez, A. Arbe, J. Colmenero, R. Zorn and D. Richter, *Comput. Mater. Sci.*, 2002, **25**, 596–605.
65 S. Plimpton, *J. Comput. Phys.*, 1995, **117**, 1–19.
66 M. J. Robertson, J. Tirado-Rives and W. L. Jorgensen, *J. Chem. Theory Comput.*, 2015, **11**, 3499–3509.
67 R. W. Hockney and J. W. Eastwood, *Computer Simulation Using Particles*, CRC Press, 1988.
68 Y. Y. Yimer and M. Tsige, *J. Chem. Phys.*, 2012, **137**.
69 D. E. Motaung, G. F. Malgas, C. J. Arendse, S. E. Mavundla, C. J. Oliphant and D. Knoesen, *J. Mater. Sci.*, 2009, **44**, 3192–3197.
70 R. Zhang, B. Li, M. C. Iovu, M. Jeffries-el, G. Sauve, J. Cooper, S. Jia, S. Tristram-Nagle, D. M. Smilgies, D. N. Lambeth, R. D. McCullough and T. Kowalewski, *J. Am. Chem. Soc.*, 2006, **128**, 3480–3481.
71 R. Liping, Z. Guoqiang and Y. Shua, *Proc. 17th IAPRI World Conf. Packag.*, 2010, 212–216.
72 D. Alberga and G. Mangiatordi, *J. Phys. …*, 2014.
73 N. R. Tummala, C. Risko, C. Bruner, R. H. Dauskardt and J. L. Br??das, *J. Polym. Sci. Part B Polym. Phys.*, 2015, **53**, 934–942.
74 H. Münstedt, *Soft Matter*, 2011, **7**, 2273.
75 Y. K. Lan and C. I. Huang, *J. Phys. Chem. B*, 2008, **112**, 14857–14862.
76 R. S. Bhatta, Y. Y. Yimer, M. Tsige and D. S. Perry, *Comput. Theor. Chem.*, 2012, **995**, 36–42.
77 D. A. Kislitsyn, B. N. Taber, C. F. Gervasi, L. Zhang, S. C. B. Mannsfeld, J. S. Prell, A. L. Briseno and G. V Nazin, *Phys. Chem. Chem. Phys.*, 2016, **18**, 4842–9.
78 A. Warshel, M. Kato and A. V. Pisliakov, *J. Chem. Theory Comput.*, 2007, **3**, 2034–2045.
79 J. Schmidhuber, *Neural Networks*, 2015, **61**, 85–117.
80 G. Williams, *Chem.~ Soc.~ Rev*, 1978, **7**, 89ff.